

University of Southern Queensland
Faculty of Health, Engineering & Sciences

Axial Flux Permanent Magnet Coreless Machine

A dissertation submitted by

Vladislav Kaliyev

in fulfilment of the requirements of

ENG4111/4112 Research Project

towards the degree of

Bachelor of Electrical & Electronic Engineering

Submitted: October, 2015

Abstract

Axial Flux Permanent Magnet (AFPM) machines are becoming increasingly popular due to introduction of the second generation of rare-earth permanent magnets. Owing their unique construction and many advantages, AFPM machines have extensive topology and applications. Among them the coreless AFPM (without ferromagnetic material in the stator) offer reduced cogging torque which proved to be particular useful for special applications, e.g. low power wind energy generation, hub motors of electrical vehicles and electrical bicycles.

A Double Stator Internal Rotor prototype was designed and constructed to investigate the performance of the coreless construction. This geometry (not very popular due to poor winding utilisation) has an advantage of using less PMs. Polyester resin was used to hold eight cylindrical shape magnets of the eight pole machine. The large effective air gap of the coreless machine was minimised by keeping a physical air gap and the axial thickness of the trapezoidal stator coils to the minimum, after measuring the magnetic flux distribution around the rotor circular poles. Three types of stators were manufactured to enable a performance comparison: a blank without any conductors for mechanical losses estimation, a ribbon wire coreless and a ribbon wire with magnetic powder composite backing.

Test Results confirmed the limitations of the prototype's geometry and the validity of the AFPM design parameters. The magnetic powder composite backing countered the unfavourable magnetic flux distribution of the internal rotor allowing for increase in power output compared to the stator without backing. Both types of conductor stators do not have a cogging torque with EMF outputs being very close to pure sinusoidal. Ribbon shape of the coil conductor was very beneficial in producing thin rigid coils of large diameter. This might prove to be invaluable in a multi-disc configuration.

University of Southern Queensland
Faculty of Health, Engineering & Sciences

ENG4111/2 *Research Project*

Limitations of Use

The Council of the University of Southern Queensland, its Faculty of Health, Engineering & Sciences, and the staff of the University of Southern Queensland, do not accept any responsibility for the truth, accuracy or completeness of material contained within or associated with this dissertation.

Persons using all or any part of this material do so at their own risk, and not at the risk of the Council of the University of Southern Queensland, its Faculty of Health, Engineering & Sciences or the staff of the University of Southern Queensland.

This dissertation reports an educational exercise and has no purpose or validity beyond this exercise. The sole purpose of the course pair entitled “Research Project” is to contribute to the overall education within the student’s chosen degree program. This document, the associated hardware, software, drawings, and other material set out in the associated appendices should not be used for any other purpose: if they are so used, it is entirely at the risk of the user.

Dean

Faculty of Health, Engineering & Sciences

Certification of Dissertation

I certify that the ideas, designs and experimental work, results, analyses and conclusions set out in this dissertation are entirely my own effort, except where otherwise indicated and acknowledged.

I further certify that the work is original and has not been previously submitted for assessment in any other course or institution, except where specifically stated.

VLADISLAV KALIYEV

0061017263

Acknowledgments

I am pleased to acknowledge the the assistance given to me by number of people from Faculty of Health, Engineering and Science. First of all, I acknowledge Andreas Helwig for the actual idea of the project and his guidance and support throughout the whole duration of the project. I would like thank Joshua Peauril for providing advice on the epoxy and polyester resins manufacturing.

I thank Chris Galligan from Workshop Services for his tips on the use of metalworking equipment.

Finally, I am grateful to my family for their patience and encouragements.

VLADISLAV KALIYEV

Contents

Abstract	i
Acknowledgments	iv
List of Figures	ix
List of Tables	xv
Nomenclature	xvi
Chapter 1 Introduction	1
1.1 Sustainability aspects and Motivation	2
1.2 Aims of the research project	3
Chapter 2 Background	5
2.1 Topology	5
2.2 Specifics	8
Chapter 3 Literature Review	12
3.1 Permanent Magnets in AFPM machines	12

CONTENTS	vii
3.2 Foil (Ribbon) conductor coil in electrical machines	14
3.3 Double-Sided External Stator AFPM generator	16
3.4 AFPM for small wind turbines	17
3.5 AFPM with Circular Magnets and Coils	23
3.6 Manufacturing data	25
Chapter 4 Methodology	27
4.1 Design	27
4.2 Rotor Design	29
4.3 Stator Design	35
4.4 Prototype/Test Bed Construction	45
4.5 Testing	45
4.6 Theoretical Performance	47
Chapter 5 Results	49
5.1 Blank Stator Generator	49
5.2 Stator 1 Generator	51
5.3 Composite Stator 2 Generator	55
5.4 Stators' Performance and Comparison	61
Chapter 6 Conclusion	66
6.1 Summary points	66
6.2 Future Work	67

References	69
Appendix A Project Specification	72
Appendix B Project Risk Assessment	74
B.1 Risk Assessment	75
Appendix C Manufacture and Testing	78
C.1 Parts and materials used for AFPM prototype manufacturing	79
C.2 Rotor manufacturing	81
C.3 Stator manufacturing	87
C.4 Test Equipment	95
Appendix D Program Source Code	96
D.1 The <code>rotor_and_bushing.m</code> MATLAB program	97
D.2 The <code>stator_coils.m</code> MATLAB program	101
Appendix E Project Timeline	107

List of Figures

- 2.1 AFPM machine topology. (Adapted from Mahmoudi, Rahim & Hew (2011)). 6

- 3.1 Permanent Magnets comparison. (Adapted from MEDER electronics (2015)). 12

- 3.2 N38M demagnetisation curves showing very strong dependance on temperature of NdFeB PMs(Adapted from ARNOLD Magnetics Technologies (2015)). 14

- 3.3 AFIR (Axial Flux Internal Rotor) machine. (Adapted from Javadi & Mirsalim (2010)). 17

- 3.4 Flux path of AFIR machine. (Adapted from Javadi & Mirsalim (2010)). . 17

- 3.5 Flux path of AFIR machine. (Adapted from Ani, Polinder & Ferreira (2012)). 19

- 3.6 High speed Double-Sided Internal Stator AFPM with circular magnets. (Adapted from Fei, Luk & Jinupun (2010)). 24

- 3.7 Power Output vs circular Coils Inner Radius R_i , normalised to the Outer Radius R_o . It is used in Double-Sided Internal Stator AFPM with circular PMs. (Adapted from Fei et al. (2010)). 25

- 3.8 “WPS2000 Inc” 5kw VAWT power and voltage outputs versus RPM. (Adapted from WPS2000 Inc. (2015)). 26

4.1	Axial view of the rotor. Rotor's principle dimensions are shown. The position of the 8 magnets are drawn in red with crosses indicating their centre points. An appropriately scaled version of this figure was used as a template for magnets' holes positioning.	30
4.2	Axial and side views of the rotor bushing. The aluminium rotor bushing is the connection point between the rotor structure (polyester resin) and the aluminium shaft. The symmetrical cut-outs aim to strengthen the adhesion point of polyester resin to the aluminium.	31
4.3	Manufactured rotor pressed on an aluminium shaft.	32
4.4	Typical set-up for magnetic flux measurements.	32
4.5	Net magnetic flux out of the poles of the rotor (axial direction).	33
4.6	Net magnetic flux along the side of the rotor.	34
4.7	Stator Winding Distribution across both sides. Phases <i>A</i> , <i>B</i> and <i>C</i> are shown in <i>red</i> , <i>yellow</i> and <i>blue</i> respectively. The rotation of rotor is counterclockwise. For <i>8pole</i> machine $360^\circ Elec = 90^\circ Mech$. There are 4 coils per each phase.	36
4.8	First half (side) of the stator coils. There are 6 coils per stator side, with 2 coils belonging to each of the phases <i>A</i> , <i>B</i> and <i>C</i>	37
4.9	Second half (side) of the stator coils. The coils in this side are physically offset by $30^\circ Mech = 120^\circ Elec$ compared to coils in Figure 4.8. Rotation of coils in Figure 4.8 by $30^\circ M$ anticlockwise (in the direction of rotor rotation) changes <i>A</i> to <i>B</i> , <i>C</i> to <i>A</i> , and so on.	37
4.10	One half (side) of the stator coils and physical limits. Stator coils limits are super positioned onto the axial view of the rotor. The single loop coils are shown in black dashed bold and the physical boundaries for individual coils are in red. The boundaries limit the coils extension beyond the <i>rotor bushing collar</i> and mark the borders in the space between adjacent coils. The figure was produced using MATLAB program listed in Appendix D.2	38

4.11	Single coil boundaries within the coil span angle of $\theta_c = 60^\circ$. The coil is super positioned onto the axial view of the rotor. The thickness of coil is $8mm$ allowing for $0.5mm$ clearance between adjacent coils.	38
4.12	Magnified view of a typical manufactured ribbon conductor. Ribbon produced by rolling a round wire. The external dimensions are easily determined using vernier calipers. The height of the end arcs H_{arc} is estimated using USB microscope (item 2 in Appendix C.4).	42
4.13	Dimensions of the manufactured ribbon wire used for calculations its active area and number of turns.	42
4.14	A wound coil with 8 turns.	43
4.15	Two single layer coils joined together with inner conductors soldered and outer conductors available for external connection. A tinned clip made of ribbon wire used for soldered joints is also shown.	43
4.16	A manufactured stator side - 6 coils set in a polyester epoxy.	44
4.17	Stator manufacturing template.	44
4.18	A typical experiment set-up circuit diagram.	46
5.1	Assembled AFPM generator with blank stators. Blank stators have exactly the same dimensions and finish as stators with coils.	49
5.2	ΔV Load Cell and <i>Shaft Torque</i> proportional to mechanical losses. The actual measured data is shown in red. The Cubic Fit Function is used as the mechanical losses data for further analysis as it averages out irregularities in measurements and two pronounced peaks around 600RPM and 800RPM which are caused by vibrations at those frequencies.	50
5.3	Assembled AFPM generator with the 1st stator. The ends of individual phases <i>A</i> , <i>B</i> and <i>C</i> on each half of the stator are taken out axially and supported inside the terminal blocks on the end plates of the generator.	51

5.4	The no load output from the 1st Stator Generator produced on the screen of a digital oscilloscope. The 3 phase output and the voltage at the output of 3 phase rectifier (shown in green color - Channel 4) are obtained at 750RPM or at 50Hz.	52
5.5	A, B and C phases waveforms of the Stator 1 generator (no-load, 50Hz). . .	52
5.6	The no load output from 3-phase rectifier.	53
5.7	Voltage versus Current (V-I) at varying loads.	53
5.8	Voltage and Power output from 3-phase rectifier at constant load.	54
5.9	2nd stator (composite) AFPM generator on the test bed.	55
5.10	The no load output from the 2nd Stator Generator produced on the screen of a digital oscilloscope. The 3 phase output and the voltage at the output of 3 phase rectifier (shown in green color - Channel 4) are obtained at 750RPM or at 50Hz. The output here is higher compared to 1st Stator in Figure 5.4	56
5.11	A, B and C phases waveforms of the Stator 2 generator (no-load, 50Hz). . .	57
5.12	The no load output from 3-phase rectifier.	57
5.13	Voltage versus Current (V-I) at varying loads.	58
5.14	Voltage and Power output from 3-phase rectifier at constant load.	58
5.15	V-I and Stator Temperature for varying loads.	59
5.16	Stator temperature output after 20 minutes at 11A output current.	60
5.17	Plain camera view corresponding to the IR image in Figure 5.16.	60
5.18	Additional IR image (after 20 minutes at 11A output current) showing the temperature of the rotor reaching about 40°C.	60
5.19	Stators 1 and 2 Harmonic RMS no-load output at 50Hz.	63

5.20	Stators 1 and 2 comparison in Power, V-I and load cell ΔV	64
5.21	Stators 1 and 2 comparison in Power vs Current at constant RPM and varying loads. There is about a 23% improvement for the Composite Stator in peak output power reference to the 1st Stator.	65
C.1	Rotor setup parts from left to right: pre-cut Fibreglass Chopped Strand Mat (CSM) 300gm, pre-cut Fibrecore 3mm Fibreglass, press plate, Rotor Bushings, former flange. The CSM adds structural strength to the core, while the Fibrecore gives extra body to the core.	81
C.2	Rotor supporting structure ready for polyester resin. The symmetrical cut-outs are visible on the surface of the Rotor Bushing. The concentricity of the Rotor Bushing and the <i>former</i> is maintained.	82
C.3	Rotor former set with the polyester resin (Top side).	82
C.4	Rotor former set with polyester resin (bottom side). CSM is clearly visible on the photograph.	83
C.5	Rotor magnets template is set – ready for drilling.	83
C.6	Rotor magnets holes are partially drilled.	84
C.7	Rotor magnets holes are being finalised to allow extra space for the adhesive.	84
C.8	Rotor supporting structure is ready for magnets (bottom side).	85
C.9	Rotor supporting structure is ready magnets (top side). There are imperfections in the surface finish. The magnets' placements are marked <i>N,S</i> to accommodate magnets' magnetic poles.	85
C.10	Rotor magnets are set with <i>Araldite Selleys</i> Epoxy Adhesive. There is a fillet of <i>Araldite</i> between the surfaces of polyester resin (core) and the magnets to provide an extra bond. The magnets' pole surfaces are free of any epoxy.	86
C.11	The complete rotor assembly. The rotor is pressed on an aluminium shaft.	86

C.12 A single layer coil is formed. There are 8 turns in the coil.	88
C.13 A single layer coil is clamped while under tension before removing from the winding machine.	88
C.14 A single layer coil is removed from the winding machine. Once the centre former is knocked out the coil can be zip-tied allowing for clamp removal.	89
C.15 Araldite is applied to the sides of a single layer coil.	89
C.16 Two single layer coils are correctly oriented for joining.	90
C.17 A complete coil is formed by applying Araldite between the individual layers. The inner ends are soldered with an aid of tinned clamped.	90
C.18 The stator mould.	91
C.19 6 coils are positioned inside the stator mould.	91
C.20 A stator without magnetic backing.	92
C.21 A stator with composite magnetic backing.	92
C.22 A stator side complete. There are 6 coils per stator side.	93
C.23 Two stator sides without magnetic backing. 6 individual coils of each side are joined into 3. Two coils belonging to the same phase are connected in series. The ends of final 3 coils of a stator side are terminated with a 6 way terminal block for easy connection and disconnection.	93
C.24 Two stator sides with magnetic composite backing. The darker color of the iron powder (compared to Figure C.23) is clearly visible.	94

List of Tables

3.1	Typical values for N38M grade NdFeB PMs. (Data adapted from ARNOLD Magnetics Technologies (2015))	13
3.2	Rotor loss Constants.	21
3.3	Harmonic content of line EMF for generator with circular magnets and circular coils. (Data adapted from Fei et al. (2010))	25
5.1	Stator winding parameters	56
5.2	Generator Characteristics	61
5.3	Total Harmonic Distortions	63

Nomenclature

	AF	Axial Flux
	AFIR	Axial Flux Internal Rotor
	AFPM	Axial Flux Permanent Magnet
	CSM	Chopped Strand Mat
	DC	Direct Current
	IR	Infrared
ABBREVIATIONS	NdFeB	Neodymium Iron Boron
	PM	Permanent Magnet
	PWM	Pulse Width Modulation
	RPM	Rotations Per Minute (also <i>rpm</i>)
	SmCo	Samarium-Cobalt
	THD-F	Total Harmonic Distortion as comparison to the fundamental
	THD-R	Total Harmonic Distortion as comparison to the signal's RMS value
	VAWT	Vertical Axis Wind Turbine
	c	coil
	cu	copper
	e	eddy
	Fe	iron
	g	gap
SUBSCRIPTS	h	hysteresis
	m	magnet, magnetic
	ph	phase
	pk	peak
	rec	recoil
	sy	stator yoke

	B	Vector Magnetic Flux Density
	B	Magnetic Flux Density (Magnetic Induction)
	B_{avg}	Average magnetic flux density
	$(BH)_{max}$	Maximum energy density point on demagnetisation curve
	B_{mg}	Peak value of Magnetic Flux Density in air gap
	B_r	Remanent Magnetic Flux Density (remanence)
	D_{in}	Inner diameter of PM mounting
	D_{out}	Outer diameter of PM mounting
	e	Instantaneous EMF
	E	EMF
	\hat{E}	Peak EMF value
	E_a	No-load EMF of phase A of AFPM machine
	f	frequency (Hz)
	g	Air gap
	H	Vector Magnetic Field Intensity
	H	Magnetic Field Intensity (Magnetic Field Strength)
SYMBOLS	$i\mathbf{H}_c$	Intrinsic coercive field strength
	H_c	Coercive Magnetic Field Strength (coercivity)
	h_m	Magnet axial thickness
	k_d	Inner to Outer radius or (diameter) ration $k_d = \frac{R_{in}}{R_{out}} = \frac{D_{in}}{D_{out}}$
	k_w	Winding factor
	n	Rotational speed (rpm)
	N_c	Number of turns per coil
	N_s	Number of turns per stator phase
	p	Number of pole pairs, $2p =$ total number of poles
	P	Number of poles $P = 2p$
	R_{in}	Inner radius of PM mounting
	R_{out}	Outer radius of PM mounting
	R_{load}	Load resistance
	V_{mean}	Mean voltage (V)
	V_{diode}	Diode voltage drop
	\hat{V}_L	Peak linear voltage (V)
	w_m	Magnet width (also pole width and pole diameter for round magnet)
	Z_a	Impedance of phase A of AFPM machine

	α_B	temperature coefficient for B_r [%/°C], $\alpha_B < 0$
	α_H	temperature coefficient for H_c [%/°C], $\alpha_H < 0$
	α_i	magnet width (pole arc) to pole pitch ratio
	ϵ_0	permittivity of free space $\epsilon_0 = 8.854 * 10^{-12} F/m$
	ϵ	Richter's constant $m^4/(H \text{ kg})$
	η_d	coefficient of distortion of magnetic flux density
	θ_c	coil span angle
	μ_0	magnetic permeability of free space $\mu_0 = 4\pi * 10^{-7} H/m$
	μ_r	relative magnetic permeability
	μ_{rec}	recoil magnetic permeability $\mu_{rec} = \mu_0 \mu_{rrec} = \frac{\Delta B}{\Delta H}$
SYMBOLS	μ_{rrec}	relative recoil magnetic permeability
	ρ_{cu}	copper electric resistivity $\rho = \frac{1}{\sigma}$
	σ_{cu}	copper electric conductivity $\approx 57 * 10^6 S/m$ at 20°C and $\approx 47 * 10^6 S/m$ at 75°C
	σ_{Fe}	electric conductivity of steel $\approx 4.5 * 10^6 S/m$ at 20°C
	σ_{PM}	NdFeB PM electric conductivity $\approx 0.5 - 0.85 * 10^6 S/m$ at 20°C
	τ_{Fe}	specific density of core material
	τ_c	coil pitch
	τ_p	pole pitch
	ϕ	instantaneous magnetic flux
	Φ	peak magnetic flux
	ω	radian frequency (rad/s)
	A	Amperes (<i>SI</i> unit of electric current)
	A/m	Amperes per Meter (<i>SI</i> unit of magnetic field strength H)
	G	Gauss (<i>CGS</i> unit of magnetic flux density B) $1G = 10^{-4}T$
	T	Tesla (magnetic flux density B)
UNITS	mil	a thousandth of an inch $1mil = 0.001in = 25.4\mu m$
	mT	milliTesla
	Oe	Oersted (<i>CGS</i> unit of magnetic field strength H) $1Oe = 79.577A/m$
	kOe	kiloOersted
	MGOe	megaGauss Oersteds (BH_{max}) $1MGOe = 7.9577kJ/m^3$
	V	Volts (<i>SI</i> unit of electric potential)

Chapter 1

Introduction

Electrical Machines (motors and generators) play a significant role in shaping human society. Since the electromagnetic energy generation discovery in nineteenth century, the use and applications of electric machines increased exponentially. A myriad of electrical machines have been built with sizes ranging from “nano-generators” to hundreds of megawatts (MW). The current applications of electrical machines covers all areas of industrial, domestic and personal use.

The electromagnetic machines have three main physical configurations: cylindrical radial, linear and disc axial. While the linear electrical machine has no rotating parts, the names of the radial and the axial rotating machines refer to the direction of main magnetic flux flow with reference to their rotor axes.

Despite the fact that the first invented electromagnetic generators were actually the Axial Flow (AF) machines, with the absence of suitable PMs, the radial machine construction has been the preferred type for long time and for very valid reasons: robust construction, ease of manufacturing and low cost.

The appearance of the second generation of rare earth permanent magnets (PM) and the progress in modern technology made it commercially viable to manufacture Axial Flux Permanent Magnet (AFPM) machines. So that many advantages of AFPM can now be exploited. Due to their flat construction and high power density, the AFPM (or disc machines) are used in electrical vehicles, pumps, fans, valve control, centrifuges, machine tools, robots, hard drives, mobile phones etc. (Gieras, Wang & Kamper 2008) . The

potential for the disc machines' applications seems to be limitless and their market share is expected to only increase in the future.

1.1 Sustainability aspects and Motivation

The ever increasing sustainability concerns of traditional power generation brings about an argument of finding the more viable methods. Changing from high power constant output coal and hydro prime movers to natural sources of mechanical energy (e.g. wind with low power and irregular drive) requires modifications to the types of generators used. This particularly relevant for low power generation units.

Small wind turbines is a popular complementary option to solar generation where connection to grid is not possible. However, at the moment the low power generation units are significantly more expensive per kilowatt than their high power counterparts (Ani et al. 2012). The continuing research to minimise the cost of materials, to increase efficiency, to simplify technology and availability of manufacturing methods would ultimately result in more small wind turbines units used. The benefits are twofold: green energy production and an affordable access to electricity to those in need of it.

The *coreless* AFPM structures with minimum cogging torque are critical for wind generators to allow operating in low wind areas, which are the typical areas of operation of small turbines. The coreless structures are also important in many other applications aimed at the environmental needs of not so distant future. These include hub motors of electrical vehicles and electrical bicycles where coreless construction allows for improved low speed control and linear torque-current characteristics, at the same time minimising unwanted pulsating torque. It is also advantageous in small portable devices like mobile phones and hard-drives where an increase in efficiency and a reduction in weight and size are of high priority.

The employment of permanent magnets in electrical machines is directed towards increasing power density (lighter materials can be employed to hold magnets) and elimination of field excitation losses. More importantly, the use of PMs significantly simplifies the electrical machine construction and consequently the required maintenance throughout the life of the device. This makes the technology more readily available to the wider community. Additionally, owing the construction simplicity, an AFPM machine can be constructed

from many readily available recycled materials. AFPM wind generators constructed from vehicle's hubs is just one example.

Another area of AFPM research is a stator design to suit a particular machine configuration and intended applications. One way to increase stator efficiency, and therefore reduce amount of copper conductors required, is to increase the coil packing factor. Ribbon (or foil) windings achieve higher packing factor and they also can be manufactured from available recycled materials. Currently manufacturing of ribbon (rectangular) transformer wire is considerably more expensive than the traditional round one. However, with a view of limited resources, ribbon wire benefits might be of higher importance in the future.

1.2 Aims of the research project

AFPM machines are particularly suitable for low power wind generator units. Simplified physical integration of a generator and a turbine, large possible number of poles and low inertia structures make AFPM machines very useful for low speed applications.

A PM machine is susceptible to two undesired pulsating torque components caused by: (1) harmonic content of the voltage and current waveform and (2) interaction of PMs with ferromagnetic material of the slotless or slotted stator (Gieras et al. 2008). This PMs interaction creates a holding force between rotor and stator which is called *cogging torque*. Coreless machines (machines without any ferromagnetic material) are generally free of cogging torque. The dilemma is that lack of ferromagnetic material in the core increases the effective air gap causing reduction in the machine's output.

In addition to the cogging torque reduction, elimination of any ferromagnetic material from the stator makes the associated eddy current and hysteresis losses non-existing. Also axial magnetic attraction forces between stator and rotor are eliminated at zero armature current state (Gieras et al. 2008).

The coreless construction of AFPM machines allows for low cut-in wind speeds of wind generator turbines. However, the coreless construction requires more PM volume material and very careful air-gap magnetic flux distribution analysis for the same power output.

Of the many types and applications of AFPM machines the following are the *objectives* of this research paper:

- Investigate performance of the coreless AFPM construction, especially suitable for wind energy generation, through construction and testing of a prototype.
- Investigate the use of foil winding in the AFPM stator coils.

Chapter 2

Background

This chapter provides background information about Axial Flux Permanent Magnet machines including AFPM topology, classification, advantages and disadvantages. The *Double-Sided External-Stator* AFPM configuration, coreless machine and permanent magnet (PM) information are considered in greater detail.

2.1 Topology

As the name suggests Axial Flux Permanent Magnet (AFPM) machines utilise Permanent Magnets (PM) in their design and the direction of the magnetic flux flow within AFPM is parallel to the rotor axis. AFPMs are also called *disc machines* as their stators and rotors are of a disc shape effectively forming a “pancake” stack. Despite the fact that the disc machines look significantly different in appearance (to their conventional radial equivalents) the electromagnetic principles employed within are essentially the same. The major difference is in their construction. The AFPM construction can be imagined as follows. Starting with the radial machine, effectively “unroll” both the cylindrical rotor and the cylindrical stator from the cylinder shape to a flat rectangle and then “bent” this rectangle in its plane to form a circular flat donut.

There are many publications that discuss the available configuration for AFPM. Mahmoudi et al. (2011) provides a useful figure depicting the main AFPM topologies (Figure 2.1).

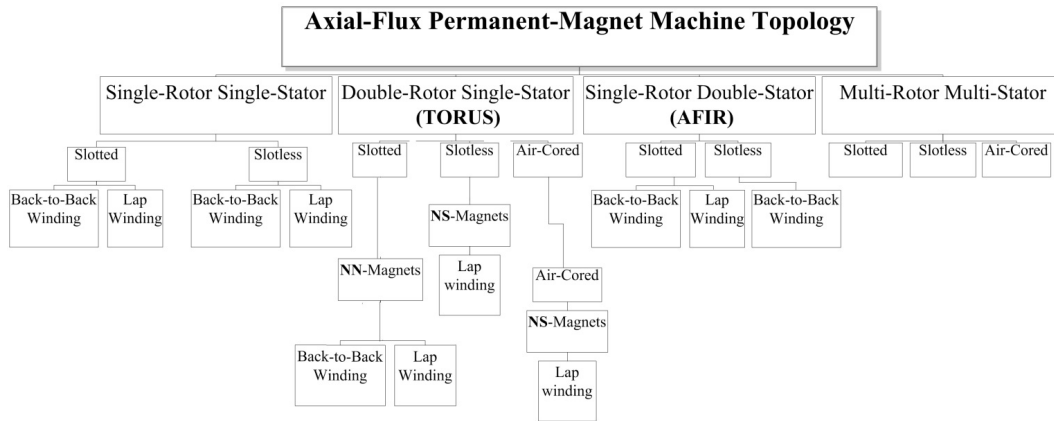


Figure 2.1: AFPM machine topology. (Adapted from Mahmoudi et al. (2011)).

As can be seen from Figure 2.1, the single sided machines have one rotor and one stator. The double sided machines have either two rotors and a single stator or equally two stators with a single rotor. The multi-rotor/multi-stator machines provides a convenient method of increasing power to the desired level just by stacking extra discs. The armature can be made with slots (similar to the radial machine) or without. The slotless armature can have a ferromagnetic core or it can be set in resin (coreless type). Finally, the magnets can be surface mounted or can be of internal type.

Types

AFPM machines have virtually the same main classification types: *PM DC commutator*, *PM brushless DC*, *synchronous AC* and *induction* (Gieras et al. 2008). PM DC commutator machines use PMs for the field excitation and can have a *wound rotor* or *printed winding rotor* (Gieras et al. 2008). While the wound rotor copper winding is set in a resin type mould, the printed armature winding is made from coils of sheet copper set on non-ferrous disc to form a wave winding (similar to the wave-connected armature of the radial machine).

DC brushless and AC synchronous machines have similar construction to the PM DC commutator, except for magnets being mounted on the rotor and the obvious operational differences.

Stator

There is a variety of windings used in AFPM machines to suit a particular application. The two main types are *concentrated* and *distributed* (in slots) windings. Both types can

be of *overlap* or *non-overlap* kind, which refers to physical overlapping of coils in the stator. At the same time, they can be a *single layer* or *double layer*, which identifies the number of coil sides per single slot (Gieras et al. 2008).

Special type of winding is a *toroidal* one, which is normally employed in Double-Sided External-Rotor configuration, where coils are wound on the toroidal shape stator.

Finally, the coreless stators can be multi-turn coils of round or rectangular conductors, or *printed windings (film coil winding)*. The shapes of winding coils employed are usually circular, trapezoidal and rhomboidal. The circular and trapezoidal coils generally employed to match the shapes of magnets used within the machine. The rhomboidal coils are considered if minimum *long-end* winding is desired (at the expense of reduced torque).

Rotor

AFPM brushless machines have rotors with either *surface mounted* or *internal* magnets. There several commonly used shapes of magnets employed in rotor magnetic circuits. They are trapezoidal, circular or semicircular. The *PMs shape* and the *distance between adjacent magnets* will determine the distribution of the air gap magnetic field and the harmonics content (quality) of output voltage (Gieras et al. 2008). Additionally, the shape of magnets affects *cogging torque* within the machine.

Strong PMs (Alnicos, rare-earth, etc.) are usually used in AFPM machines. It is a common practice to fabricate rotors using surface magnets (for reasons of achieving flat shape and keeping minimal effective air gap). The surface magnets are usually attached to a ferromagnetic plate which aids in completing magnetic circuit.

Advantages/Disadvantages

The AFPM machines have the inherent disadvantages which has prevented their widespread manufacturing up till recent decade. They are described by Gieras et al. (2008) and Aydin et al. (2004) as follows:

- Strong axial magnetic attraction force between the stator and rotor in the steady zero-current state (cored armature). This dictates the more heavy duty construction (e.g. increased base plate thickness) for rotors and stators.
- Difficulties in assembling and keeping the uniform air gap.

- Fabrication difficulties (cutting slots in laminated cores) and high cost of manufacturing the laminated stator cores.
- Small surface contact between the rotor and shaft leading to difficulties in designing a high mechanical integrity rotor-shaft mechanical joint in the higher range of the output power.
- Long end windings of some AFPM topologies contribute to higher copper losses and inefficiencies (Aydin et al. 2004).
- Still existing the relative high cost of strong PMs.

Nevertheless, with the appearance of rare earth PM and the modern technology, AFPM machines are becoming increasingly more commercially viable. So, the following advantages of the AFPMs can be exploited in accordance with Aydin et al. (2004) and Gieras et al. (2008):

- Flat disc construction leading to small axial dimensions. - Large outer diameter makes it suitable for special purpose applications (e.g. fly-wheel effect and high torque applications).
- Capable of being designed to have higher power-to-weight ratio resulting in less core materials.
- Planar and adjustable air gaps. Reduced noise (slotless armature construction).
- The AFPM machine is suitable for modular construction allowing for adjusting to the required power and torque levels.
- Large number of poles housed by a large diameter core leads to high frequency or low speed operations.
- Having the inner diameter of the core much greater than the shaft diameter, better ventilation and cooling can be designed, which ultimately contributes to higher power output.

2.2 Specifics

Chosen Design specifics

Of the discussed above AFPM types, this paper works towards designing brushless *Single-rotor/Double-Stator* AFPM machine.

The Single-rotor/Double-stator configuration (also known as *Axial Flux Internal Rotor* (AFIR) or *Double-Sided External-Stator*) has been chosen due to availability of only 8 magnets for this research project. This particular configuration has the advantage of needing less PMs at the expense of poor winding utilisation and is not considered to be an advantageous machine topology (Gieras et al. 2008). One of other drawbacks of this configuration is more complicated connection of the rotor to the output compared to the External Rotor configuration, where the integration of generator to turbine (for small wind turbine) is simpler as generator can be bolted easily to turbine rotor (Ani et al. 2012).

Since the magnetic flux does not need to travel through the rotor structure the magnetic type material is not used to hold the rotor magnets. So the nonmagnetic (and potentially lighter in weight) material can be used as the rotor base material. This can lead to better power to inertia ratio making it suitable for applications which require small inertia (Aydin et al. 2004). Wind generation is one of this applications.

In addition to non-magnetic, to eliminate the rotor losses a non-metal rotor structure, similar to epoxy resin, can be used.

Coreless Specifics

A Coreless stator does not have any ferromagnetic materials in its armature. Gieras et al. (2008) highlighted the majority of advantages of Coreless stator in AFPM which can be summarised as following:

- Coreless stator has less axial magnetic forces acting between stators and rotors, considerably simplifying construction and assembly.
- Cogging torque (at zero-current) and stator core losses (eddy current and hysteresis loss) are eliminated.
- Rotor surface losses, magnetic saturation and acoustic noise (in case of slotless design) are reduced.
- Slotless winding do not require a complex manufacturing process.

The *negative side* of coreless structure is that more volume of PM is required to produce the same output as the ferromagnetic core stators, lower winding inductances potentially causing problems for inverter-fed motors, and significant eddy current losses in stator conductors. Additionally all slotless armature windings typically will have larger magnetic

air gap, which necessitates a careful design to maximise efficiency and minimise leakage flux.

Mahmoudi et al. (2011) points out that although the problem of cogging torque is answered with ideal coreless stator, the parasitic pulsating torque still exists. The proposed and researched ways of torque ripple reduction are similar to radial machines: magnet shaping, winding shaping and skewing. Additionally, a specific configuration of AFPM design can be modified, e.g. for the two rotors and internal double stator setup an inclusion of extra angular displacement between stator sides reduces the resulting cogging torque.

Permanent Magnets

The lack of field windings is one of the key advantages of using permanent magnets in electrical machines. The general magnetism theory is still applicable. There are, however, some specifics in using PMs.

The magnets store the magnetic energy within. Being the source of the magnetic energy, there exists a magnetic potential between poles of the magnet (${}_i\mathbf{H}$) which is 180° to the intrinsic flux density \mathbf{B}_i . Any external magnetic circuit (with intensity \mathbf{H}) opposing the magnet tends to demagnetise the PM in accordance with Equation 2.1. The degree of demagnetisation will depend on the magnet geometry and permeance of the external magnetic circuit (Gieras 2010).

$$\mathbf{B}_i = \mathbf{B} - \mu_0\mathbf{H} \quad (2.1)$$

The magnetisation curves are generally used for external magnetic circuits. In the case of PMs the *demagnetisation curves* are the design parameter. The *demagnetisation curve* is the 2nd quadrant portion of the the hysteresis loop. As long as the external magnetic field intensity \mathbf{H} (in opposition to the magnet's field) does not exceed the *intrinsic coercive field strength* ${}_i\mathbf{H}_c$, the magnet demagnetisation curve can be approximated by the *recoil line*, the slope of which is described by the *recoil magnetic permeability* μ_{rec} , which is the ratio of the magnetic flux density to magnetic field intensity at any point on the demagnetisation curve (Gieras 2010) (Equation 2.2).

$$\mu_{rec} = \mu_0\mu_{rrec} = \frac{\Delta B}{\Delta H} \quad (2.2)$$

where,

μ_{rrec} – relative recoil permeability of the magnets $\mu_{rrec} = 1 \dots 3.5$, and

μ_0 – magnetic permeability of free space $\mu_0 = 4\pi * 10^{-7} H/m$

The usual causes of PMs demagnetisation is the presence of high permeability material not at the pole faces (which also increases leakage flux) , excessive vibration and temperature. The strength of magnets is significantly reduced with temperature. Both the remanence (B_r) and the coercivity (H_c) are reduced with increase in temperature in accordance with Equation 2.3 (Gieras 2010). The net result of increase in temperature of PM is lower position of the demagnetisation curve, which in turn lowers the *maximum energy product* $(BH)_{max}$ and the energy available from the magnet.

$$\begin{aligned} B_r &= B_{r20} \left(1 + \frac{\alpha_B}{100} (T - 20) \right) \\ H_c &= H_{c20} \left(1 + \frac{\alpha_H}{100} (T - 20) \right) \end{aligned} \quad (2.3)$$

where,

T – temperature of PM [$^{\circ}C$],

B_{r20} – remanent magnetic flux density at $20^{\circ}C$ [T],

H_{c20} – coercivity at $20^{\circ}C$ [A/m],

α_B – ($\alpha_B < 0$) B_r temperature coefficient [$\%/^{\circ}C$], and

α_H – ($\alpha_H < 0$) H_c temperature coefficient [$\%/^{\circ}C$].

Gieras et al. (2008) states that PMs behave differently than a DC electromagnet, that the energy of PMs is not constant if the permeance and exciting current of the external armature changes.

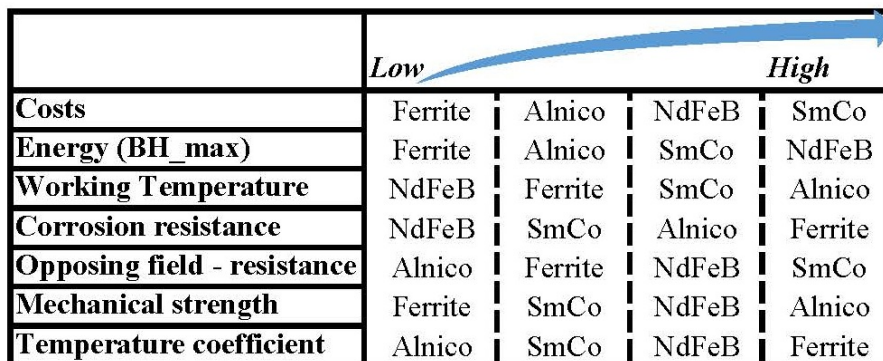
Chapter 3

Literature Review

This chapter investigates the current state, technology and materials used for slotless coreless and cored AFPM machines, especially suitable for wind generation use.

3.1 Permanent Magnets in AFPM machines

There are three classes of PMs used in electrical machines (Gieras 2010): Alnicos (with high B_r , low temperature coefficients α_B and α_H , low H_c and non-linear demagnetisation curve), Ferrites (with higher than Alnicos H_c , lower than Alnicos B_r , high temperature coefficients α_B and α_H , low cost, very high electric resistance) and rare-earth PMs (“first gen” Samarium-cobalt SmCo and “second gen” neodymium-iron-boron NdFeB). The convenient comparison of the magnets is given in Figure 3.1 (MEDER electronics 2015).




	<i>Low</i>  <i>High</i>			
Costs	Ferrite	Alnico	NdFeB	SmCo
Energy (BH_max)	Ferrite	Alnico	SmCo	NdFeB
Working Temperature	NdFeB	Ferrite	SmCo	Alnico
Corrosion resistance	NdFeB	SmCo	Alnico	Ferrite
Opposing field - resistance	Alnico	Ferrite	NdFeB	SmCo
Mechanical strength	Ferrite	SmCo	NdFeB	Alnico
Temperature coefficient	Alnico	SmCo	NdFeB	Ferrite

Figure 3.1: Permanent Magnets comparison. (Adapted from MEDER electronics (2015)).

The second generation rare earth magnets - Neodymium-Iron-Boron (NdFeB) - are most

popular PMs for use in AFPM machines, and for good reasons. Besides becoming affordable in recent years, NdFeB PMs have high values of the maximum energy product $(BH)_{max}$, they have almost linear demagnetization curve, high values of remanent magnetic flux density B_r and coercivity H_c . These qualities contribute to low volume/mass, higher efficiency and tolerance to gap variations which make NdFeB PMs most suitable for use in AFPM machines (Gieras 2010).

The major disadvantages of NdFeB magnets are: their demagnetisation curve strong dependency on temperature, and their susceptibility to corrosion. These limitations set the general requirements for cooling (to maintain operating temperature) and considerations for the thermal conductance of the materials around the PMs and anti-corrosion coating.

As an example, an NS87100 NdFeB magnet (*diameter = 0.875inch* and *height = 1inch*) is offered by *Dura Magnetics Inc* (Dura Magnetics, Inc 2015). This is a 3814 grade, sintered neodymium alloy magnet (same as N38M or ND-38M grade) with the average value of the *maximum energy product* $(BH)_{max} \approx 299kJ/m^3$ (38MGOe) and the intrinsic coercivity of $iH_c \approx 1114kA/m$ (14000 Oersteds). The specification values for this magnet are given in Table 3.1 and the demagnetisation curves are shown in Figure 3.2 (data is provided by ARNOLD Magnetics Technologies (2015)).

Table 3.1: Typical values for N38M grade NdFeB PMs. (Data adapted from ARNOLD Magnetics Technologies (2015))

B_r	H_c	iH_c	$(BH)_{max}$	α_B	α_H	$Temp_{max}$
1260 T	899 kA/m	1114 kA/m	307 kJ/m ³	-0.12 %/°C	-0.595 %/°C	100 °C

The *electrical resistivity* of N38M magnet is given as $180\mu\Omega * cm$ ($\approx 0.56 * 10^6 S/m$). Therefore, the losses in conductive PMs due to higher harmonic magnetic fields produced by the stator must be taken into account (Gieras et al. 2008).

Nguyen & Tseng (2012) investigated the losses in rare-earth magnets in AFPM machine. The operating frequency increases the magnet losses which are mainly caused by time harmonics of PWM in supply voltages. Eddy currents circulating in the magnets can be reduced by increasing their circulating path lengths. Similar to the idea of the core laminating, it was found that eddy-current losses can be reduced by magnet segmentation in both circumferential and radial directions.

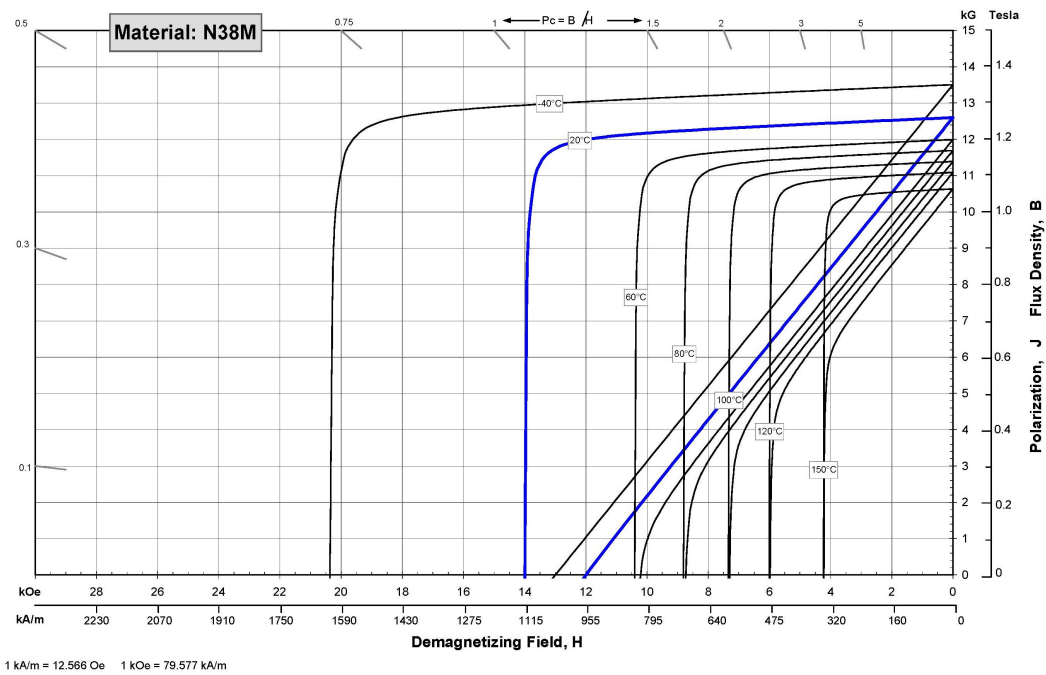


Figure 3.2: N38M demagnetisation curves showing very strong dependence on temperature of NdFeB PMs(Adapted from ARNOLD Magnetics Technologies (2015)).

3.2 Foil (Ribbon) conductor coil in electrical machines

The continuing trend for miniaturisation (while maintaining (or improving) the power to volume efficiency and performance-to-cost ratio) is the main reason for the interest in foil windings. Foil winding is one of the areas of research (rare-earth magnets is another) that works towards building low volume, high power density machines.

Lorilla et al. (2006) highlights the main benefits of foil windings of their prototype based on the conventional Lundell alternator (the principles are equally applicable to the AFPM machines). The practical experiments were based on modifying the field winding of the Lundell alternator from traditional round wire (440 turns of 40 mil) to foil winding (90 turns of 5mil with 1mil insulation). To achieve the required ampere-turns a higher current with lower voltage has been supplied through brushes and a DC-DC converter. The highlighted benefits are:

- The geometric *packing factor* (also *fill factor*) of the foil winding (for the same number of turns and the same current carrying capacity) is increased from about 0.6 to above 0.7 (the prototype achieving a 15% improvement). Therefore, for a given volume a higher number of turns can be achieved. Equally the higher current

carrying capacity can be achieved for the given number of turns. Both result in higher ampere-turn.

- The thermal properties of the foil winding improved due to better heat transfer across a winding layer). This allows for a higher winding current for a given temperature.

The use of thinner insulation for foil winding and re-design of the stator to accommodate the foil winding are the researchers' recommendations.

Foil winding in AFPM machine

The novel design experimented by (Melendez-Vega & Venkataramanan 2012) was inspired by an opportunity to recycle the old home video tapes and finding a cheaper alternative to traditional copper winding for AFPM generators in small wind turbines.

Melendez-Vega & Venkataramanan (2012) has experimentally tested a performance of aluminium foil in the stator of a commercially manufactured generator (a 500W, 5-phase, 12 pole, air core AFPM direct drive Scoraig Wind Electric generator). The stator coils were rewired using aluminium foils insulated with VHS video tape. 3 aluminium foil stators had been built and tested and compared to the original round copper winding stator.

The best performing aluminium coil design has less number of turns (125 turns compared to the copper 150 turns), larger conductor cross section ($1.51mm^2$ compared to $1.09mm^2$ for copper), larger resistance (0.64Ω compared to 0.42Ω) and comparable inductance ($1.22mH$ compared to $1.3mH$) taking into account less number of turns of the foil winding.

Despite the increased aluminium stator coils impedance, by reducing the magnetic air gap, a similar performance to the original stator in the output power VS rotor speed and a low cut-in speed has been achieved. An additional advantage of using the magnetic VHS tape as the insulator between the foil turns was the increased permeability causing corresponding increase in the magnetic flux and the open circuit voltage.

Melendez-Vega & Venkataramanan (2012) suggested future work: 1) thinner coil to achieve smaller air gaps and an increase in voltage. 2) Inclusion of magnetic materials (i.e. ferric oxide powder) in the stator cast in order to achieve uniform permeability and further reduce the reluctance.

Disadvantages of Using Ribbon Wire

Cost

Still the cost of the ribbon wire is considerably higher than that of a traditional round copper. As an example, a 22AWG round wire can be purchased for around 7\$/lb while the equivalent size flat magnet wire with ratio 1:4 can cost about 17\$/lb. The cost of thinner foil winding can be considerably higher owing added step in a manufacturing process and finding suitable insulation. Therefore, a method of producing cheaper ribbon wire would be of great advantage for small generator manufacturing.

Eddy Current Losses

The use of flat wire could lead to potential increase of eddy current losses (Ani et al. 2012). This especially pertinent to coreless stator design where the eddy current losses in the windings exposed to PM magnetic field are already increased due to lack of the ferromagnetic core.

3.3 Double-Sided External Stator AFPM generator

To solve the problem of increased electrical power demand of modern vehicles Javadi & Mirsalim (2010) have proposed and built the AFPM generator for yet to come 42V vehicle electrical system. The AFPM generator is Double-sided External Stator. The actual prototype built has ironless stator with solid mild steel back plates on the outer sides. The stator uses concentrated coils glued on non-conducting material. The rotor has flat NdFeB magnets supported on an aluminium disc. The machine configuration is shown on Figure 3.3 with the flux path are shown on Figure 3.4.

Stators one side is stationary and the other is allowed to rotate to create an angle between stator sides coils. This flux weakening feature is used for output voltage regulation.

The machine has been modelled and 3-D Finite-Element Method (FEM) calculation with motion has been used to compare with experimental details. Both results were closely aligned within accuracies of computer modelling and manufacturing.

The prototype is claimed to produce output voltage higher than the desired 42V which is

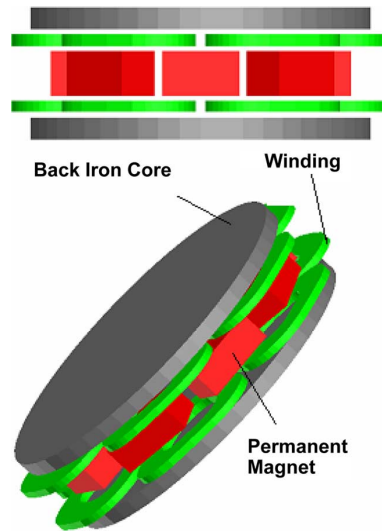


Figure 3.3: AFIR (Axial Flux Internal Rotor) machine. (Adapted from Javadi & Mirsalim (2010)).

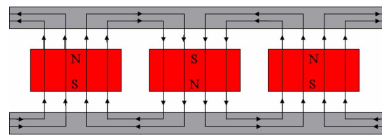


Figure 3.4: Flux path of AFIR machine. (Adapted from Javadi & Mirsalim (2010)).

very close to the sinusoidal at 2000rpm. Efficiency of higher than 91% has been achieved for a load current of 15A (the main losses are found to be the copper losses). A total harmonic distortion is under 6.9%. The coreless stator was found to contribute to low armature reaction. The added advantages are the lack of brushes and simple structure.

3.4 AFPM for small wind turbines

AFPM are becoming increasingly popular for use in small wind turbines owing their advantageous construction and recent technology developments where strong PMs are becoming more affordable. However, the small wind turbine (based on radial slotted and axial slotted types) are still (three times plus) more expensive per kW compared to large turbines (Ani et al. 2012). Ani et al. (2012) identifies specific problem pertaining to the operation of small wind turbine: since they operate in low to moderate wind areas they experience starting problems. Starting problems are caused by self-excitation principles of PM generators which is generally identified as a cogging torque.

Cogging Torque

A PM machine is susceptible to two undesired pulsating torque components (Gonzlez, Tapia & Bettancourt 2007) caused by: (a) harmonic content of the voltage and current waveform and (b) interaction of PMs with stator (cogging torque). Coreless machines are generally free of cogging torque. However presence of any ferromagnetic material in stator (whether slotless or slotted) will cause for a holding force to develop between the rotor and stator.

Gonzlez et al. (2007) investigated the methods of reducing the cogging torque for a slotted machine. Main methods that have been proposed are modifying magnet/slot shape and introduction of stator displacement. The techniques for modifying shapes involved modifying the magnet (or equally tooth for slotted machine) shape to make sure the whole edge of the magnet does not move in front of the tooth at the same time. These included magnets with rounded borders, magnet with rounded faces (both concave and convex) and skewing (magnet or teeth). The cogging torque reduction of 40-60% (with rounding parameter equal to slot width) has been achieved using the techniques.

Stator displacement involves introduction of angular shift between sides of an internal stator of Double-Sided configuration. The idea is to split in phase the cogging torque of each side.

To further develop idea of skewing Hsieh et al. (2009) proposed idea of “hybrid skewing” where North and South poles have different shapes. This technique on its own produced 57% reduction in cogging torque while maintaining the performance. Together with 2.5 degree stator displacement, authors claimed to have an 88% reduction in peak cogging torque compared to the standard trapezoidal non-skewed pole set up. The obvious drawback of the method, however, is the complexity in manufacturing not ideal for small scale production.

Effective Air gap

As a way to reduce the cost of manufacturing, at the same time reducing the cogging torque, Ani et al. (2012) investigated performance of Double-Sided External Rotor AFPM with coreless stator. Off the shelf surface magnets were fixed to steel rotor back iron. The structure of the machine is built around a standard vehicle hub. The developed diagram is shown on Figure 3.5.

The design highlights the large air gap which is typical for AFPM design, which is why

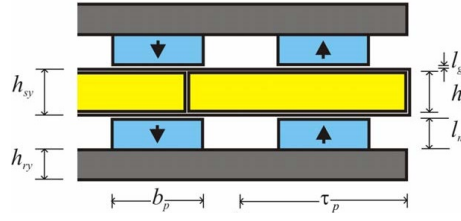


Figure 3.5: Flux path of AFIR machine. (Adapted from Ani et al. (2012)).

strong PMs (similar to NdFeB) are required. The effective air gap is a significant feature affecting the machine electrical output and is given as Equation 3.1:

$$l_{geff} = 2l_g + \frac{2l_m}{\mu_{rrec}} + h_{sy} \quad (3.1)$$

where,

l_g – the physical gap,

l_m – the magnet length in axial direction,

μ_{rrec} – relative recoil permeability of the magnets, and

h_{sy} – the stator thickness (sy-stator yoke).

Where l_g is the physical gap, l_m is the magnet length in axial direction, μ_{rrec} is the relative recoil permeability of the magnets and h_{sy} is the stator thickness (sy-stator yoke).

Losses

Low speed operation of wind turbines makes it necessary to account for generator losses, which can be grouped into Stator and Rotor losses.

$$P_{loss} = P_{stator} + P_{rotor} \quad (3.2)$$

Stator. For a *coreless* stator losses will consist of the copper losses and winding eddy current losses. The winding eddy current losses increase with an increase of active conductor area and decrease with increase in resistivity in accordance with Equation 3.3 (Ani et al. 2012):

$$P_{eddy\ cu} = \frac{1}{32} (\omega B_{gm} d)^2 \frac{2N_c l \pi d^2}{\rho_{cu} 4} \quad (3.3)$$

where,

d – diameter of copper wire,

l – length of wire exposed to magnetic field,

N_c – number of turns per coil,

ρ_{cu} – copper electric resistivity, and

B_{gm} – amplitude of the fundamental harmonic of gap flux density.

Therefore, the multi-strand wires can be employed to reduce eddy currents. The cost of manufacturing, however, is increased and is found to be not necessary for this application: the winding eddy current losses found to be insignificant for small generators operating at low speed, low frequency with relatively small peak flux density and wire diameter. Stator winding eddy currents losses are increased at higher speeds.

For *cored stator*, the windings eddy currents will be negligible and the major losses will be the core losses, which include iron eddy currents and hysteresis. The eddy current and hysteresis losses can be approximated by using Equation 3.4 and 3.5 respectively (Gieras et al. 2008):

$$P_{eddy\ core} = \frac{\pi^2 \sigma_{Fe}}{6 \tau_{Fe}} f^2 d_{Fe}^2 m_{Fe} (B_{mx1}^2 + B_{mz1}^2) \eta_d^2 \quad [W] \quad (3.4)$$

where,

σ_{Fe} – electric conductivity of core material ,

τ_{Fe} – specific density of core material ,

d_{Fe} – thickness of core material ,

m_{Fe} – mass,

f – frequency in Hz,

B_{mx1} – “x”-component (tangential) of the fundamental harmonic of magnetic flux density,

B_{mz1} – “z”-component (normal) of the fundamental harmonic of magnetic flux density,

η_d – coefficient of distortion of magnetic flux density ,

$\eta_d = 1$ eddy current losses under sinusoidal magnetic flux density.

$$P_{h\ core} = \epsilon \frac{f}{100} m_{Fe} (B_{mx1}^2 + B_{mz1}^2) \eta_d^2 \quad [W] \quad (3.5)$$

where,

ϵ – Richter’s constant,

$\epsilon = 2.8m^4/(H \text{ kg})$ for isotropic laminations with 2% Si, and

$\epsilon = (4.4 - 4.8)m^4/(H \text{ kg})$ for isotropic siliconless laminations

If multi-stranded wires are used to mitigate “skin” and “proximity” effects (Fei et al. 2010) for high frequency stator excitation, or for low frequency operation the coil resistance can be estimated using standard equation for resistance with accuracy depending only on the ability to accurately determine the conductor length per phase (Equation 3.6):

$$R_{phase} = \rho_{cu} \frac{l_{ph}}{A_{conductor}} \quad (3.6)$$

where,

ρ_{cu} – copper electric resistivity at $20^\circ C$,

l_{phase} – length of conductor per phase, and

$A_{conductor}$ – conductor cross section area

Rotor. The Rotor losses are rotor electrical and mechanical losses. Ani et al. (2012) identified the mechanical losses as windage losses proportional to the cube of the rotor speed $P_w = C_w \omega^3$ and bearing losses which are proportional to the speed $P_b = C_b \omega$. The value of C_w constant depends on the dimensions of the rotor disk, friction coefficient of the rotor disk and air density, while the constant C_b depends on the bearings used. For the manufactured machine in Figure 3.5 the constants were experimentally determined for 410rpm (Table 3.2).

Table 3.2: Rotor loss Constants.

Windage Loss constant (W)	4
Bearing Loss constant (W)	72

The result of using vehicle hub as the main supporting structure (with recycled bearings) resulted in mechanical losses contributing to the majority (80+%) of total no-load loss.

(The lesson is not to economise on bearings plus there is no need for multi-strand wires).

Dimensions There are many designs of AFPM generators that have been implemented and discussed in relevant literature. The physical dimensions and electrical specifications

are varied to suit particular applications. There are, however, general guidelines and recommendations to achieve best results.

Design of AFPM generator suitable for wind generation needs to consider the following :

- The type of output load will set the requirements for minimum V_{min} and maximum V_{max} output voltages of the generator. The typical loads are a battery or an inverter for connection to the grid (Latoufis et al. 2012).
- V_{min} is tied to the time when rotor blades will start rotating, which depends on the minimum wind speed (*cut-in speed* usually set at $3m/s$ (WPS2000 Inc. 2015)). The *cut-in speed* in turn will depend on the mechanical factors (e.g. blade construction and size, gear train friction) and electrical factors (e.g. cogging torque, load). Latoufis et al. (2012) observed that the rotor needs an initial gust of *higher* wind speed to start rotating.
- Required generator frequency f for given rotor RPM will set the number of poles, and the number of magnets.
- Physical distance between magnets is set by the *magnet width* (pole arc or pole width) to *pole pitch* ratio. The recommended values (Latoufis et al. 2012):

$$\alpha_i = \frac{\text{magnetwidth}}{\text{polepitch}} = \frac{w_m}{\tau_p} \approx 0.4 - 0.7 \quad (3.7)$$

Where the *pole pitch* is (Gieras et al. 2008):

$$\tau_p = \frac{2\pi r}{2p} = \frac{\pi r}{p} \quad (3.8)$$

- The *inner-to-outer PM radius* or *inner-to-outer PM diameter* ratio (set by radial magnet dimension) should be low as this maximises the active area:

$$k_d = \frac{R_{in}}{R_{out}} = \frac{D_{in}}{D_{out}} \quad (3.9)$$

- To minimise attraction magnetic forces between magnets and stator (cored) the outer generator diameter should be as small as possible without sacrificing performance. If the AFPM machine is intended for use as a motor a larger output diameter is preferred for higher torque. Theoretically, to maximise the electromagnetic torque the k_d should be set to $k_d = 1/\sqrt{3}$. Experimentally though, as clarified by (Gieras et al. 2008), the maximum torque is for $k_d \neq 1/\sqrt{3}$.
- The output voltage waveform will be closer to sinusoidal if the inner shape and dimension of coils match the shape and dimension of the magnets used (Latoufis

et al. 2012). At the same time (Latoufis et al. 2012) points out that if the output voltage of the generator is rectified before being supplied to the load, then the increase in harmonic content caused by the rectifier means that “achieving a sinusoidal EMF while designing the generator, will probably have no significance in the performance of the small wind turbine system”.

- The number of the stator coils and rotor poles should be different to provide starting torque for motors and also the reduction of torque pulsations for generators (Gieras et al. 2008).
- Cooling the winding would allow for higher current density. The maximum allowable temperature for the stator material should not be exceeded. Changing winding packing factor, therefore, will directly affect the *heat flux* [W/cm^2] and the maximum generator current (Latoufis et al. 2012). Additionally, the magnets’s temperature should be kept below the recommended for the PM type and grade maximum, as to prevent the reduced performance of the AFPM machine.

3.5 AFPM with Circular Magnets and Coils

There several commonly used shapes used rotor magnetic circuits. They are trapezoidal, circular or semicircular. The PMs shape and the distance between adjacent magnets will determine the distribution of the air gap magnetic field and the harmonics content (quality) of output voltage (Gieras et al. 2008). Usually PMs are surface magnets attached to a ferromagnetic core which helps to complete magnetic circuit.

With circular shape magnets the diameter of PMs restricts the active area, which for a set number of poles is closely related to the pole pitch (Bumby & Martin 2005). This could lead to comparatively large diameter machines with small active area. The problem can be reduced by using trapezoidal magnets where pole pitch and active length can be decoupled from each other (Bumby & Martin 2005).

(Fei et al. 2010) designed a high-speed (20000rpm rated) AFPM with circular magnets. The chosen structure was Double-Sided Internal Stator (Figure 3.6. A total of 6 circular concentrated coils are set in nonferromagnetic and non-conductive epoxy resin to form a 3-phase system (2 coils in series per phase). 8 magnets per rotor side (total of 16) are fixed in aluminium holders (for rotor integrity at high speed) with iron backing to

complete magnetic path.

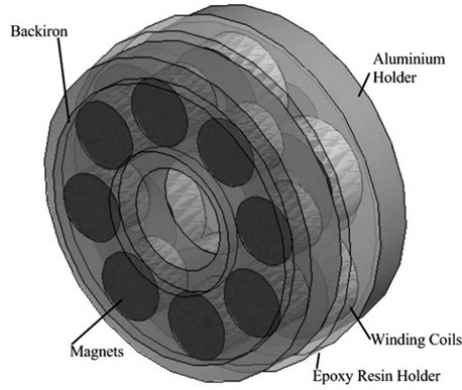


Figure 3.6: High speed Double-Sided Internal Stator AFPM with circular magnets. (Adapted from Fei et al. (2010)).

The stator magnetic field distribution for the circular PMs is believed to have the peak value corresponding to the centre of magnets and falling off in sinusoidal fashion. In circumferential direction this becomes a continuous sinusoid with a radius of half of the rotor pole pitch. In the radial direction (both inwards and outwards from the magnets centre) it will fall to zero. The following analytical formula (Equation 3.10) can be used for estimating the peak flux density (Fei et al. 2010):

$$B_{peak} = \frac{4B_r \sin(pR_m/2R_c) \sinh(pl_m/2R_c)}{\pi\mu_r \sinh(p(2l_m + g)/4R_c)} \quad (3.10)$$

where,

B_r – magnet remanence,

μ_{rrec} – relative recoil magnetic permeability,

R_m – radius of the circular magnets,

R_c magnet placement circle radius,

l_m axial length of the magnets,

g physical air gap, and

p – number of poles.

Experimentally, the sinusoidal EMF output with negligible higher harmonics has been achieved (Table 3.3), proving that the assumption of the sinusoidal flux distribution is valid assumption.

The geometry of armature coils plays an important role in establishing machine reactance,

Table 3.3: Harmonic content of line EMF for generator with circular magnets and circular coils. (Data adapted from Fei et al. (2010))

Harmonic	Fundamental	5th	7th	11th	13th	17th	19th
Line EMF (V)	79.0	0.241	0.356	0.112	0.303	0.424	0.305

generated EMF and ultimately the output power. For the circular coils of fixed outer diameter of 25mm with constant available winding package factor (30% for the multi-strand Litz wire) the variation of inner diameter will provide the opportunity to change the number of turns in a coil and the flux linkages. The optimal coil inner diameter for 16mm diameter PMs placed on 50mm diameter circle is found to be 7mm. The graph of the output power versus the variation in the inner coil radius expressed as normalised value is shown in Figure 3.7.

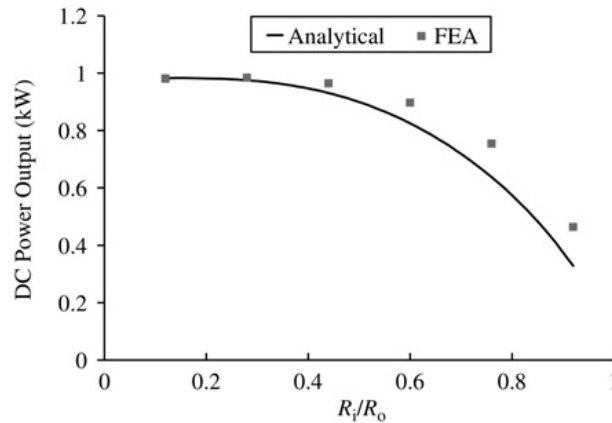


Figure 3.7: Power Output vs circular Coils Inner Radius R_i , normalised to the Outer Radius R_o . It is used in Double-Sided Internal Stator AFPM with circular PMs. (Adapted from Fei et al. (2010)).

3.6 Manufacturing data

AFPM machines are made commercially and available to purchase. Currently (Apr 2015) there is a range of different machines available including made specifically for wind generation. “U-POLEMAG Industry Limited” offers a range of Coreless PM vertical wind generators (U-POLEMAG Industry Limited 2015). The power range offered is as follows:

- 1-5kW wind turbines as Single-Sided AFPM,
- 5-50kW turbines as Double-Sided External Stator,

- Above 50 kW as Radial Flux PM Generator.

AFPMG-380 model from this company is rated to deliver 1kW output, at rated 180rpm, weight of 32kg and $< 0.3Nm$ of stator moment.

Another typical product available is a complete wind generator assembly which would have an internal AFPM machine. The most common type is a Vertical Axis Wind Turbine (VAWT) which allows for utilisation of the flat construction of axial flux generator. The 5kW Coreless wind generator offered by “WPS2000 Inc” has the following main features (WPS2000 Inc. 2015):

- 3 phase coreless PM,
- 3m/s cut-in speed,
- 15m/s rated wind speed,
- 100-400V DC output,
- 380kg generator weight,
- 120kg rotor weight.

The power and voltage outputs versus Rpm are shown on Figure 3.8.

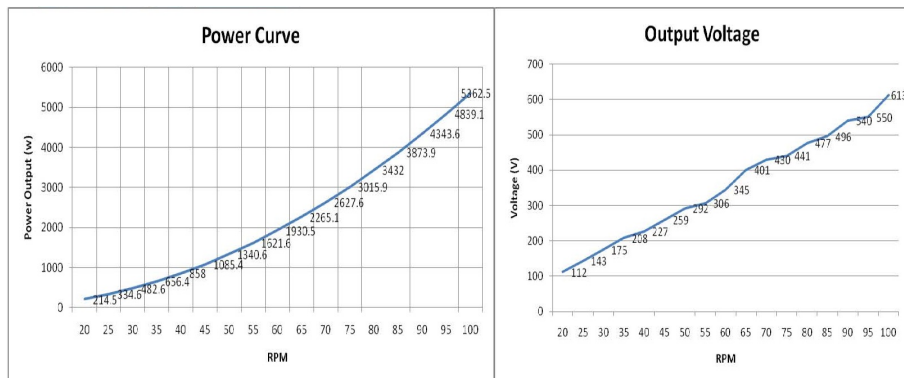


Figure 3.8: “WPS2000 Inc” 5kw VAWT power and voltage outputs versus RPM. (Adapted from WPS2000 Inc. (2015)).

Chapter 4

Methodology

This chapter outlines the methodology of the research project. It covers phases of design, construction, testing and the theoretical performance of proposed brushless *Single-rotor/Double-Stator* AFPM machine.

4.1 Design

The Single-rotor/Double-stator configuration (also known as *Axial Flux Internal Rotor* (AFIR) or *Double-Sided External-Stator*) has been chosen due to availability of only 8 magnets for this research project. As mentioned earlier, this particular configuration has the advantage of needing less PMs at the expense of poor winding utilisation and is not considered to be an advantageous machine topology. As a result, little performance information is available for this AFPM arrangement.

Double sided configuration does help to balance axial forces which is a big factor in AFPM. In addition there is a degree of flexibility in coils distribution across two sides (or two halves) of the stator.

Since the magnetic flux does not need to travel through the rotor structure the magnetic type material is not used to hold the rotor magnets. A polyester epoxy is used for the rotor base material. This makes the rotor lighter in weight (increasing power to inertia ratio), eliminates rotor core losses and reduces the cogging torque.

The circular shape of the magnets (pole faces) is ideal for generating sinusoidal waveforms. The added benefit of the the circular pole faces is a reduction in the cogging torque. As mentioned in the literature review, this occurs due to the whole edge of the magnet not moving in front of the stator core (in case of cored machine) at the same time.

The armature winding is chosen to be a three phase type in order to maximise the output and reduce pulsating torque. The coils of the winding are distributed between both sides of the stator. The two phase winding is possible and its performance can be evaluated in the future work.

The machine's structure and all supplementary hardware of the machine is constructed from non-magnetic materials (aluminium, stainless steel, plywood) with the intention to reduce the typical losses associated with an electrical machine and to minimise the structure's contribution towards creating the cogging torque. Additionally, insulation between different parts of the machine is included to reduce any circulation currents.

Prototype variants

Due to little available data for *Double-Sided External-Stator* structure, to identify benefits (or equally weaknesses) of this AFPM setup, several prototype variants are needed. The rotor change is not feasible during this research project as it would require resetting the magnets which is a very time-consuming process. However, several different stator configurations are possible and are relatively easy to implement.

For the same rotor several stators with exactly the same dimensions need to be manufactured. The proposed stator structures for performance evaluation and comparison are:

- A stator containing no electrical conductors (for losses evaluation). This is identified as a *Blank Stator* within the project.
- A coreless ribbon wire winding. This is identified as a *Stator 1* within this project. And,
- A magnetic non-conductive powder composite backing with ribbon wire winding, which is called a *Stator 2* or a *Composite Stator* within the project. The magnetic backing was achieved by mixing *magnetic non-conductive iron powder* with polyester resin (at 50% concentration). The total thickness of 10mm was achieved for the magnetic backing (more information is provided in Appendix C.3).

4.2 Rotor Design

To achieve a low RPM operation (suitable for wind generation applications) a large number of poles is required. Therefore, the maximum number of available magnets (8) is used for the rotor.

$$\begin{aligned}
 &\text{Number of poles } 2p = 8 \\
 &\text{Number of pole pairs } p = 4 \\
 &\text{Electrical Degrees in 1 revolution } 360^\circ \text{Mech} = 360 * 4 = 1440^\circ \text{Elec} \\
 &360^\circ E = 90^\circ M \\
 &120^\circ E = 30^\circ M \\
 &\text{Pole pitch in mechanical degrees} = \frac{360}{8} = 45^\circ M
 \end{aligned} \tag{4.1}$$

The cylindrical shape magnets available for the project have the following dimensions: $diameter_m = w_m = 22mm$ and $height = axial\ thickness = h_m = 25.4mm$. The magnets grade is unknown. Therefore the rotor is constructed first (with all magnets set in place) and then the distribution of the magnetic field (flux density) is measured using Model 455 Gaussmeter (*Lake Shore Cryotronics, Inc*).

To improve the volume to power efficiency, the magnets are mounted as close to one another as possible, therefore the minimum physical dimensions for the machines rotor are produced. There are physical limitations to the minimum size possible that are specific to the AFPM construction:

- There should be enough core material (polyester resin) to support the magnets and maintain the structural integrity against forces of magnets themselves and forces between the stator and the rotor,
- The rotor shaft (aluminium) diameter should be large enough to prevent excessive deflection during operation $D_{shaft} = 20mm$, and
- The connection point (polyester resin set onto aluminium bushing) of the rotor disc to the shaft should withstand the maximum imposed torque $D_{bush} = 35mm$.

Figures 4.1 and 4.2 show the *Rotor principle dimensions* and *Rotor Bushing dimensions* respectively. The figures were produced using MATLAB program listed in Appendix D.1

and the drawings were used to manufacture the rotor. The parts list is provided in Appendix C.1 and steps of the rotor manufacturing process are outlined in Appendix C.2.

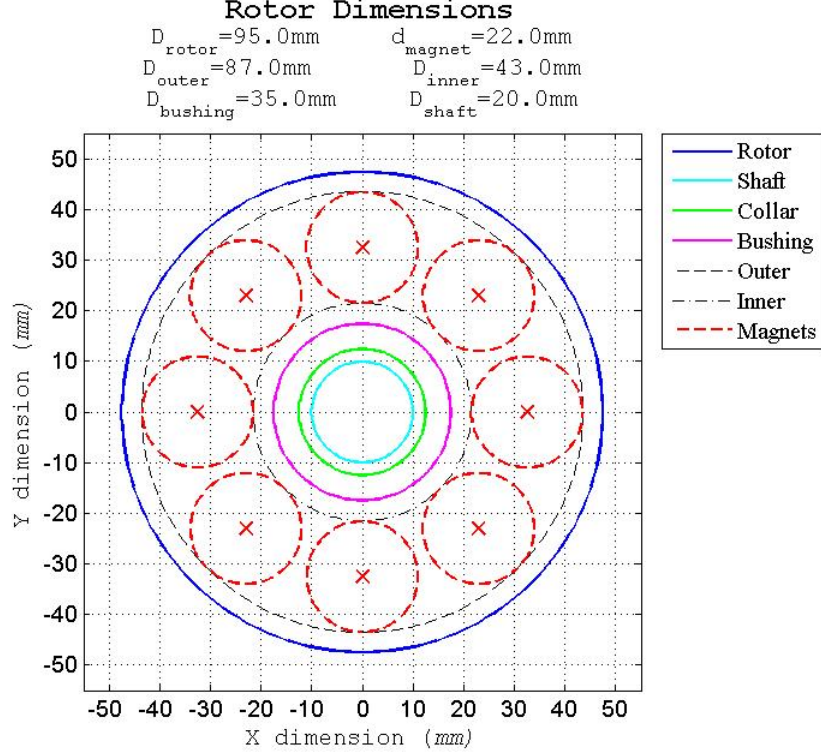


Figure 4.1: Axial view of the rotor. Rotor's principle dimensions are shown. The position of the 8 magnets are drawn in red with crosses indicating their centre points. An appropriately scaled version of this figure was used as a template for magnets' holes positioning.

The following are the AFPM parameters related to the rotor.

- The average diameter of the rotor (based on the inner and outer PM diameters):

$$D_{av} = \frac{D_{out} + D_{in}}{2} = \frac{43 + 87}{2} = 65\text{mm} = 0.065\text{m} \quad (4.2)$$

- The inner-to-outer PM diameter ratio is:

$$k_d = \frac{D_{in}}{D_{out}} = \frac{43}{87} \approx 0.494 \quad (4.3)$$

- Since the magnet diameter is set, the pole pitch is:

$$\tau_p = \frac{\pi D_{av}}{2p} = \frac{\pi 65}{8} \approx 25.53\text{mm} = 0.02553\text{m} \quad (4.4)$$

- Physical distance between magnets expressed as a *magnet width* (pole arc or pole width) to *pole pitch* ratio is:

$$\alpha_i = \frac{\text{magnet width}}{\text{pole pitch}} = \frac{w_m}{\tau_p} = \frac{22}{25.53} \approx 0.86 \quad (4.5)$$

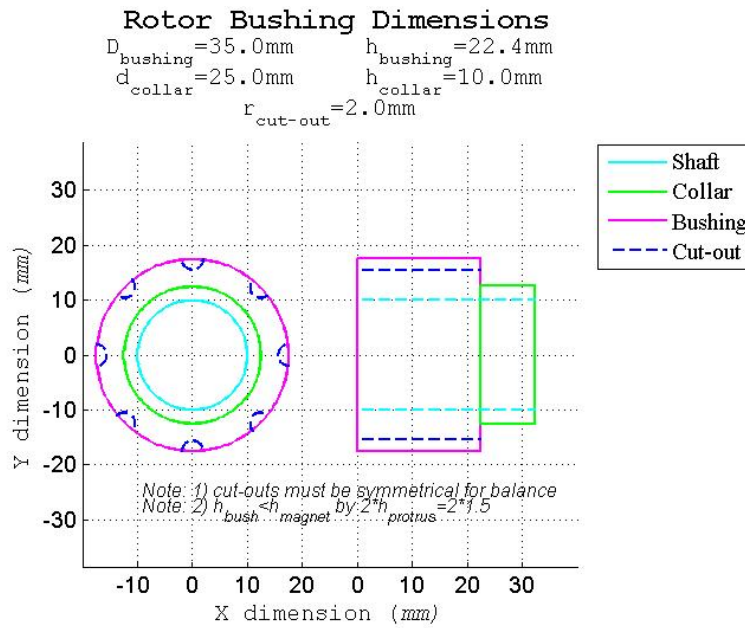


Figure 4.2: Axial and side views of the rotor bushing. The aluminium rotor bushing is the connection point between the rotor structure (polyester resin) and the aluminium shaft. The symmetrical cut-outs aim to strengthen the adhesion point of polyester resin to the aluminium.

The manufactured rotor pressed on an aluminium shaft is shown in Figure 4.3.

Net physical flux of the rotor is measured using the *DSP Gaussmeter* (Appendix C.4 item 1). The typical set-up is shown in Figure 4.4, where probe is supported in a vice allowing for more accurate results. The results of the measurements are presented in Figures 4.5 and 4.6. It must be mentioned here that there is a variation in magnetic flux produced by different poles (possibly due to magnets manufacturing tolerances, magnets' age and asymmetrical poles positioning on the rotor disc). The variation in magnetic flux from pole to pole was estimated to be about 10%. Therefore, the measurements were taken on a pole with the maximum magnetic flux.

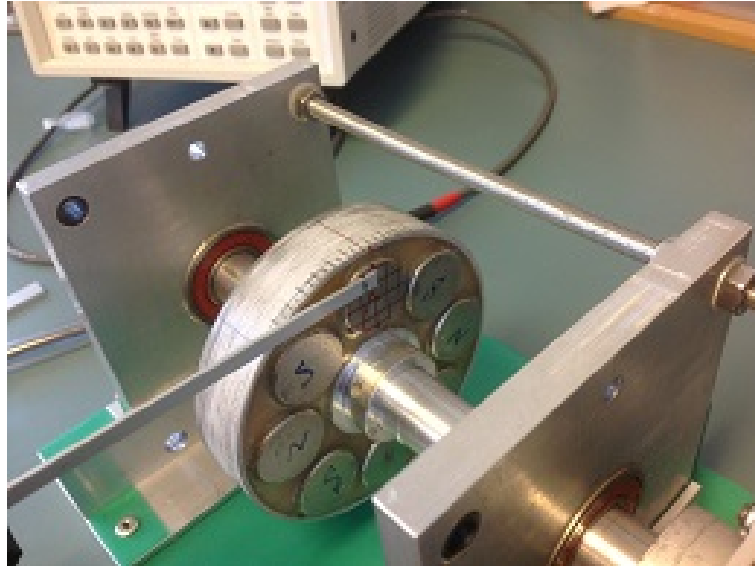


Figure 4.3: Manufactured rotor pressed on an aluminium shaft.

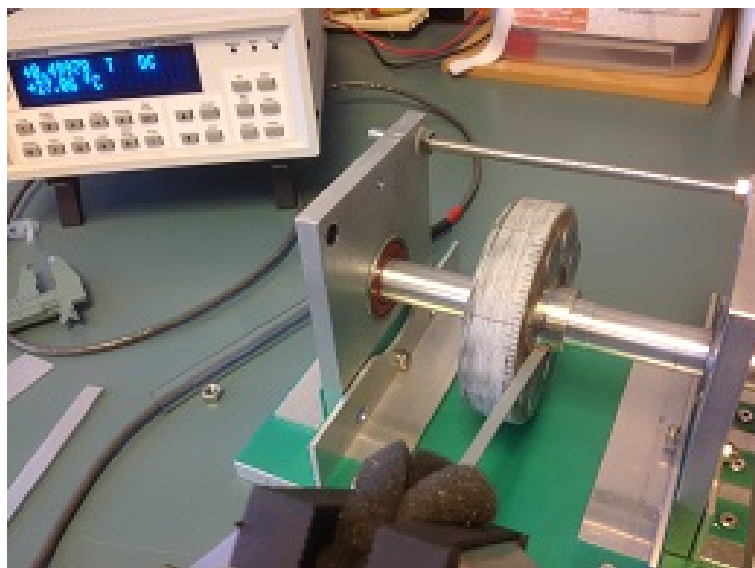


Figure 4.4: Typical set-up for magnetic flux measurements.

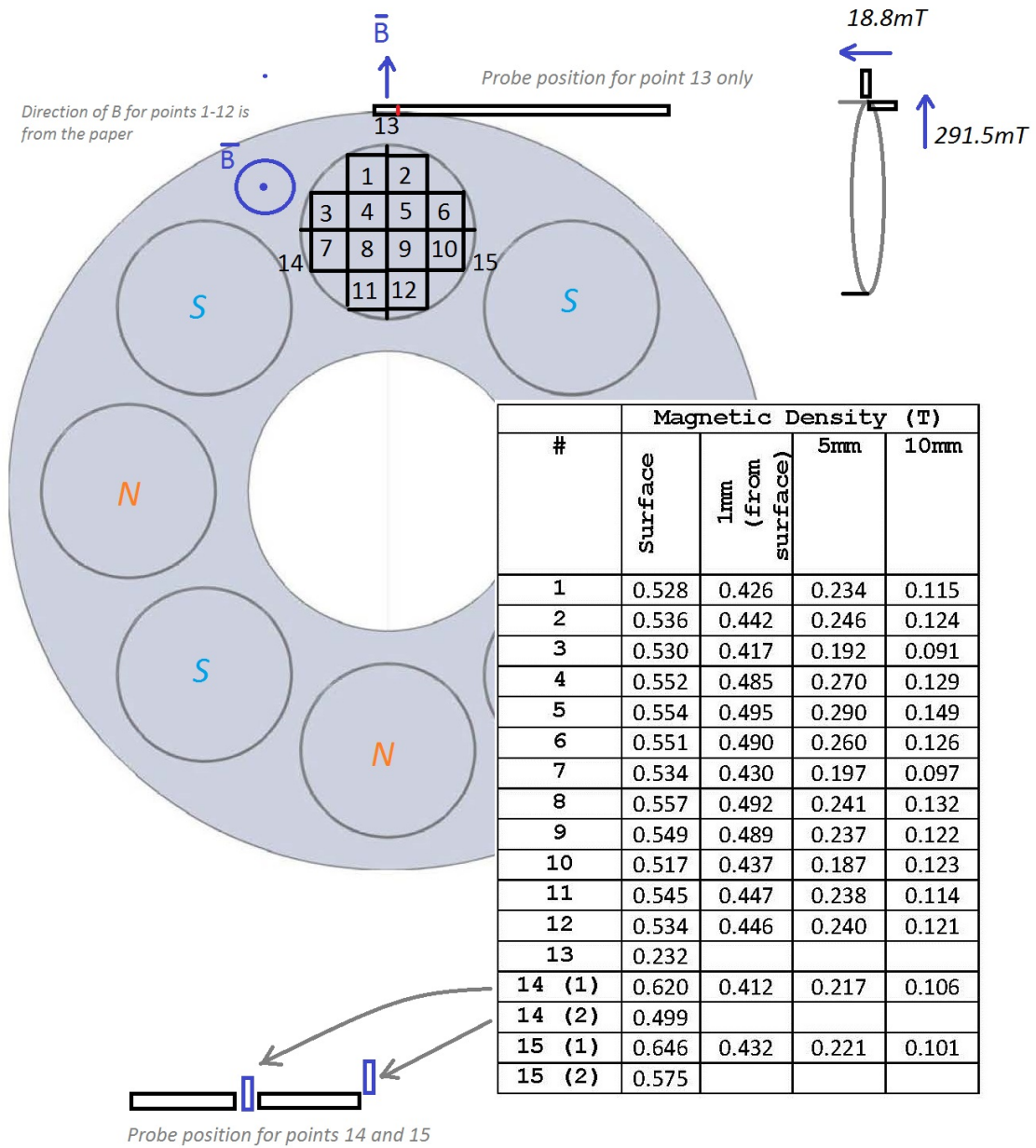


Figure 4.5: Net magnetic flux out of the poles of the rotor (axial direction).

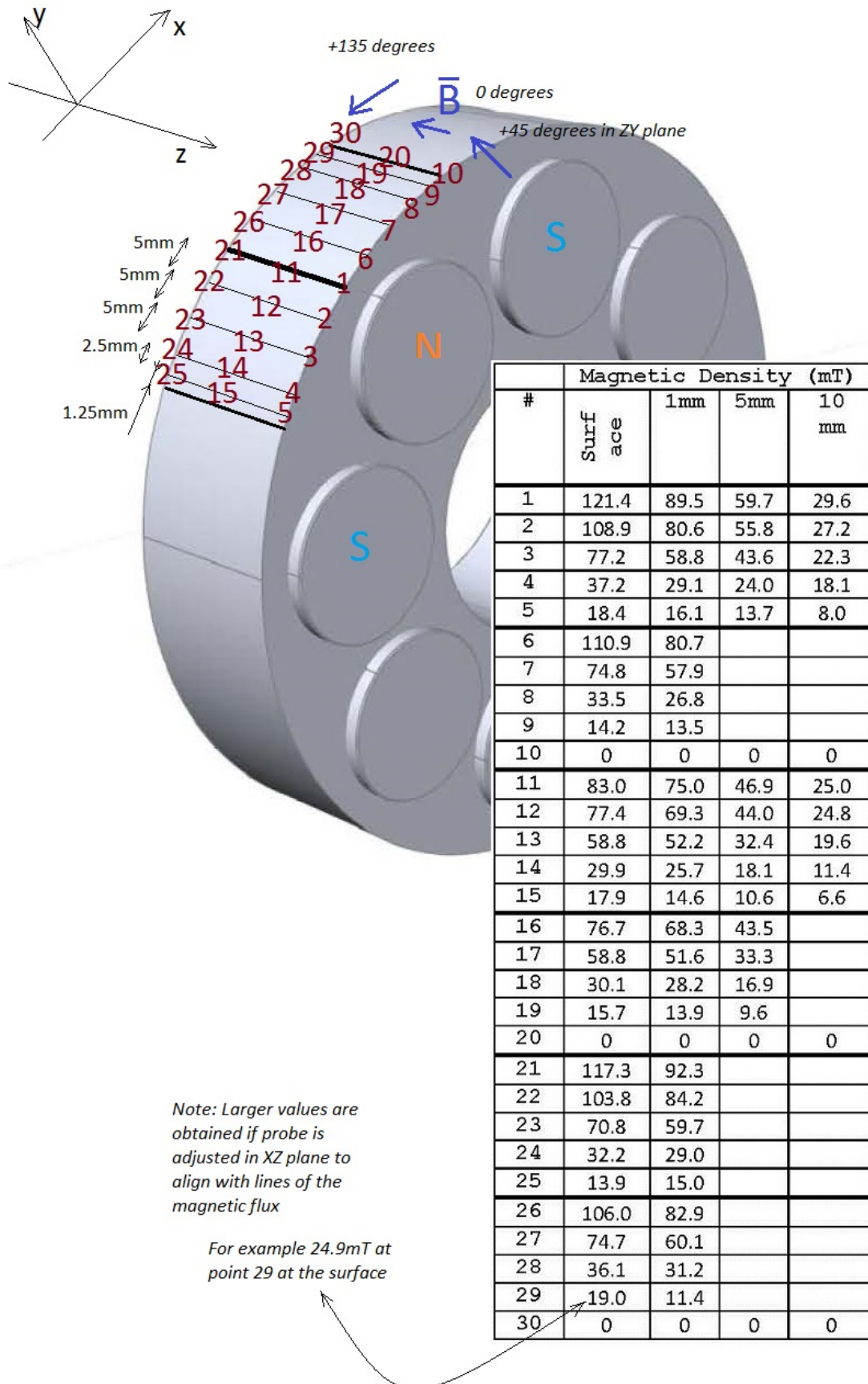


Figure 4.6: Net magnetic flux along the side of the rotor.

4.3 Stator Design

Once the rotor dimensions are set the stator winding of the *Single-Rotor/Double-Stator* AFPM can be considered. The stator features are as follows:

- Dual Stator means the stator has two halves on both sides of the rotor, balancing the axial forces acting during AFPM operation.
- Stator Coils can be distributed across both sides.
- With the absence of physical slots in the stator, concentrated coils are used. Double-layer style (side by side coils, two sides of different coils are in the same slot) winding is used to maximise the use of available space. To maximise the packing factor (especially for ribbon style winding) a non-overlap style is also employed. Therefore, the winding is *concentrated, double-layer, non-overlap*.
- The arc taken by a middle of a coil (coil pitch τ_c) is taken to be equal the pole pitch (τ_p) (Figure 4.10). For the double layer, non-overlap winding the coil span angle $\theta_c = 60^\circ$. Red lines in Figure 4.10 show the limits: the radial parts indicate the coils span limits and the circumferential part (shown for one coil span only) runs along the Rotor Bushing Collar, which physically limits the extent of coil conductors.
- With the coil span angle $\theta_c = 60^\circ$:

$$\begin{aligned} \text{Number of coils per stator side} &= 360^\circ/60^\circ = 6 \text{ coils} \\ \text{Total number of coils (both sides)} &= 12 \text{ coils} \end{aligned} \tag{4.6}$$

This confirms that the number of coils is not equal to the number of the magnets, to provide starting torque for motors and the reduction of torque pulsations for generator operation.

- For the 3 phase system and 12 stator coils in total there are:

$$\begin{aligned} 4 \text{ coils per phase (Figure 4.7)} \\ 2 \text{ coils per phase per side (Figures 4.8 and 4.9)} \end{aligned} \tag{4.7}$$

- Investigating dimensions corresponding to the view in Figure 4.10 suggests the maximum clearance between “single loop” winding (shown in black dashed bold), along the circle drawn through the magnets’ centres, is 8.51mm (rounded to 8mm).
- Single coil boundaries within the coil span angle of $\theta_c = 60^\circ$ are shown in Figure 4.11. The single loop coils are shown in black dashed bold and the physical boundaries for one coil are in red. The boundaries limit the coils extension beyond the *rotor bushing collar* and mark the borders in the space between adjacent coils. There is

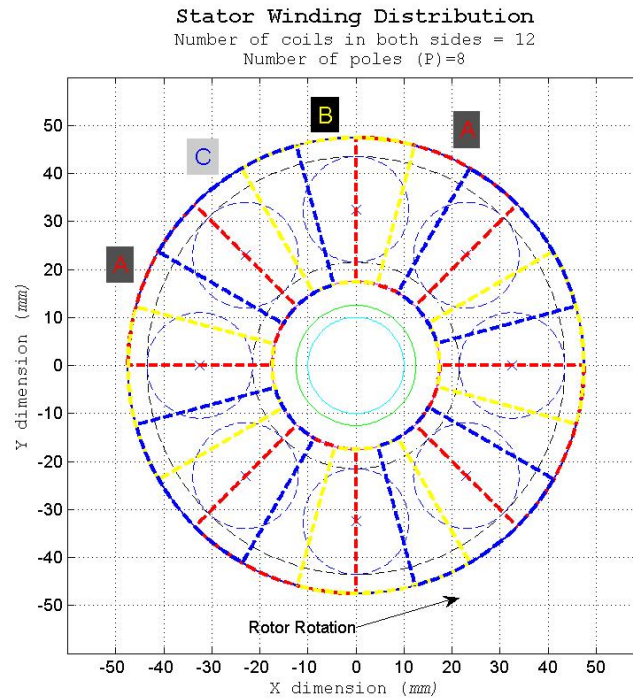


Figure 4.7: Stator Winding Distribution across both sides. Phases *A*, *B* and *C* are shown in *red*, *yellow* and *blue* respectively. The rotation of rotor is counterclockwise. For *8pole* machine $360^\circ Elec = 90^\circ Mech$. There are 4 coils per each phase.

more room at the outer stator diameter , however, increasing coils in this direction will increase copper usage and copper losses.

- Shape of the coils is *trapezoidal* (Figure 4.11). It was stated earlier that the output voltage waveform will be closer to sinusoidal if the inner shape and dimension of coils match the shape and dimension of the magnets used. However, the trapezoidal shape was preferred in this design for reasons of increased EMF (increased active area and packing factor at the cost of increased *long ends* and copper losses) and increased torque for motor operation. The inner dimensions of the trapezoidal winding, on average, match the dimensions of the magnets. The inner dimensions of the trapezoidal coil can be adjusted (if needed and within the *coil span angle*) to change the number of turns, the inner coil dimension or the outer coil dimensions to fine tune the optimum performance. Additionally, comparing the directions of the radial black dashed lines with red coil boundaries in Figure 4.11, a degree of conductor skewing against the center line of the pole face is evident. This in theory should improve the output wave towards the sinusoidal shape.
- The centres of coils (in case of coreless structure) can be drilled out to effect an extra cooling.

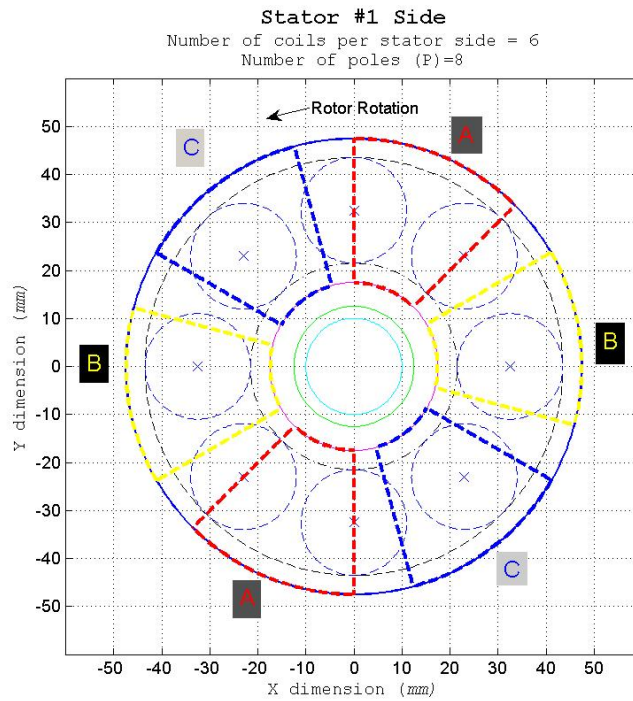


Figure 4.8: First half (side) of the stator coils. There are 6 coils per stator side, with 2 coils belonging to each of the phases *A*, *B* and *C*.

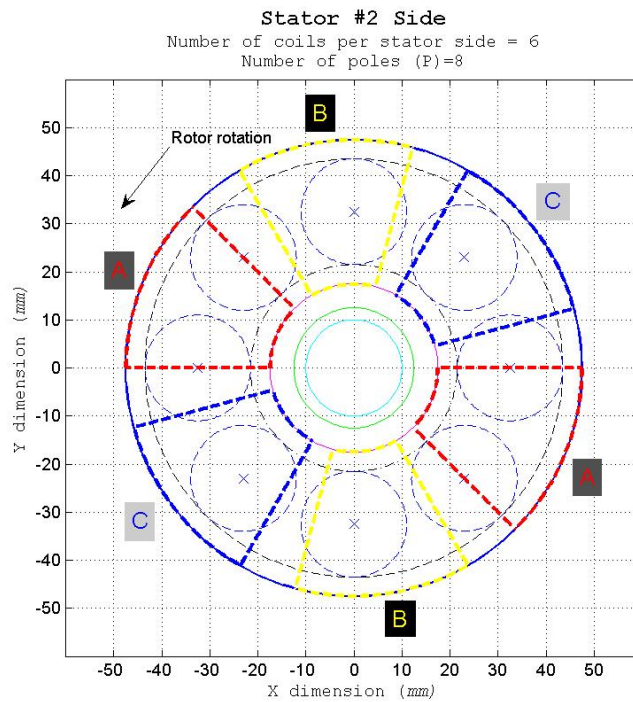


Figure 4.9: Second half (side) of the stator coils. The coils in this side are physically offset by $30^\circ Mech = 120^\circ Elec$ compared to coils in Figure 4.8. Rotation of coils in Figure 4.8 by $30^\circ M$ anticlockwise (in the direction of rotor rotation) changes *A* to *B*, *C* to *A*, and so on.

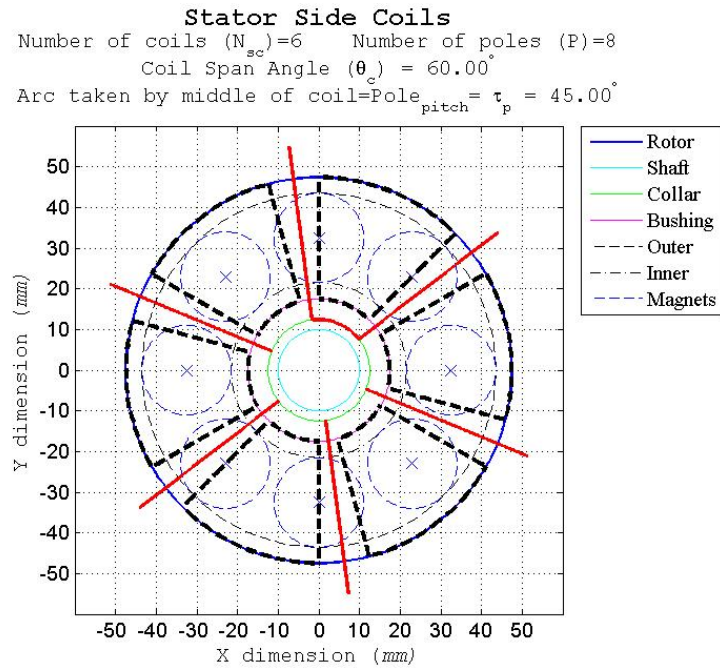


Figure 4.10: One half (side) of the stator coils and physical limits. Stator coils limits are super positioned onto the axial view of the rotor. The single loop coils are shown in black dashed bold and the physical boundaries for individual coils are in red. The boundaries limit the coils extension beyond the *rotor bushing collar* and mark the borders in the space between adjacent coils. The figure was produced using MATLAB program listed in Appendix D.2

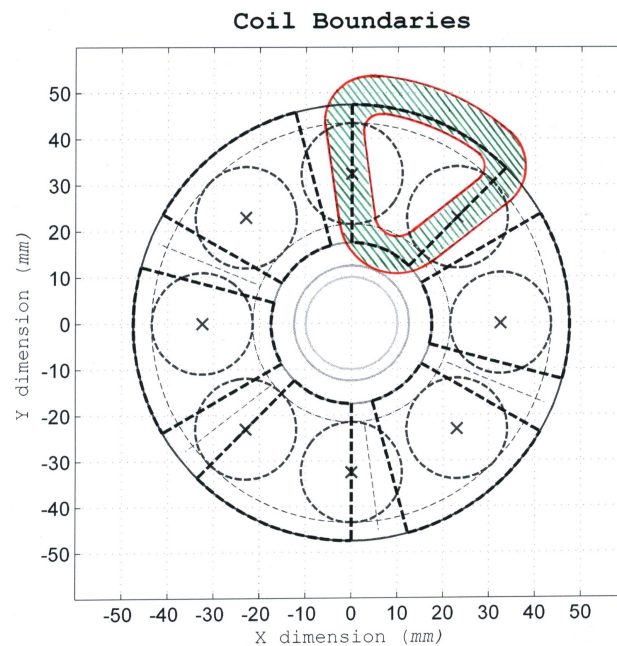


Figure 4.11: Single coil boundaries within the coil span angle of $\theta_c = 60^\circ$. The coil is super positioned onto the axial view of the rotor. The thickness of coil is 8mm allowing for 0.5mm clearance between adjacent coils.

Conductors

In line with the proposed prototype variants *Ribbon Wire* conductor profile is needed for stators manufacturing.

Andreas Helwig has locally manufactured the ribbon conductors by rolling a round wire between two rollers. The prerequisite of this manufacturing method is that an original round wire has to have a larger active area than finished ribbon conductor.

Ideally stator coils should be manufactured using conductors with the same active areas for easy prototype performance comparison (packing factor, EMF, losses). However, due to limitations of local manufacturing the dimensions of ribbon conductors can be only approximated to one of the standard round copper wires cross section areas.

The general process for estimating the number of turns N_c in a coil, common to the both types of conductors(round and ribbon), involves the following steps:

- 1) Estimation of available for a coil space within the stator. Coil span angle $\theta_c = 60^\circ$, required coil inner dimension and other specific physical limitation (*rotor bushing collar* in this case) produces the maximum available width of coil conductors in circumferential and radial directions (as on the axial view of Figure 4.11) — $w = 8mm$. The axial depth of the coil conductor space is determined from the required air gap g and the distribution of the magnetic field within the air gap. The optimum axial depth is estimated to be $a = 5mm$.
- 2) The area of space occupied by single conductor depends on its external dimensions:

$$\text{Round wire with diameter } d: A_{round} = d^2$$

$$\text{Ribbon wire with } W_{ribbon} \text{ and } H_{ribbon} \text{ (Figure 4.13): } A_{ribbon} = W_{ribbon} * H_{ribbon} \quad (4.8)$$

- 3) The number of loops within available volume can be estimated by dividing $w * a$ by the area occupied by a single conductor.

Conductor Active Area.

Active cross-section area (area less insulation) of the round wire can be found using standard manufacturers data. Since the ribbon wire is locally manufactured the estimation of its active area is as follows:

- 1) Estimate the height H_{arc} and width W_{arc} of end circular segments (Figures 4.12 and 4.13):

$$\begin{aligned} W_{arc} &= H_{ribbon} - 2 * insulation \\ H_{arc} &= \frac{W_{ribbon} - w1}{2} - insulation \end{aligned} \quad (4.9)$$

- 2) Find radius of the end segment from the base (W_{arc}) and the height (H_{arc}) of the end arcs (Page 2015):

$$R_{arc} = \frac{H_{arc}}{2} + \frac{W_{arc}^2}{8 * H_{arc}} \quad (4.10)$$

- 3) Find area an end circular segments from arc's radius (R_{arc}) and height (H_{arc}) (Page 2015):

$$A_{arc} = R_{arc}^2 \cos^{-1} \left(\frac{R_{arc} - H_{arc}}{R} \right) - (R_{arc} - H_{arc}) \sqrt{2R_{arc}H_{arc} - H_{arc}^2} \quad (4.11)$$

- 4) Active cross-section area of ribbon wire:

$$A_{active} = w1 * W_{arc} + 2 * A_{arc} \quad (4.12)$$

Locally manufactured ribbon wire

For the locally manufactured ribbon wire shown in Figure 4.12:

- External dimensions are:

$$\begin{aligned} H_{ribbon} &= 1.07mm \quad (\approx 265units) \\ W_{ribbon} &= 2.16mm \quad (\approx 555units) \\ 1unit &\approx 0.00395mm \\ Insulation &= 0.02mm \end{aligned} \quad (4.13)$$

- The height H_{arc} and width W_{arc} of end circular segments (Figures 4.12 and 4.13):

$$\begin{aligned} W_{arc} &= H_{ribbon} - 2 * insulation = 1.07 - 2 * 0.02 = 1.03mm \\ H_{arc} &= \frac{W_{ribbon} - w1}{2} - insulation = 0.25675 - 0.02 \approx 0.24mm \end{aligned} \quad (4.14)$$

- Active cross-section area of ribbon wire:

$$A_{active} \approx 2.04mm^2 \quad (4.15)$$

- The area of space occupied by single conductor based on the external dimensions:

$$A_{ribbon} = W_{ribbon} * H_{ribbon} \approx 2.31mm^2 \quad (4.16)$$

- Number of turns in the single layer of a coil that can fit into the available coil space:

$$N_{layer} = \frac{8mm}{H_{ribbon}} = \frac{8mm}{1.07} \approx 7.48 \quad \text{turns} \quad (4.17)$$

As the actual design conductor space available is $w = 8.51mm$, to increase the number of turns to 8 the inner dimension of the coils is reduced by $1mm$. This allows for $0.5mm$ between coils, 8 turns per coil per layer and possible variation in conductor dimensions:

$$N_{layer} = \frac{(9.5 - 0.5)mm}{H_{ribbon}} = \frac{(9.5 - 0.5)mm}{1.07} \approx 8.43 \quad (\text{rounded to 8 turns}) \quad (4.18)$$

- Total number of turns per coil (2 layers) = $8 * 2 = 16$ turns.
- The best theoretically possible coil packing factor (assuming the axial depth $a = 2 * W_{ribbon}$ and coil width $w = 8mm$):

$$\frac{A_{active} * 16}{2 * W_{ribbon} * w} = \frac{2.04 * 14}{2 * 2.16 * 8.53} \approx 0.88 \quad (4.19)$$

- The standard round wire with the closest active cross section area is **AWG14** with *active cross section area* = $2.08mm^2$.

The ribbon conductor coils fabrication, in accordance with method proposed by Andreas Helwig, is as follows:

- individual single layer coils are wound first,
- two single layer coils are aligned so that the conductor winding direction of both layers is the same (i.e. the number of coils adds), and the layers can be joined together with tape and adhesive,
- the inner ends are soldered and insulated,
- the outer ends are readily available for external connection.

During the actual manufacturing tape was not used to secure individual coils to minimise the air gap. The individual (single layer) coils were set in Araldite first before joining two layers together again with Araldite. The tape was used to secure the ends of the double layer coil during setting the coils in the polyester epoxy.

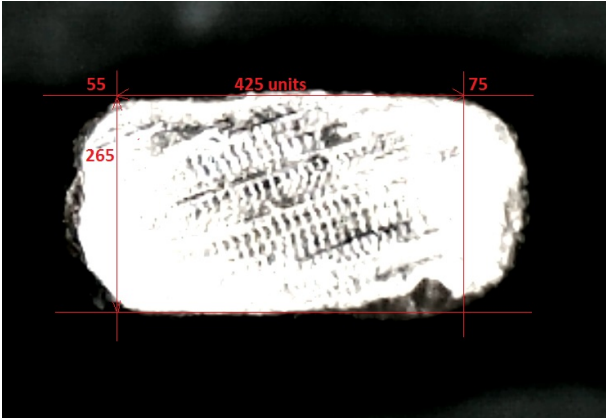


Figure 4.12: Magnified view of a typical manufactured ribbon conductor. Ribbon produced by rolling a round wire. The external dimensions are easily determined using vernier calipers. The height of the end arcs H_{arc} is estimated using USB microscope (item 2 in Appendix C.4).

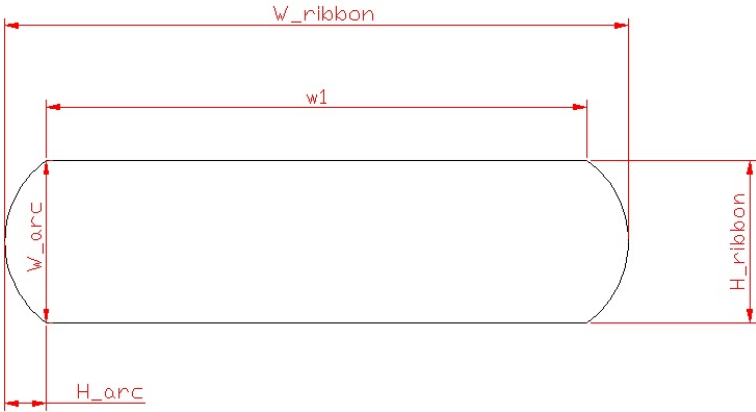


Figure 4.13: Dimensions of the manufactured ribbon wire used for calculations its active area and number of turns.

Stators manufacture

A wound coil with 8 turns is shown in Figure 4.14. Two single layer coils joined together with inner conductors soldered and outer conductors available for external connection is shown in Figure 4.15. And a manufactured stator side (coils set in a polyester epoxy) is shown in Figure 4.16.



Figure 4.14: A wound coil with 8 turns.

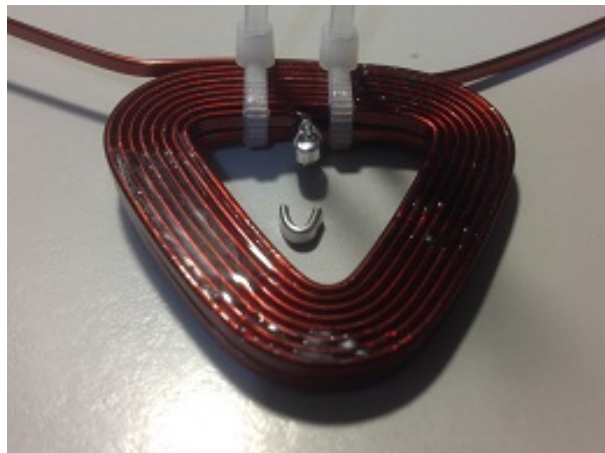


Figure 4.15: Two single layer coils joined together with inner conductors soldered and outer conductors available for external connection. A tinned clip made of ribbon wire used for soldered joints is also shown.

The jig for stator manufacturing was made based on drawing shown in Figure 4.17. The parts list is provided in Appendix C.1 and steps of the stator manufacturing process are outlined in Appendix C.3.

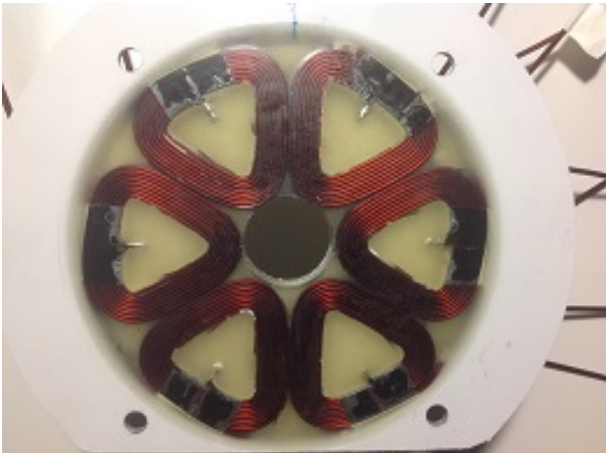


Figure 4.16: A manufactured stator side - 6 coils set in a polyester epoxy.

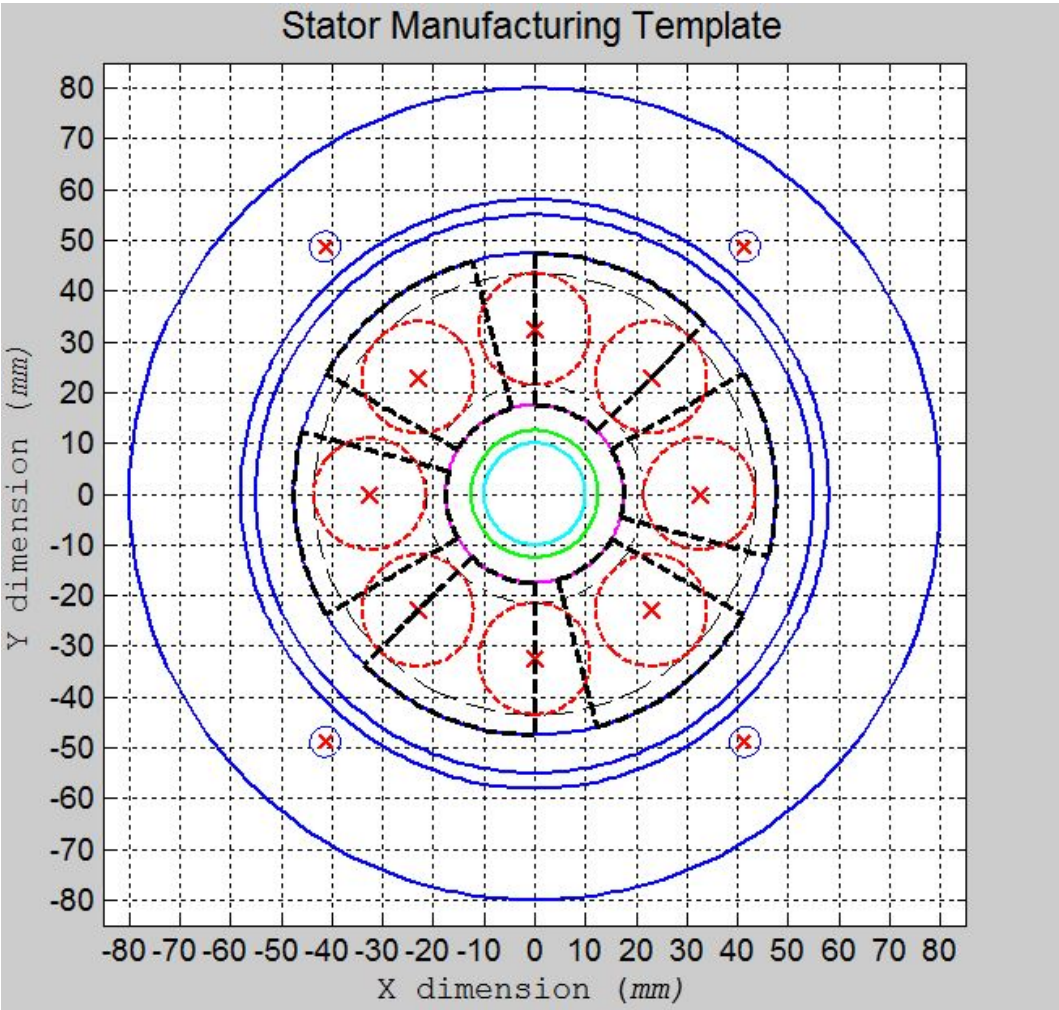


Figure 4.17: Stator manufacturing template.

4.4 Prototype/Test Bed Construction

In general the prototype construction is tailored to aid the maximum output and minimum possible losses from the designed generator.

The physical air-gap between rotor and the stator sides is one of the critical parameters. To make as minimum as possible no protective coating is applied to the pole surfaces of the magnets. This is reasonable for a prototype used in non-corrosive, controlled environment. However, the magnets surfaces would need some protective coating to prevent possible corrosion in the long term.

The insulation between all construction parts is provided to prevent any possible circulating currents ultimately creating interference, opposition torque and affecting the performance. In line with this the extra space between side supports is given to minimise the structure contribution to cogging torque and losses. It also permits the possibility of expanding the AFPD setup to multi disc configuration.

High-speed deep groove quality bearings are chosen to reduce mechanical losses and provide axial stability.

All structural materials and hardware (including the pulley) are non-magnetic type: aluminium, stainless steel or plywood. List of materials is provided in Appendix C.1.

4.5 Testing

To evaluate the machines performance it is driven by a variable speed DC PWM drive coupled via pulleys and a belt. The PWM drive is able to maintain the set speed under varying load conditions.

A load cell sensor is used to measure the input torque. To achieve this, the base plate of the machine is hinged on one side allowing it to rotate in the rotor disc plane and to provide the force on the load sensor.

The machine performance with various stator configuration tested under no load and load conditions at various speeds. The list of test equipment is provided in Appendix C.4. The

following tests were carried out:

- 1) Mechanical losses: windage, bearing and rotor mass losses are estimated using the *blank stator* with no conductors. The *load cell voltage* versus *RPM* characteristic provides the required information in the usable RPM range. Adjusting the *load cell voltage* for generator weight W and the drive belt tension gives the sought mechanical losses.
- 2) Stator winding eddy-current losses can be estimated from no load test and the “mechanical losses” test carried out during previous step. Stator winding eddy-current losses added to the mechanical losses give the machines total losses. Total loss figures allow to carry out a comparison between performances of two types of prototype stators.
- 3) Load test (at varying loads) at low RPM (750RPM or 50Hz is suitable for 8-pole machine) for V-I characteristic for cogging torque determination.
- 4) Load test (at constant load) at variable RPM for Output Power and Efficiency versus RPM performance.
- 5) Direct measuring of inductance and resistance of generator windings (LCR Meter) for the AFPM machine equivalent circuit parameters.
- 6) Generator Temperature measured using IR camera.

A typical experiment set-up is shown in Figure 4.18. The AFPM machine windings are connected in a star configuration. AFPM machine is represented by its equivalent circuit comprising a no-load EMF (E_a , E_b and E_c) and an impedance (Z_a , Z_b and Z_c) in each winding. The output is rectified with a 6-diode rectifier. The circuit is loaded with a variable or a constant value *low* – Ω resistor as required by a specific test. The RMS voltage and current is measured with a multimeter and an ammeter.

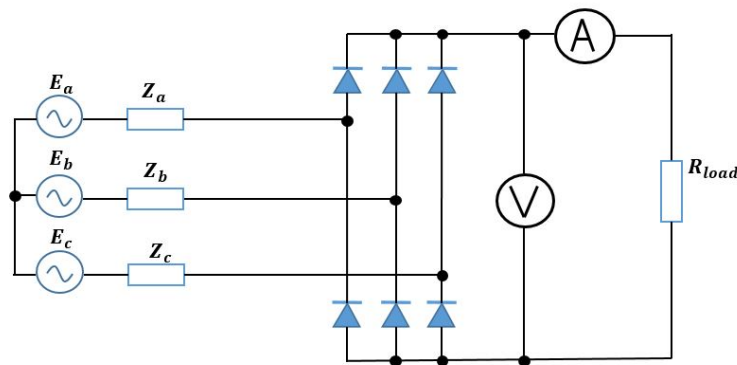


Figure 4.18: A typical experiment set-up circuit diagram.

The comparison of the experimental results between two stator types and the analytical solution is the base for the analysis and suggestions for any future work.

4.6 Theoretical Performance

The theoretical output from the machine is estimated using methods described in Latoufis et al. (2012) and Gieras et al. (2008) as follows.

The measured air gap **peak Magnetic Flux Density** value at a distance of $1mm$ from the pole' surface is taken to be an average of points 4, 5, 8 and 9 (Figure 4.5):

$$B_{mg} \approx 0.49T \quad (4.20)$$

The average magnetic flux density, assuming a sinusoidal magnetic distribution excited by circular poles:

$$B_{avg} = \frac{2}{\pi} B_{mg} = 0.3119T \quad (4.21)$$

The rotational speed is taken as $n = 750RPM$, which represents $50Hz$ for a number of poles $P = 8$ (number of pole pairs $p = 4$):

$$f = \frac{n * P}{120} = \frac{n * p}{60} = \frac{750 * 8}{120} = 50Hz \quad (4.22)$$

The winding factor is estimated to be:

$$k_w = 0.9441 \quad (4.23)$$

The peak value of *flux* based on the average magnetic flux density B_{avg} , the outer PM diameter $D_{out} = 87mm$ and inner-to-outer PM diameter ratio $k_d = 43/87 = 0.4943$:

$$\Phi = \frac{\pi}{8p} B_{avg} D_{out}^2 (1 - k_d^2) \approx 1.7518 * 10^{-4} Wb \quad (4.24)$$

The *instantaneous phase EMF* is proportional to the rate of change of flux linkage. For the fundamental of the magnetic flux $\phi = \Phi \sin(\omega t)$ and number of turns per phase N_s :

$$e = d(N\phi) = N_s k_w \frac{d\phi}{dt} = N_s k_w (2\pi f) \Phi \cos(\omega t) \quad (4.25)$$

The *peak phase EMF* (substituting $f = np/60$) is:

$$\hat{E} = N_s k_w (2\pi f) \Phi = 2\pi N_s k_w \Phi \frac{np}{60} \quad [V/rpm] \quad (4.26)$$

The *peak phase EMF* for $N_s = 64$ and $n = 750rpm$:

$$\hat{E} = 2\pi N_s k_w \Phi \frac{np}{60} \approx \mathbf{3.32V} \quad (E_{rms} = \mathbf{2.35V}) \quad (4.27)$$

For the three phase 6-diode rectifier (with linear voltage V_L and diode voltage drop V_{diode}) the expected mean output is:

$$V_{mean} = \frac{3\sqrt{2}V_L}{\pi} - 2V_{diode} = \frac{3\hat{V}_L}{\pi} - 2V_{diode} \quad (4.28)$$

Therefore, with linear voltage $\hat{V}_L = \hat{E}\sqrt{3} = 5.75V$ and $2V_{diode} = 0.891V$, the expected mean output voltage across the load R_{load} is:

$$V_{mean} = \frac{3\hat{V}_L}{\pi} - 2V_{diode} = \frac{3 * 5.75}{\pi} - 0.891 \approx \mathbf{4.6V} \quad (4.29)$$

Chapter 5

Results

This chapter discusses the results of conducted tests for the three types of stators built (Blank, Coreless and Coreless with Magnetic Composite backing) for *Single-rotor/Double-Stator* AFPM machine during the project.

5.1 Blank Stator Generator

The assembled AFPM generator with blank stators is shown in Figure 5.1.

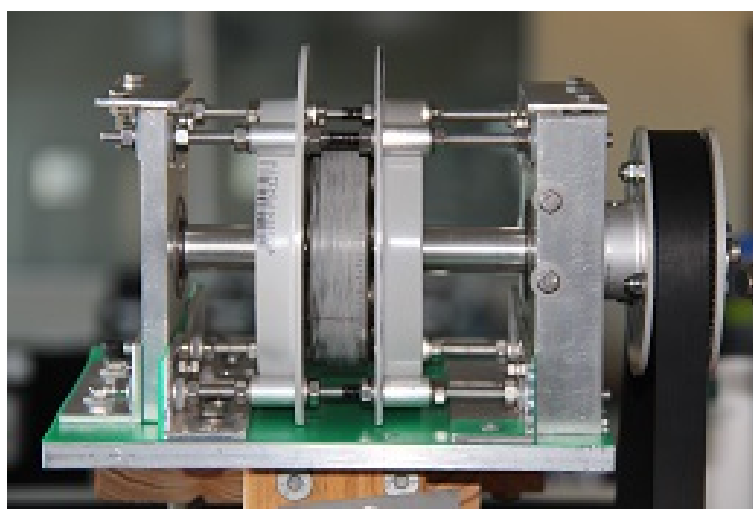


Figure 5.1: Assembled AFPM generator with blank stators. Blank stators have exactly the same dimensions and finish as stators with coils.

The blank stator generator is used for determining mechanical losses. The load cell

voltage is proportional to the weight of the generator itself, tension of the drive belt and the generator shaft resistance torque. In case of blank generator the only resistance torque produced is due *mechanical losses*: bearing, windage and rotor mass. Subtracting the measured load cell value proportional to the generator weight W and the belt tension T the mechanical losses can be estimated for various RPM.

$$\text{Mechanical Losses} = \text{Total Loss} - W - T \quad (5.1)$$

In terms of Load Cell voltage:

$$\Delta V = V_{\text{Mechanical Losses}} = V_{\text{Total Loss}} - V_W - V_T \quad (5.2)$$

The ΔV and estimated *Shaft Torque* (proportional to mechanical losses) versus RPM are shown in Figure 5.2.

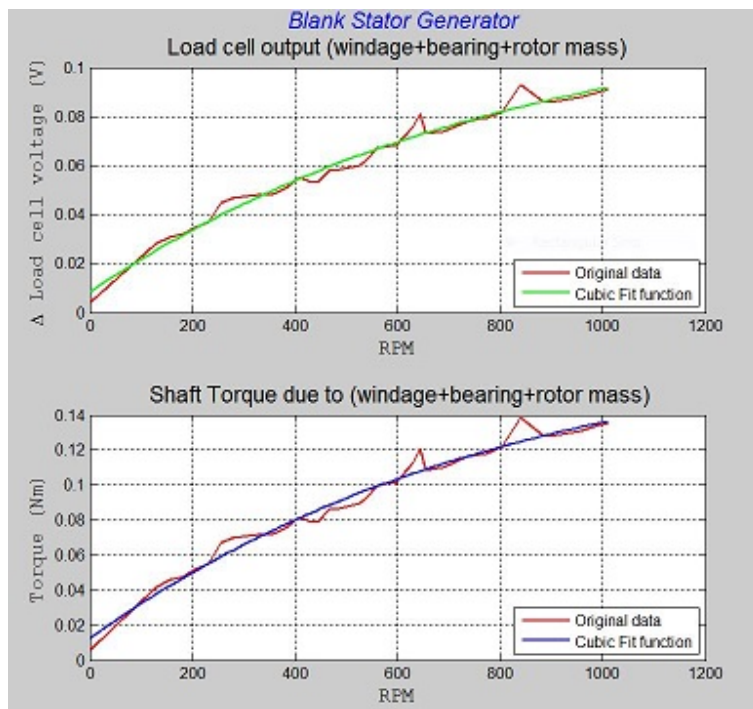


Figure 5.2: ΔV Load Cell and *Shaft Torque* proportional to mechanical losses. The actual measured data is shown in red. The Cubic Fit Function is used as the mechanical losses data for further analysis as it averages out irregularities in measurements and two pronounced peaks around 600RPM and 800RPM which are caused by vibrations at those frequencies.

5.2 Stator 1 Generator

The assembled AFPM generator with the 1st stator is shown in Figure 5.3.

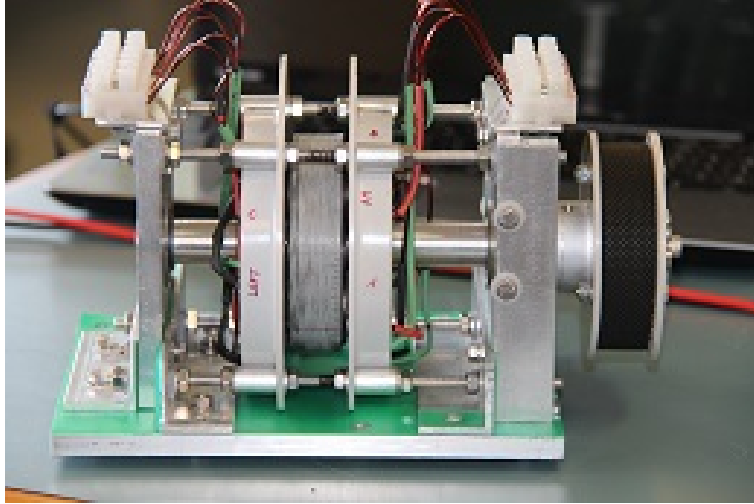


Figure 5.3: Assembled AFPM generator with the 1st stator. The ends of individual phases A , B and C on each half of the stator are taken out axially and supported inside the terminal blocks on the end plates of the generator.

The *no load* output from the 1st Stator Generator produced on the screen of a digital oscilloscope is shown in Figure 5.4. The 3 phase output and the voltage at the output of 3 phase rectifier (shown in green color) are obtained at 750RPM or at 50Hz. The corresponding 3-phase waveforms are shown in Figure 5.5. In addition to captured waveforms for A , B , and C phases, there are mathematically constructed waveforms. It is clear that the actual output is very close to the pure sinusoid.

Compared to the theoretical $EMF \hat{E} \approx 3.32V$ (Equation 4.27) the measured output is lower $\approx 2.96V_{pk}$.

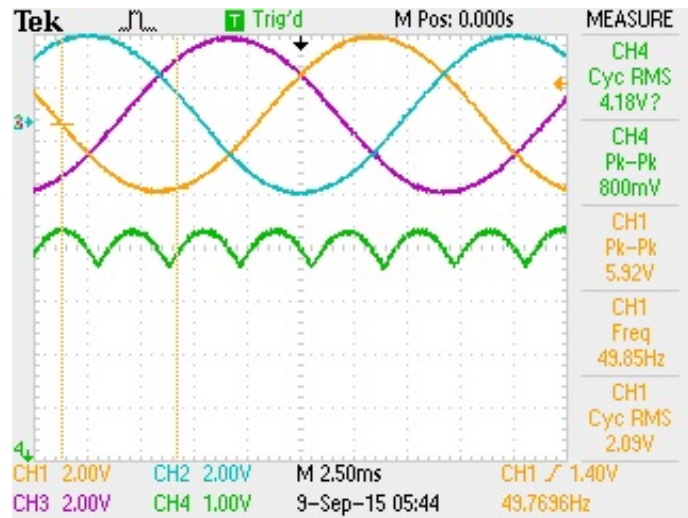


Figure 5.4: The no load output from the 1st Stator Generator produced on the screen of a digital oscilloscope. The 3 phase output and the voltage at the output of 3 phase rectifier (shown in green color - Channel 4) are obtained at 750RPM or at 50Hz.

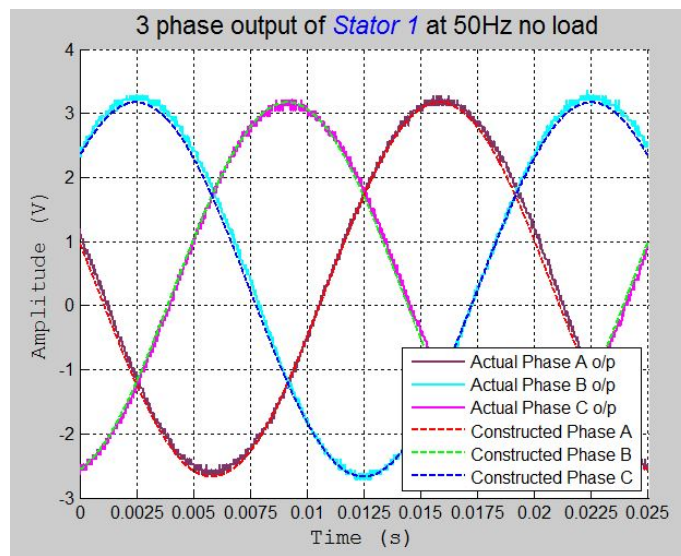


Figure 5.5: A, B and C phases waveforms of the Stator 1 generator (no-load, 50Hz).

The EMF, V-I for variable loads and Power for constant load are shown in Figures 5.6, 5.7, and 5.8 respectively.

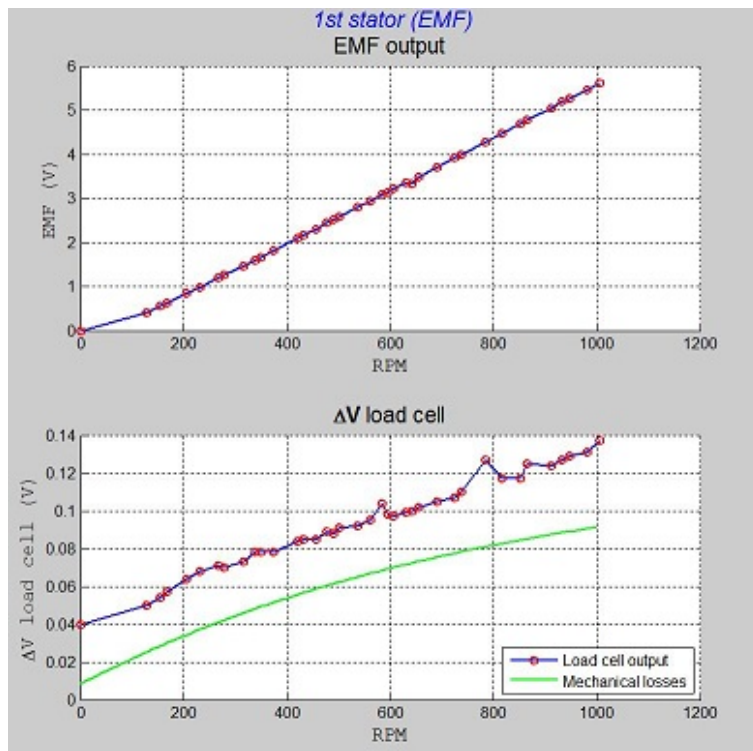


Figure 5.6: The no load output from 3-phase rectifier.

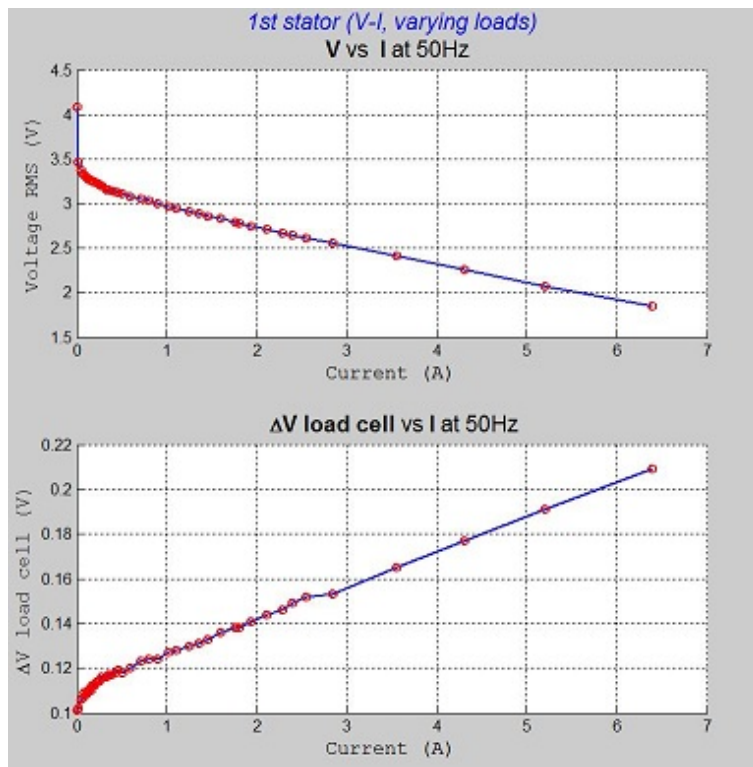


Figure 5.7: Voltage versus Current (V-I) at varying loads.

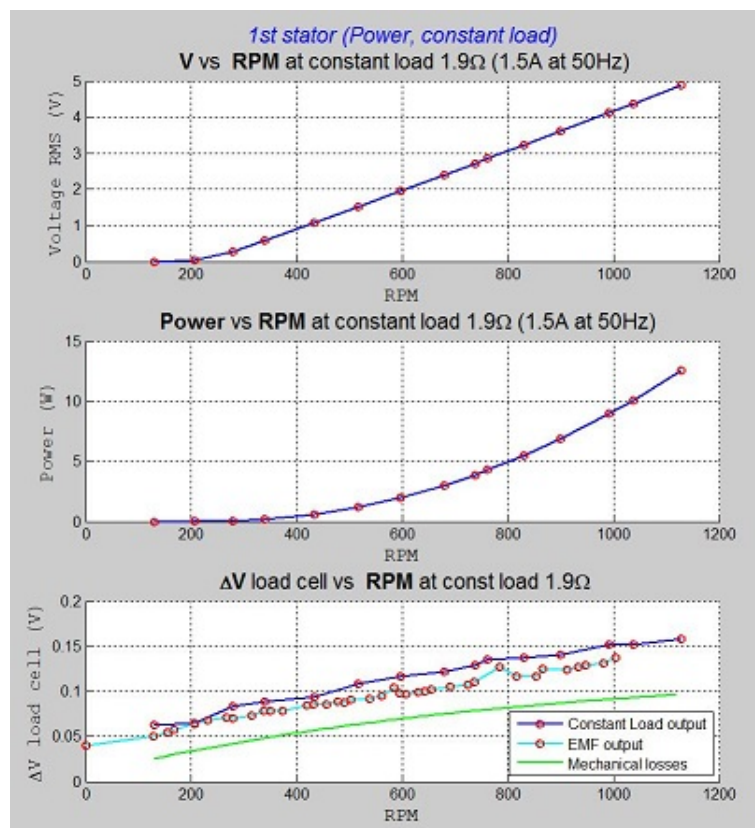


Figure 5.8: Voltage and Power output from 3-phase rectifier at constant load.

5.3 Composite Stator 2 Generator

The 2nd stator AFPM generator on the test bed is shown in Figure 5.9.

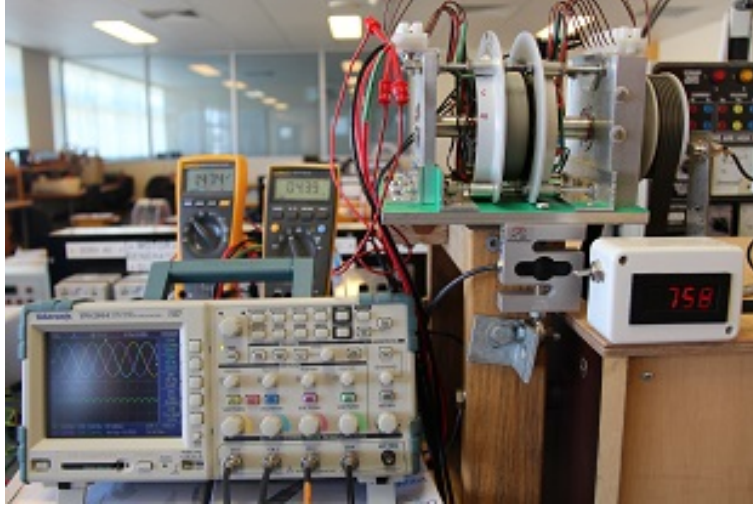


Figure 5.9: 2nd stator (composite) AFPM generator on the test bed.

The *no load* output from the 2nd Stator Generator produced on the screen of a digital oscilloscope is shown in Figure 5.10. Compared to the theoretical $EMF \hat{E} \approx 3.32V$ (Equation 4.27) the measured output is lower $\approx 3.16V_{pk}$.

The 3 phase output and the voltage at the output of 3 phase rectifier (shown in green color) are obtained at 750RPM or at 50Hz. The corresponding 3-phase waveforms are shown in Figure 5.11. In addition to captured waveforms for *A*, *B*, and *C* phases, there are mathematically constructed waveforms. It is clear that the actual output is very close to the pure sinusoid. The result is very similar to the *Stator 1*.

Measured parameters of Phase *A* are shown in Table 5.1. The measurements were carried out with an LCR Meter (Appendix C.4, item 13). The parameters of phases *B* and *C* are approximately the same, with slight variations again due to manufacturing tolerances. The coils of the same phase of two stator sides are connected with 200mm of rectangular copper wire (same as coil wire). The DC resistance of the 200mm wire is measured at $R_{connect} \approx 5m\Omega$. This resistance is included in the parameter measurements for *Phase A* ~ 4 coils in series. The *Max* value of series inductance (L_s) is achieved by positioning a rotor poles in the middle of stator coils.

Table 5.1: Stator winding parameters

Phase A (both stator sides ~ 4 coils in series)			
Frequency	Max/Min value of Ls	Series Inductance (Ls)	Series Resitance (Rs)
100 Hz	max	0.0420mH	77mΩ
100 Hz	min	0.0349mH	79.3mΩ
120 Hz	max	0.0416mH	77.7mΩ
1 kHz	max	41.33μH	83.9mΩ
Phase A (one side only ~ 2 coils in series)			
100 Hz	max	0.02mH	39.0mΩ
120 Hz	max	0.02mH	39.0mΩ
1 kHz	max	19.92μH	41.9mΩ

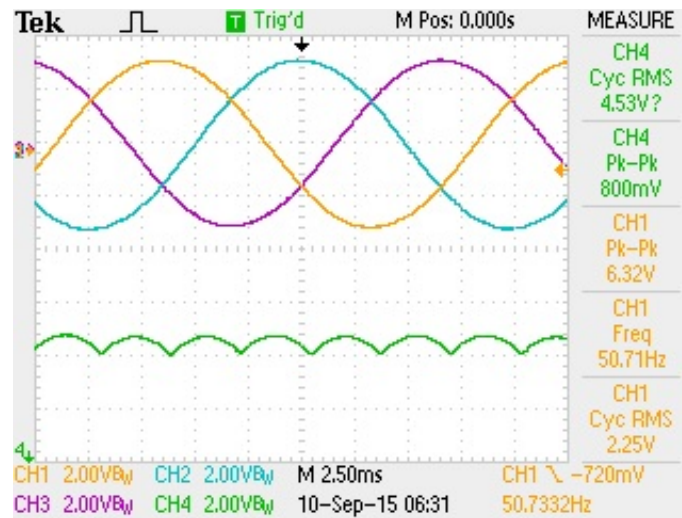


Figure 5.10: The no load output from the 2nd Stator Generator produced on the screen of a digital oscilloscope. The 3 phase output and the voltage at the output of 3 phase rectifier (shown in green color - Channel 4) are obtained at 750RPM or at 50Hz. The output here is higher compared to 1st Stator in Figure 5.4

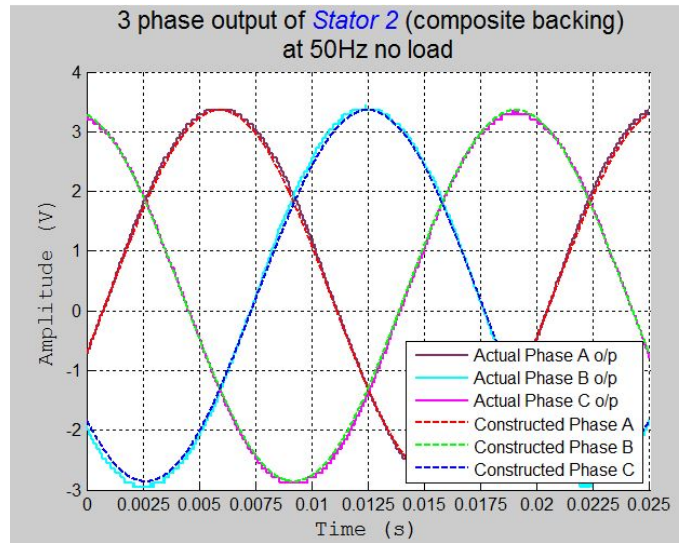


Figure 5.11: A, B and C phases waveforms of the Stator 2 generator (no-load, 50Hz).

The EMF, V-I for variable loads, Power for constant load and Stator Temperature for variable loads are shown in Figures 5.12, 5.13, 5.14, and 5.15 respectively.

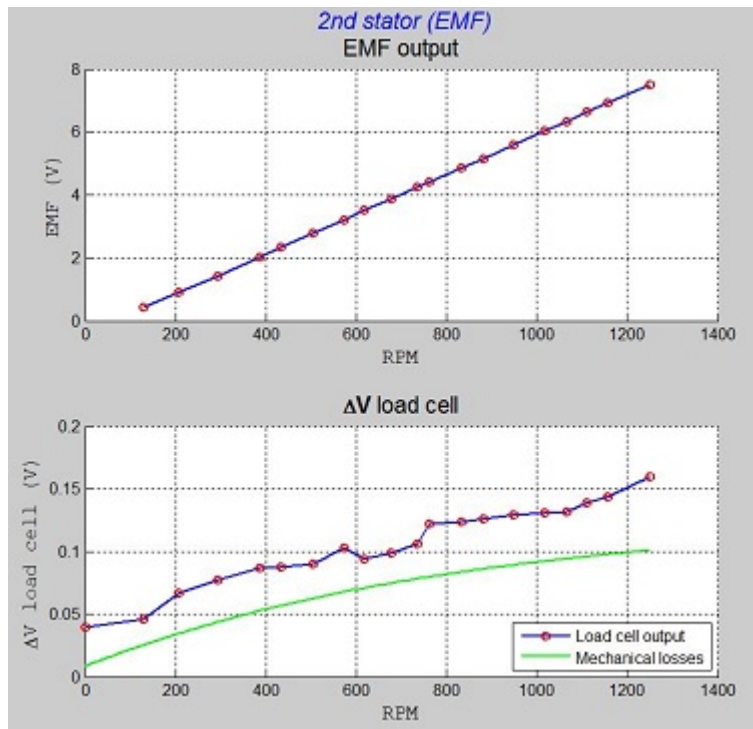


Figure 5.12: The no load output from 3-phase rectifier.

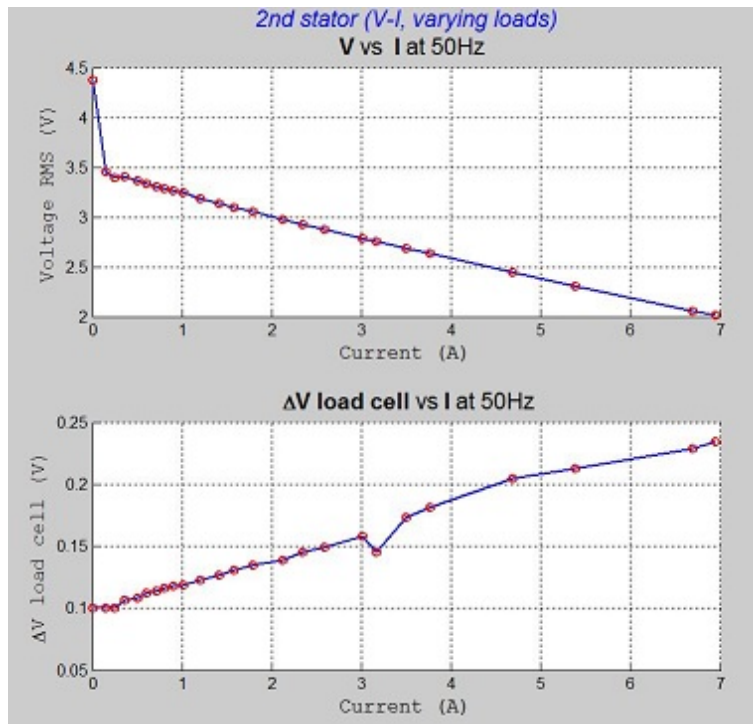


Figure 5.13: Voltage versus Current (V-I) at varying loads.

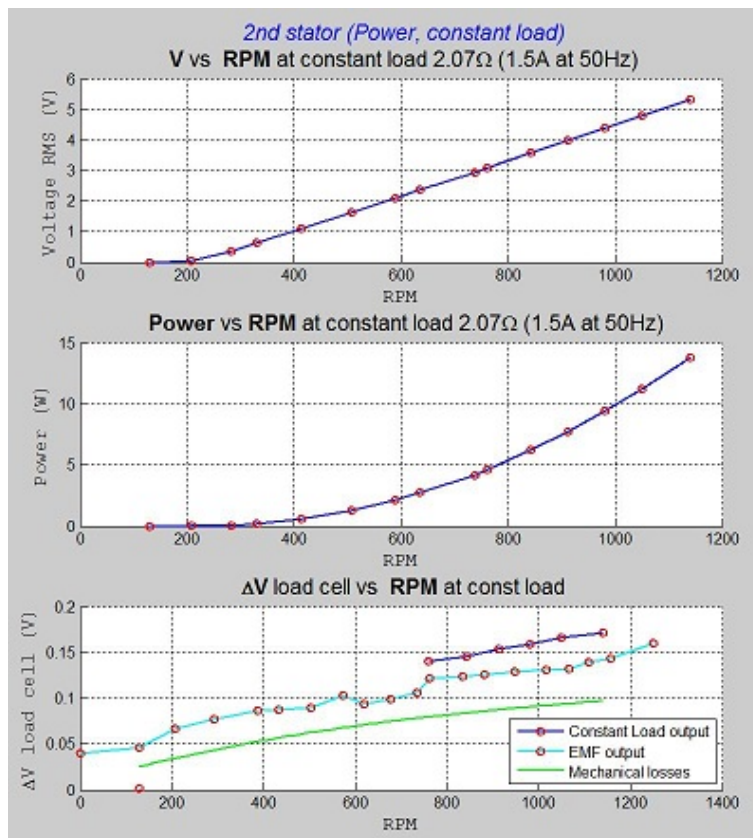


Figure 5.14: Voltage and Power output from 3-phase rectifier at constant load.

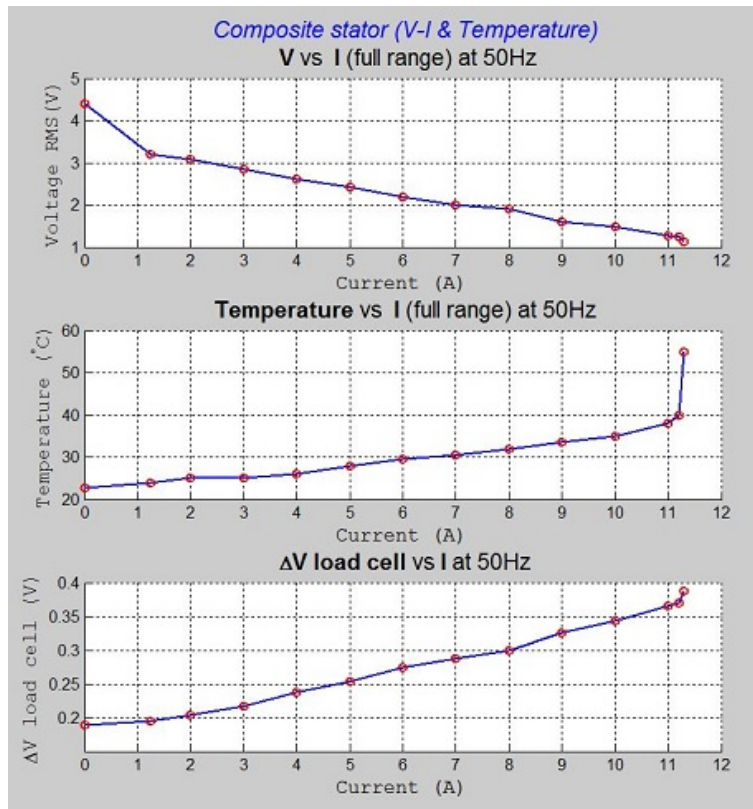


Figure 5.15: V-I and Stator Temperature for varying loads.

Stator temperature output taken with IR camera is shown in Figure 5.16. The corresponding camera view is given in Figure 5.17. The short was taken after running the generator for 20 minutes at 11A output current. The hottest part of the stator are the stator windings reaching 55°C . The rotor temperature at the time reached 40°C and this shown in Figure 5.18. The bearings's temperature was maintained at around 31°C .



Figure 5.16: Stator temperature output after 20 minutes at 11A output current.

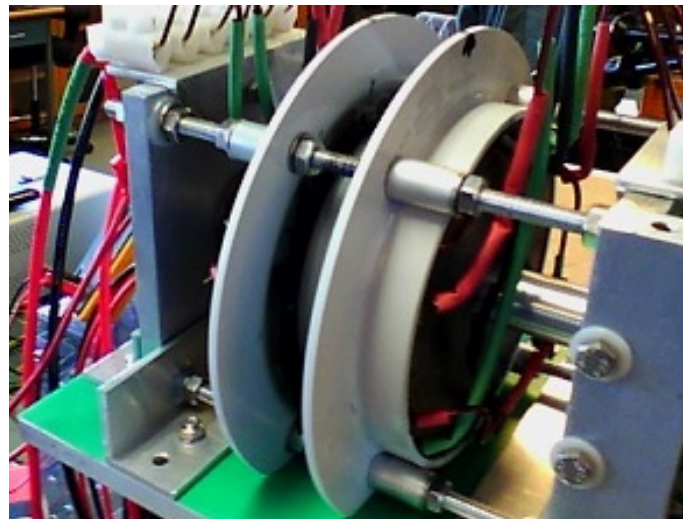


Figure 5.17: Plain camera view corresponding to the IR image in Figure 5.16.

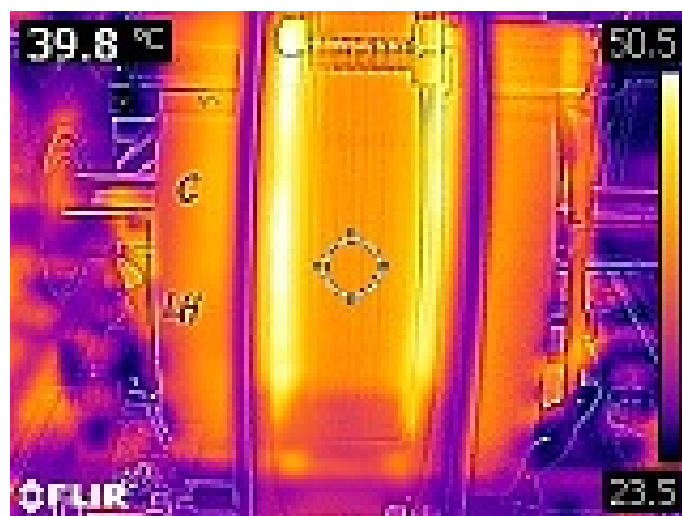


Figure 5.18: Additional IR image (after 20 minutes at 11A output current) showing the temperature of the rotor reaching about 40°C.

5.4 Stators' Performance and Comparison

The common characteristics of the constructed generator are shown in Table 5.2.

Table 5.2: Generator Characteristics

Parameter	Value
Number of Rotors	1 Internal Rotor
Inner Diameter of PM mounting (D_{in})	43mm
Outer Diameter of PM mounting (D_{out})	87mm
The average diameter (D_{av})	65mm
The inner to outer diameter ratio (k_d)	0.494
Number of Poles (P)	8
Number of pole pairs (p)	4
Pole pitch (τ_p)	45° (25.53mm)
Magnet width (pole width, magnet diameter) (w_m)	22mm
Magnet axial thickness (h_m)	25.4mm
Magnet width to pole pitch ratio (α_i)	0.86
Number of Stators	2 External Stators
Angular offset between stator sides	30° mech
Number of phases	3
Type of coils	Trapezoidal
Total Number of coils	12
Number of coils per stator side	6
Total Number of coils per phase	4
Coil span angle (θ_c)	60°
Number of turns per coil (N_c)	16
Number of turns per phase (N_s)	64
Type of wire	Ribbon
Wire external dimensions ($H_{ribbon} \times W_{ribbon}$)	1.07mm x 2.16mm
Active cross section area of ribbon wire (A_{active})	2.04 mm ²
Coil Axial thickness (nominal)	4.5mm
Physical air gap (g)	max 0.5mm
Average magnetic flux density in the air gap (B_{avg})	0.312T

Compared to the theoretical $EMF \hat{E} \approx 3.32V$ (Equation 4.27) the measured output for both generators is lower, which can be attributed to:

- Changing magnetic flux distribution in axial direction (Figure 4.5): the maximum magnetic flux density is $B_{mg} = 0.495T$ at $1mm$ and $B_{mg} = 0.290T$ at $5mm$. Therefore, the air gap **peak Magnetic Flux Density** will not be $0.49T$ for the whole thickness of a coil. The value of $0.49T$ was taken for the theoretical calculations.
- Magnetic flux distribution will change with the introduction of stators' backing discs. The output of the composite stator ($\approx 3.16V_{pk}$) is closer to the theoretical value, which means that **peak Magnetic Flux Density** approaches the value $0.49T$ for larger portion of stator coil axial thickness.

Two stators comparison in Power versus RPM at constant load (1.5A at 50Hz), V-I characteristic and ΔV at 50Hz (750RPM) for varying loads is shown in Figure 5.20. The backing of the composite stator was designed to counter the unfavourable distribution of the measured magnetic flux around the rotor. The composite stator performed better at the expense of higher gradient of the electromagnetic torque (Load Cell δV), which is to be expected.

Separate graph in Figure 5.21 depicts Power versus Current at constant RPM and varying loads. There is about a 23% improvement for the Composite Stator in peak output power reference to the 1st Stator.

The harmonic content (first 25 harmonics) for both stators at no-load and 50Hz is given in Figure 5.19. Both types of Total Harmonic Distortions (THD-F and THD-R) are higher for the composite stator (Table tab:hRMS. Regardless, the output for both stators is very close to pure sinusoidal waveform. Improving machine's rotor and stator manufacturing tolerances and symmetry will further clean the output.

Table 5.3: Total Harmonic Distortions

	THD-F	THD-R
Stator 1	1.82%	1.82%
Stator 2 (Composite Stator)	2.46%	2.44%

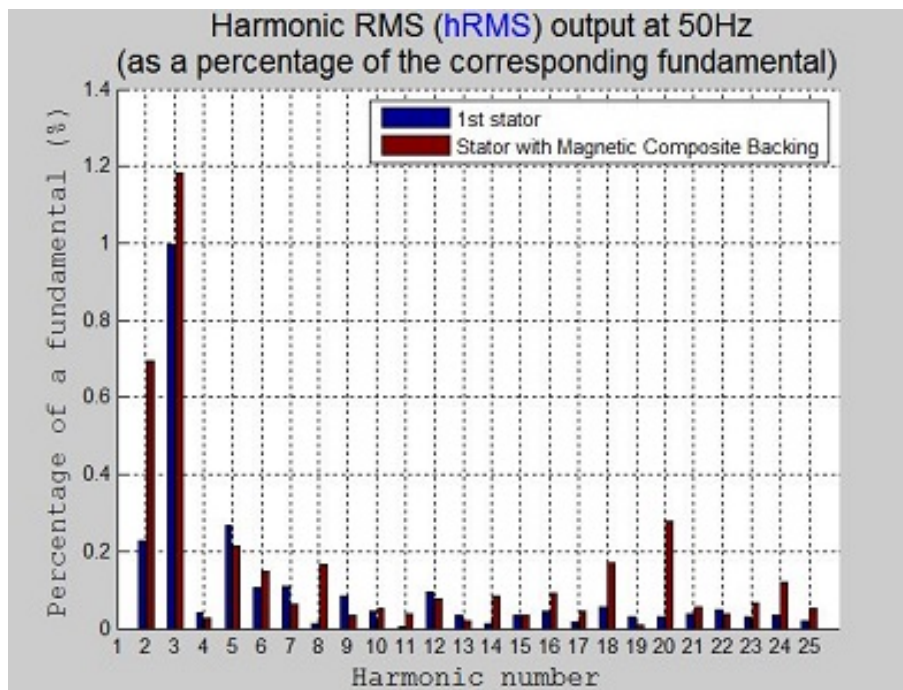


Figure 5.19: Stators 1 and 2 Harmonic RMS no-load output at 50Hz.

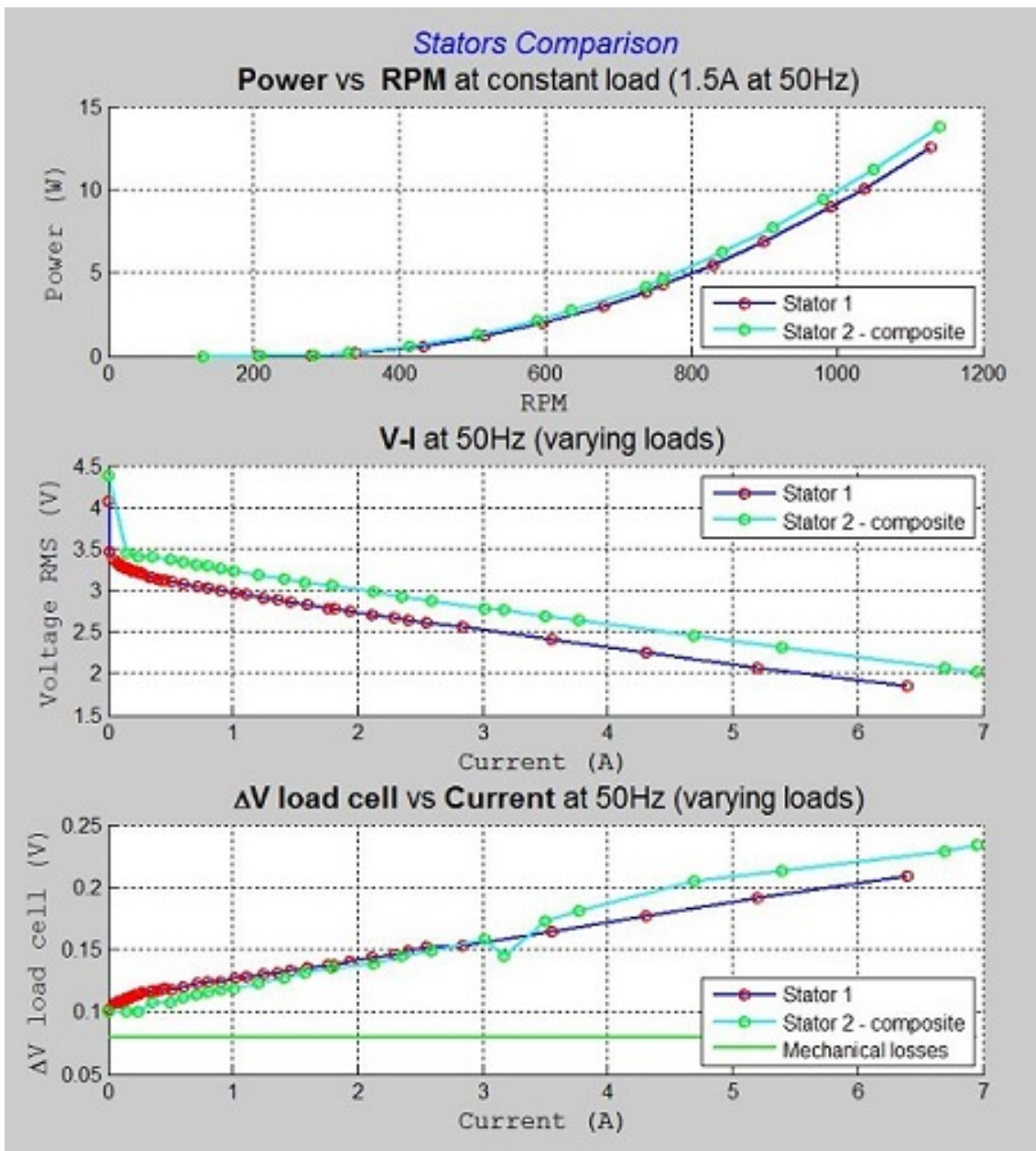


Figure 5.20: Stators 1 and 2 comparison in Power, V-I and load cell ΔV .

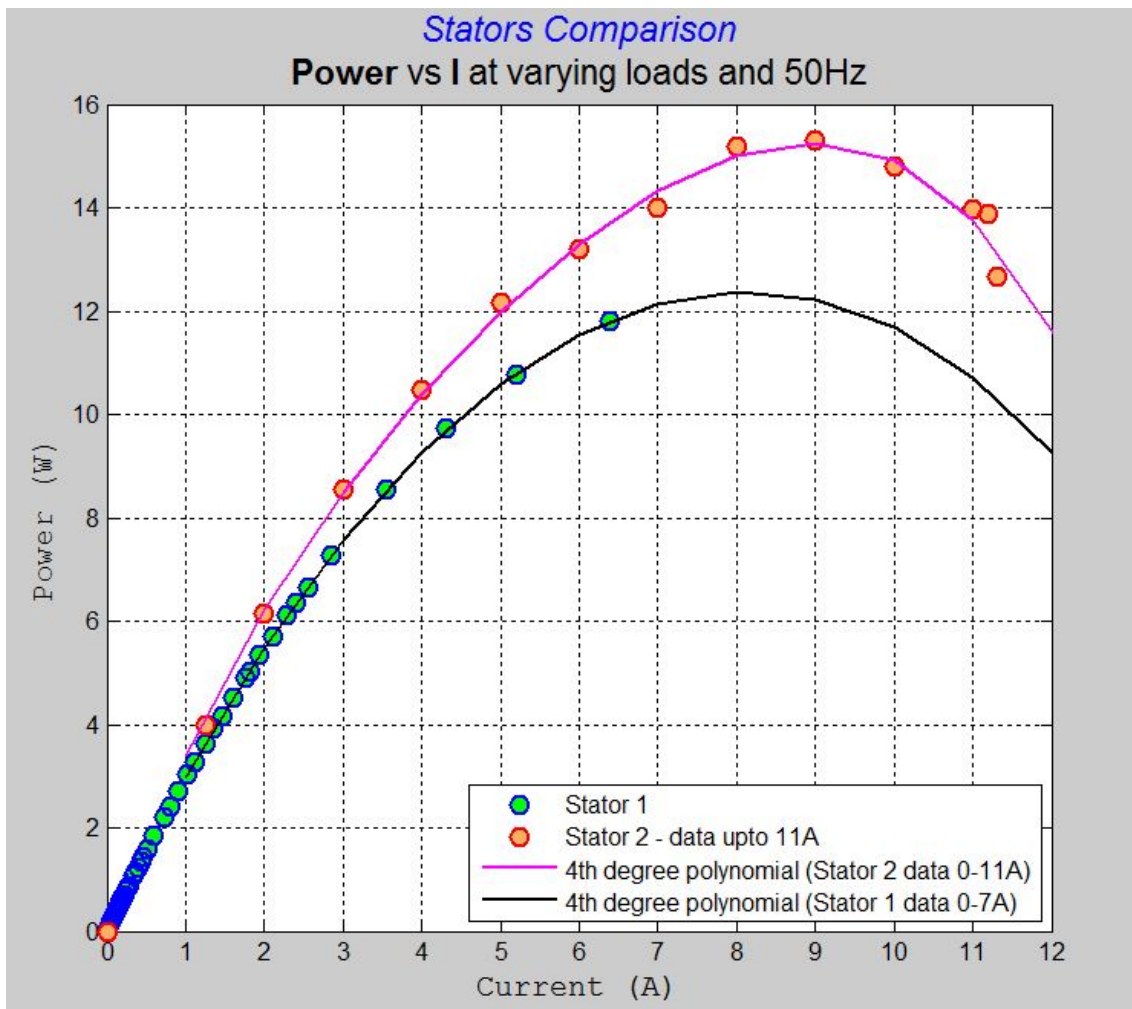


Figure 5.21: Stators 1 and 2 comparison in Power vs Current at constant RPM and varying loads. There is about a 23% improvement for the Composite Stator in peak output power reference to the 1st Stator.

Chapter 6

Conclusion

This chapter provides the summary of the research project. It addresses main lessons learned and it also outlines possibilities of any future work.

6.1 Summary points

The results of the research project can be summarised as follows:

- Confirmed no cogging torque in the built generator. This makes it ideal for low cut-in wind speeds requirements of low power wind generation units.
- Confirmed low inductance of stator windings.
- Confirmed the weaknesses of the Single-rotor/Double-stator configuration. Use of *coreless structure* requires careful magnetic flux path analysis in order to maximise efficiency.
- Confirmed the use of magnetic composite stator construction improves machine performance without an increase in cogging torque.
- Confirmed that circular polar shape with trapezoidal coils produces sinusoidal output.
- Besides the improved packing factor, there are added benefits for the use of ribbon wire which makes it suitable for this type of generator. It makes it easier to construct coils of the needed dimensions: flat thin rigid coils with minimum axial depth. Additionally, it simplifies coils reconnection for very thin stators (especially

in multi-disc configuration) as individual ends are readily available on the outer circumference of the machine without increasing the air-gap between discs.

- The number of poles need to be increased for the actual machine to obtain a low RPM performance suitable for wind generation. 16 poles would put the machine into the desirable RPM range (up to 400RPM). At the same time larger outer diameter is needed for maximum output power.

Several general improvements could be made to the current project:

- Replace aluminium rods with stainless steel ones for greater strength.
- More sensitive load sensor with a narrower span is needed to improve accuracy of torque measurements. An alternative is to use a torque sensor.
- Increase magnets (poles) placing circle diameter. This should lower the magnet width to pole pitch ratio α_i to the recommended range (0.4-0.7). As machine's outer diameter is increased this should lead to an increase in the machine's output power.
- The number of turns in a coil can be increased. Both radial and axial dimensions can be exploited. With an increase in the machine's outer diameter (radial dimension) the number of turns will be increased in a single layer. Axial magnetic flux distribution can be better utilised by increasing the axial thickness of stator coils at the expense of poorer copper winding utilisation.

6.2 Future Work

Given the obtained during the research project results, there are several items that can be included for future work. Some of them are:

- Building the two additional outside rotor discs should significantly improve the magnetic flux distribution. The rotor discs could include thin magnets with magnetic composite backing. This would allow for higher magnetic flux cutting through the stator coils which will maximise the output.
- A magnetic composite core stator could potentially significantly improve the generator performance. The effect of the composite core on the cogging torque could be

investigated.

- Performance of the machine as a motor can be investigated.
- Accurate Model of the machine could also be developed.

References

- Ani, S. O., Polinder, H. & Ferreira, J. A. (2012), Low Cost Axial Flux PM Generator for Small Wind Turbines, *in* 'Energy Conversion Congress and Exposition (ECCE)', IEEE, pp. 2350–3257.
- ARNOLD Magnetics Technologies (2015), 'Neodymium-Iron-Boron Magnet Grades, Summary Product List', viewed 20 April 2015, <<http://www.arnoldmagnetics.com/uploadedFiles/Library/pdf/Neo%20-%20Combined%20-%20140112.pdf>>.
- Aydin, Huang, M. S. & Lipo, T. A. (2004), Axial Flux Permanent Magnet Disc Machines: A Review, Research report, University of Wisconsin-Madison, College of Engineering, Wisconsin Power Electronics Research Center, vied 4 April 2014, <http://www.researchgate.net/profile/TA_Lipo/publication/228449891_Axial_flux_permanent_magnet_disc_machines_A_review/links/0fcfd5101846ea4ce100000.pdf>.
- Bumby, J. R. & Martin, R. (2005), Axial-flux permanent-magnet air-cored generator for small-scale wind turbines, *in* 'IEE Proc.-Electr. Power Appl.', Vol. 152, IEE.
- Dura Magnetics, Inc (2015), 'Stock Neodymium Magnets', viewed 20 April 2015, <<http://www.duramag.com/neodymium-magnets-ndfeb/stock-neodymium-magnets/>>.
- Fei, W., Luk, P. C. K. & Jinupun, K. (2010), 'Design and analysis of high-speed coreless axial flux permanent magnet generator with circular magnets and coils', *IET Electric Power Applications* 4(9), 739–747.
- Gieras, J. F. (2010), *Permanent magnet motor technology: design and applications*, 3rd edn, CRC Press, Taylor and Francis Group.
- Gieras, J. F., Wang, R.-J. & Kamper, M. J. (2008), *Axial Flux Permanent Magnet Brushless Machines*, 2nd edn, Springer Science + Business Media.

- Gonzalez, D. A., Tapia, J. A. & Bettancourt, A. L. (2007), Design consideration to reduce cogging torque in axial flux permanent-magnet machines, *in* 'IEEE TRANSACTIONS ON MAGNETICS', Vol. 43, IEEE, pp. 3435–3440.
- Hsieh, M.-F., Dorrell, D. G., Yeh, Y.-H. & Ekram, S. (2009), Cogging torque reduction in axial flux machines for small wind turbines, IEEE.
- Javadi, S. & Mirsalim, M. (2010), 'Design and analysis of 42-v coreless axial-flux permanent-magnet generators for automotive applications', *IEEE TRANSACTIONS ON MAGNETICS* **46**(4), 1015–1023.
- Latoufis, K. C., Messinis, G. M., Kotsampopoulos, P. C. & Hatziargyriou, N. D. (2012), 'Axial flux permanent magnet generator design for low cost manufacturing of small wind turbines', *Wind Engineering* **36**(4), 411–442.
- Lorilla, L. M., Keim, T. A., Lang, J. H. & Perreault, D. J. (2006), Foil Field Lundell Alternator with Rotating Power Electronics, *in* '37th IEEE Power Electronics Specialists Conference', IEEE Power Electronics Specialists, pp. 2164–2169.
- Mahmoudi, A., Rahim, N. A. & Hew, W. P. (2011), 'Axial-flux permanent-magnet machine modeling, design, simulation and analysis', *Scientific Research and Essays* **6**(12), 2525–2549, <<http://www.academicjournals.org/SRE>>.
- MEDER electronics (2015), 'Magnets and their specifications', viewed 20 April 2015, <http://www.digikey.com.au/Web%20Export/Supplier%20Content/Meder_374/PDF/MEDER_Magnet_Specifications.pdf?redirected=1>.
- Melendez-Vega, P. & Venkataramanan, G. (2012), Aluminum foil coils for human scale wind turbines, *in* '2012 IEEE Global Humanitarian Technology Conference (GHTC)', IEEE, pp. 1–5.
- Nguyen, T. D. & Tseng, K. J. (2012), 'Loss study of a dual-air-gap axial flux permanent magnet machine', *Australian Journal of Electrical & Electronics Engineering* **9**(4).
- Page, J. (2015), 'Math Open Reference', viewed 15 Apr 2015, <<http://www.mathopenref.com/>>.
- Reference Data for Radio Engineers* (1975), Howard W. Sams & Co., Inc.
- TEMCo Tower Electric Motor Company (2015a), 'Temco copper magnet wire - data sheet, gp/mr-200 - 200c temp class, polyester/polyamideimide', viewed 1 April 2015, <http://temcocontent.com/attachments/gpmr200_data_sheet.pdf>.

TEMCo Tower Electric Motor Company (2015*b*), 'Temco copper magnet wire - dimensions & weights', viewed 1 April 2015, <http://temcocontent.com/attachments/magnet_wire_dimensions_weights.pdf>.

U-POLEMAG Industry Limited (2015), 'Coreless vertical wind generator', viewed 14 April 2015, <http://www.u-polemag.com/coreless-vertical-wind-generator_p107.html>.

WPS2000 Inc. (2015), 'Low rpm 5kw coreless wind generator (vawt)', viewed 14 April 2015, <<http://www.wps2000uv.com/index.php?mit=201&string=Technical%20Data>>.

Appendix A

Project Specification

University of Southern Queensland
Faculty of Health, Engineering & Sciences

ENG 4111/4112 Research Project
Project Specification

For: **Vladislav Kaliyev**
Topic: Axial Flux Permanent Magnet Ironless Core machine characteristics and applications
Supervisors: Andreas Helwig
Sponsorship: Faculty of Health, Engineering & Sciences
Project Aim: To experimentally investigate characteristics of Axial Flux PM Ironless machine allowing for determination of its possible practical applications.

Program:

1. Research the background information on Axial Flux Permanent Magnet (AFPM) machines and their applications (specifically for wind energy generation applications).
2. Critically examine the various constructions and topologies, advantages and weaknesses.
3. Compare construction materials and methods.
4. Design coreless and cored AFPM machine.
5. Construct the designed machine.
6. Analyse distribution of magnetic field in the the air gap.
7. Test the constructed machine as a generator.
8. Investigate possible applications.
9. Submit an academic dissertation on the research.

As time and resources permit:

1. Investigate the use of foil winding in the AFPM machines.
2. Test the constructed machine as a motor.
3. Investigate effectiveness of multi disc rotor configurations.
4. Investigate modelling of the machines' characteristics.

Agreed:

Student Name: Vladislav Kaliyev
Date: March 12, 2015
Supervisor Name: Andreas Helwig
Date: March 12, 2015

Appendix B

Project Risk Assessment

This appendix contains risk assessment of the research project.

B.1 Risk Assessment

Hazards

The two broad phases of the project are prototype manufacturing and testing of the prototype AFPM machine. The research project has risks associated with both phases. The identified hazards are as following.

Hazards during manufacturing:

- Moving parts of power tools: lathe, drill press, mitre saw, shop press.
- Hand tools: hacksaw blade, files, screw drivers.
- Hazardous substances: polyester epoxy, cleaning agents (acetone), adhesives (Araldite).
- Fibre materials: Chopped Strand Mat (CSM).
- Electrical power.

Polyester Resin used is Low Styrene Emission (waxed) catalysed with Methyl Ethyl Ketone Peroxide (MEKP). The common hazards may include:

- Skin irritation.
- Eyes irritation.
- Thermal processing of fibre may generate fumes and vapours which may cause irritation to the nose and throat.
- Flammable liquid.

Hazards during testing:

- Moving parts of the AFPM machine: AFPM rotor is belt driven and is rotating with reference to stationary stator and the rest of the AFPM supporting structure.
- Electrical shock: 24 V power supply, 240 V test bed drive, 240V test equipment.

Control measures

The risks associated with the prototype manufacturing are controlled by adhering to guidelines provided in the equipment manufacturers instructions and use of appropriate

to the work *personal protective equipment* (PPE). The *minimum required PPE* for all jobs is:

- Steel cap boots,
- Safety glasses,
- Hearing protection (class 5) and
- Properly fitted (non-loose) protective clothing.

The *workshop control measures* include:

- Use of standard non-modified equipment.
- Separation of work and safe areas.
- Provision of good lighting.
- Use of ventilation in the work areas (natural ventilation).
- Use of industry approved safe work methods.
- Storing hazardous substances in cool, dry, well ventilated place and in metal cabinets away from work areas. Keeping all substances out of reach of any personnel (children inclusive).
- Employment of safety switches for all power points.
- Ensuring electrical power cords are in good condition and are secured away from moving machinery.

The application of all chemicals is strictly in accordance with the manufacturers instructions. The practice is to conform to the appropriate MSDS. The recommended PPE for working with polyester resin is as follows:

- Safety goggles.
- Maxi Mask 2000 Half Mask Respirator (HMTPM) and ABEK1 cartridges.
- PVC gloves.
- Safety boots.

The additional measures during the *testing operations* include:

- Safety shut down switch for the test bed drive.
- Safety transparent screen isolating the prototype from personnel.
- Use of only standard test equipment where applicable.
- Minimum start speed for the prototype before accelerating to the required RPM.

- Minimum operating time.
- Enclosed shoes with insulating soles.
- Safety glasses.

Evaluation

Provided the use of standard tools, well known materials and well established methods and procedures the risk associated with the identified hazards is “not significant and *is not likely to increase*. The prototype is the only machine produced during this research project. The current control measures are adequate at the moment. However, additional training in the prototype operation might be needed for any new personnel involved in the future research.

Appendix C

Manufacture and Testing

This appendix contains the following information:

- C.1 – List of parts and materials used for AFPM prototype construction.
- C.2 – Rotor manufacturing steps.
- C.3 – Stator manufacturing steps.
- C.4 – List of test equipment.

C.1 Parts and materials used for AFPM prototype manufacturing

List of parts/materials used for AFPM construction:

- 1) NdFeB magnets x8. Dimension: $diameter_m = w_m = 22mm$ and $height = axial\ thickness = h_m = 25.4mm$. Grade is unknown.
- 2) Waxed Polyester Resin with Methyl Ethyl Ketone Peroxide (MEKP) hardener.
- 3) Fibreglass Chopped Strand Mat (CSM) 300gm.
- 4) Fibrecore 3mm Fibreglass.
- 5) Mirror Glaze Mold Release Wax.
- 6) *Araldite Selleys*[®] Epoxy Adhesive Super Strength.
- 7) Plywood Marine AA grade 9mm thickness.
- 8) Elbow *Rain Harvesting* 90mm M&F 90° Flanged (Flange is used only for the rotor).
- 9) DWV PVC Floor Flange Holman 100mm (Stator).
- 10) Aluminium plate 10mm thickness 2 of 120x100 (side supports), 1 of 160x210 6060T5 (base plate).
- 11) Aluminium round bar 6.3mm.
- 12) Aluminium round bar 10mm T3.
- 13) Aluminium round bar 22mm T3.
- 14) Aluminium round bar 39mm T5.
- 15) Aluminium round bar 25mm T5.
- 16) Aluminium Angle 30mm.
- 17) Bearings NTN 6203LLU/19.05C3/2AS (Qty 2).
- 18) Bolts SS M4, M5 and M6 various lengths (10mm, 20mm, 25mm, 30mm). Nuts hex/Nylock M4, M5 and M6.
- 19) Grab screws M4, M5 various lengths.

- 20) Blind Rivets Aluminium *Zenith* 5/32 Diam 1/2 Grip.
- 21) Hinge Butt FP *Zenith* 70mm SS. (Qty 2).
- 22) Heat-shrink tubing 8mm, 10mm.
- 23) Nylon Bushings 5mm internal, 8mm external (various lengths).
- 24) Nylon Washers M6.
- 25) Nylon Mat 0.6mm thickness.
- 26) Rare Earth Magnet 10x3 (speed sensor).
- 27) Iron Powder NC100.24 (composite backing).
- 28) Rust converter - SEPTONE[®] (phosphoric acid for iron powder treatment).
- 29) 30A Terminal Block (stator side connection).

C.2 Rotor manufacturing

The thickness of the rotor core is chosen to be $3mm$ less than the height (or axial thickness) of magnets ($h_m = 25.4mm$). The resultant magnets' protrusion of $h_{protrus} = 1.5mm$ beyond the core (on both sides) allows for creating a fillet of epoxy adhesive at the time of setting the magnets into the core. The idea is to have no epoxy material on the poles' surfaces of the magnets as to allow for minimum air gap between the rotor and the stator sides.



Figure C.1: Rotor setup parts from left to right: pre-cut Fibreglass Chopped Strand Mat (CSM) 300gm, pre-cut Fibrecore 3mm Fibreglass, press plate, Rotor Bushings, former flange. The CSM adds structural strength to the core, while the Fibrecore gives extra body to the core.

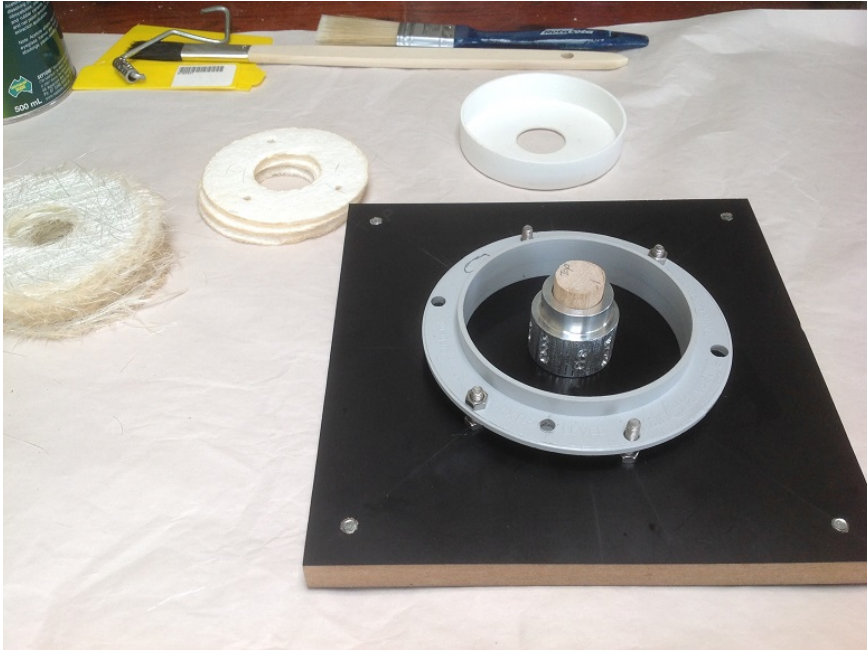


Figure C.2: Rotor supporting structure ready for polyester resin. The symmetrical cut-outs are visible on the surface of the Rotor Bushing. The concentricity of the Rotor Bushing and the *former* is maintained.



Figure C.3: Rotor former set with the polyester resin (Top side).



Figure C.4: Rotor former set with polyester resin (bottom side). CSM is clearly visible on the photograph.

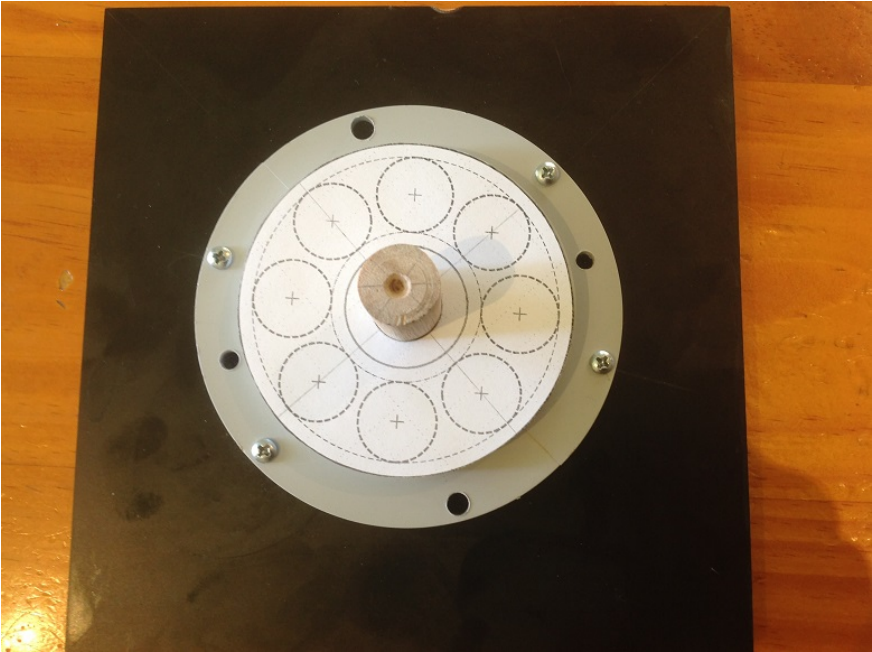


Figure C.5: Rotor magnets template is set – ready for drilling.



Figure C.6: Rotor magnets holes are partially drilled.



Figure C.7: Rotor magnets holes are being finalised to allow extra space for the adhesive.



Figure C.8: Rotor supporting structure is ready for magnets (bottom side).



Figure C.9: Rotor supporting structure is ready magnets (top side). There are imperfections in the surface finish. The magnets' placements are marked N, S to accommodate magnets' magnetic poles.



Figure C.10: Rotor magnets are set with *Araldite Selleys* Epoxy Adhesive. There is a fillet of *Araldite* between the surfaces of polyester resin (core) and the magnets to provide an extra bond. The magnets' pole surfaces are free of any epoxy.

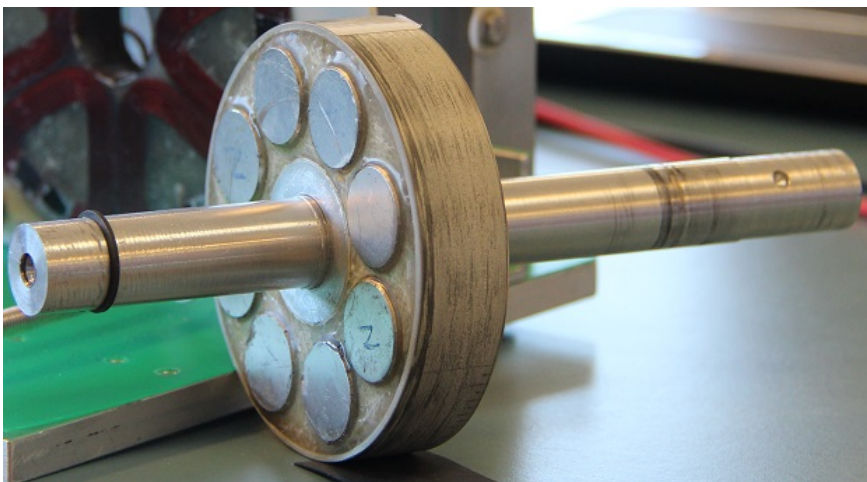


Figure C.11: The complete rotor assembly. The rotor is pressed on an aluminium shaft.

C.3 Stator manufacturing

The general procedure for a *single stator side manufacturing* involves the following steps:

- 1) Individual single layer coils with a calculated number of turns ($N = 8$) are wound on a coil former (Figures C.12 - C.15).
- 2) Two single layer coils are joined together to form a double layer coil. The two single layer coils are aligned so that the conductor winding direction of both layers is the same (i.e. the number of coils adds). After the layers are joined together with adhesive, the inner ends are soldered leaving the outer ends being available for external connection (Figures C.16 and C.17).
- 3) 6 double layer coils are placed in the stator mould (Figures C.18 and C.19).
- 4) The stator mould is filled with polyester resin reinforced with Fibreglass CSM and Fibrecore.
- 5) The *Stator 1* (without backing) is formed with a maximum possible number of layers of Fibreglass CSM and Fibrecore (Figure C.20).
- 6) The *Stator 2* (composite backing) is formed as follows (Figure C.21):
 - Polyester resin is applied up to the depth of the double layer coils.
 - Three layers of CSM are formed directly on top of coils. This serves dual purpose: to reinforce and also to separate coils from iron powder.
 - 5mm thickness of *magnetic non-conductive iron powder* mixed with polyester resin (50% concentration) is applied next. This is followed by two layers of CSM, and finally finished with another 5mm layer of magnetic composite mix. The *magnetic non-conductive iron powder* is produced by agitating fine Iron Powder (Appendix C.1) in phosphoric acid.
- 7) 6 individual coils of each side are joined into 3. Two coils belonging to the same phase are connected in series. The ends of final 3 coils of a stator side are terminated with 6 way terminal block for easy connection and disconnection. (Figures C.23 and C.24)

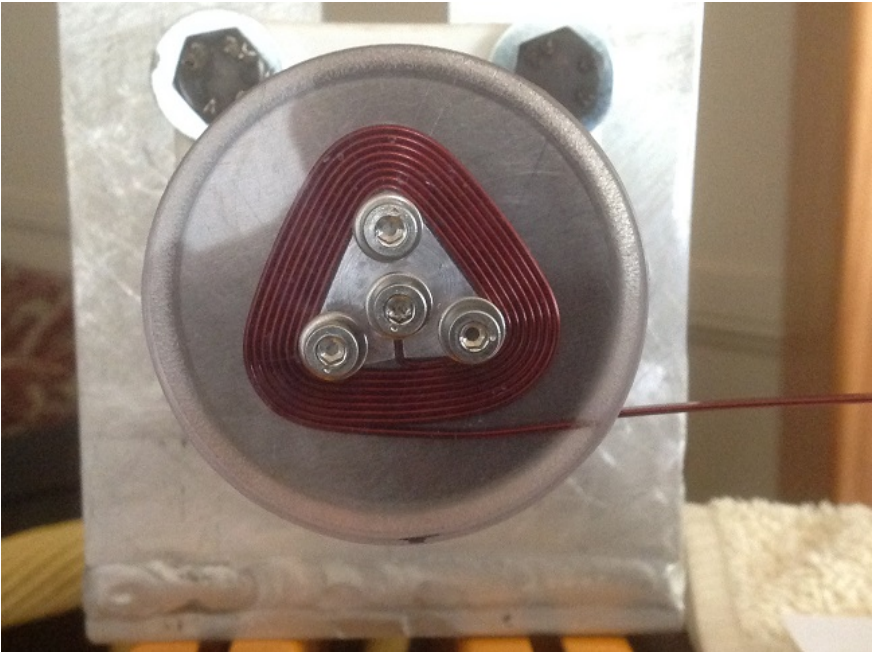


Figure C.12: A single layer coil is formed. There are 8 turns in the coil.

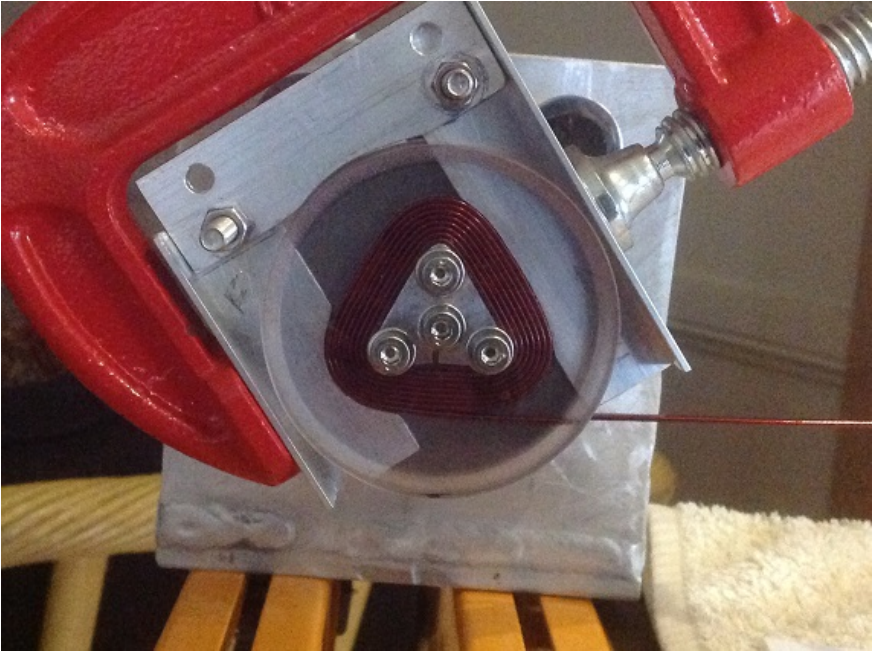


Figure C.13: A single layer coil is clamped while under tension before removing from the winding machine.

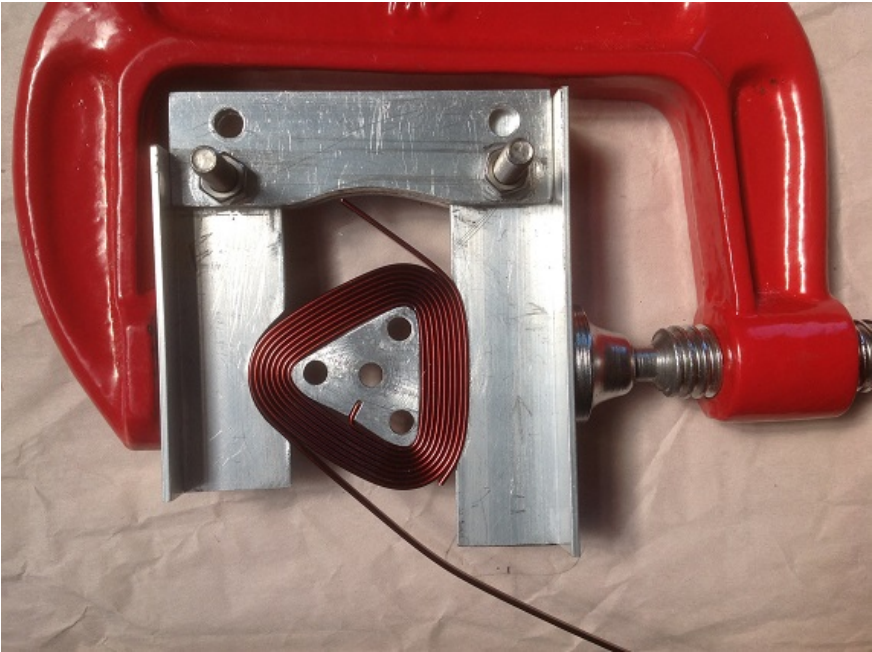


Figure C.14: A single layer coil is removed from the winding machine. Once the centre former is knocked out the coil can be zip-tied allowing for clamp removal.



Figure C.15: Araldite is applied to the sides of a single layer coil.



Figure C.16: Two single layer coils are correctly oriented for joining.

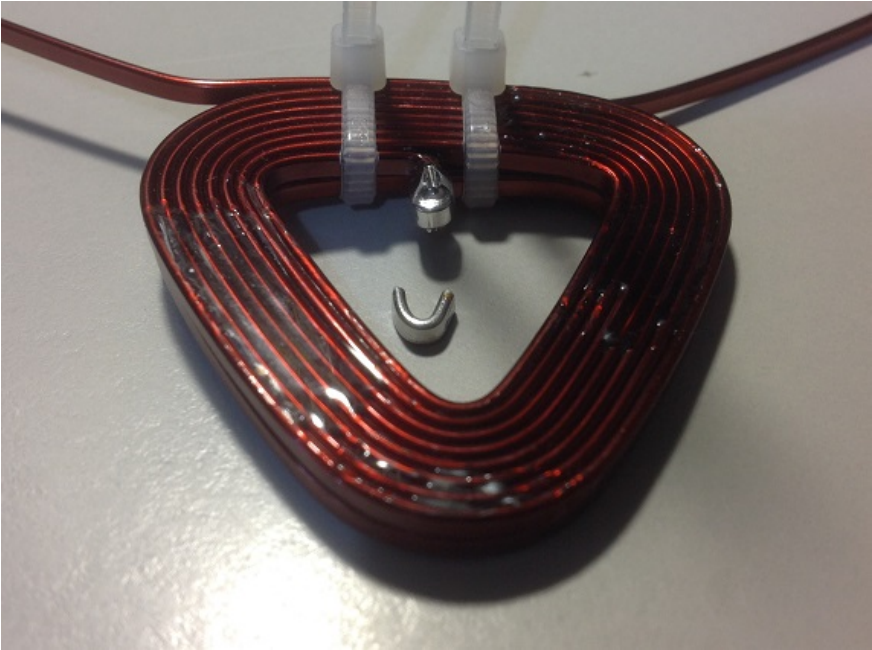


Figure C.17: A complete coil is formed by applying Araldite between the individual layers. The inner ends are soldered with an aid of tinned clamped.



Figure C.18: The stator mould.

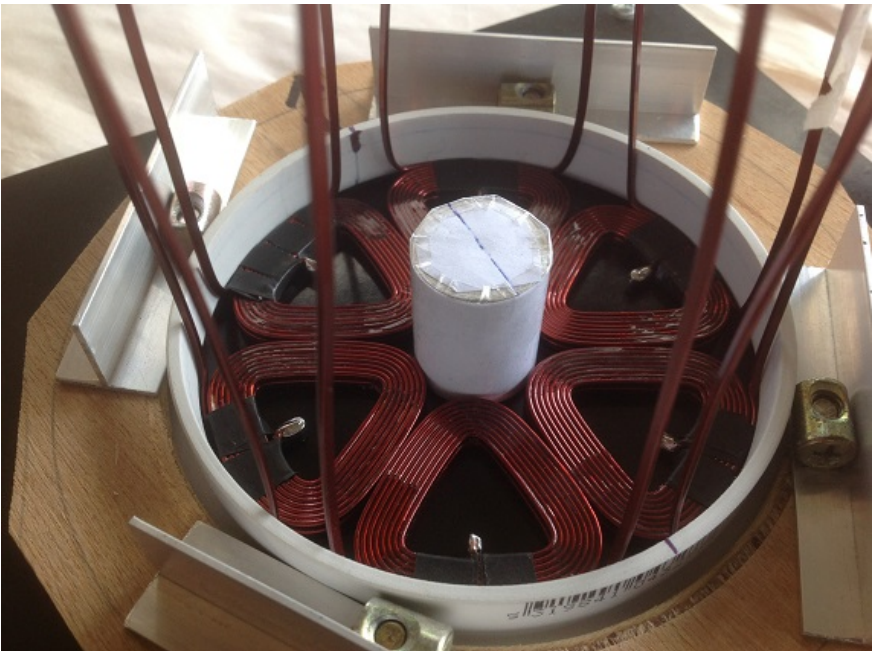


Figure C.19: 6 coils are positioned inside the stator mould.

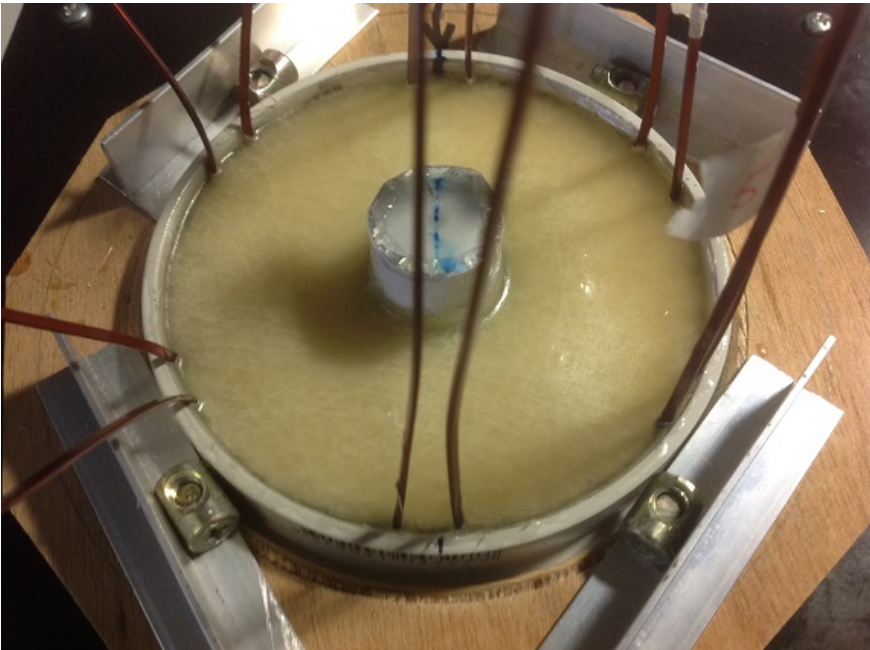


Figure C.20: A stator without magnetic backing.

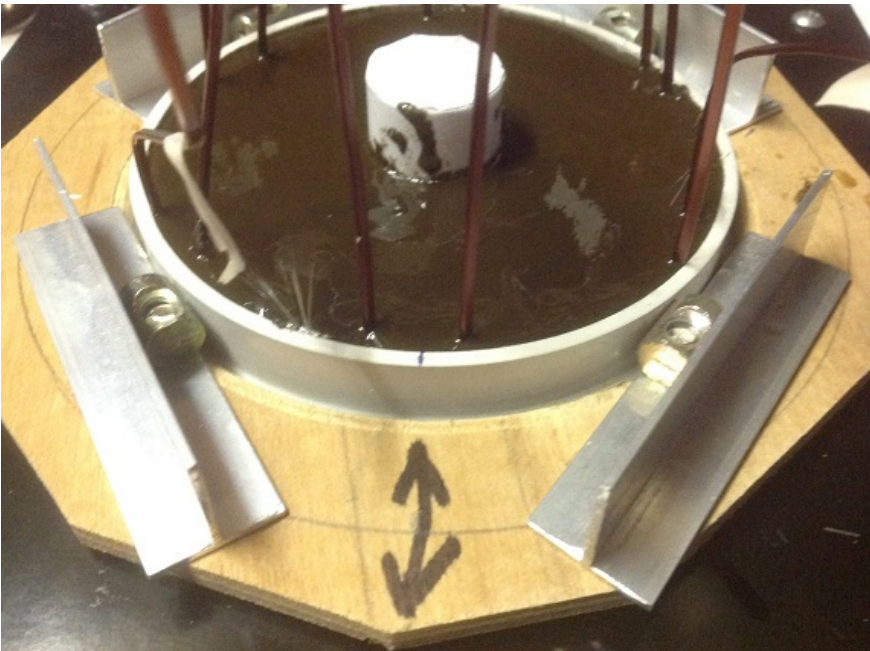


Figure C.21: A stator with composite magnetic backing.

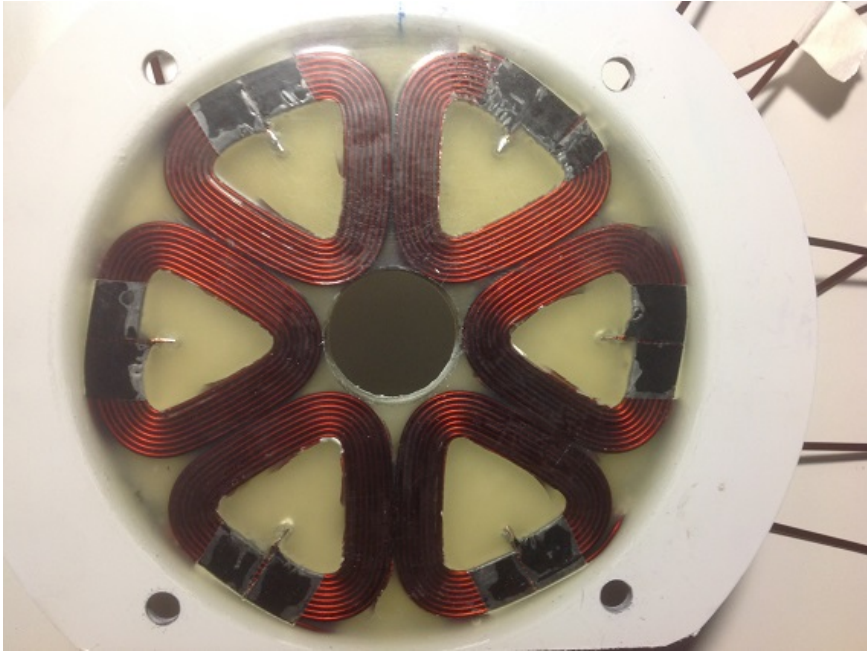


Figure C.22: A stator side complete. There are 6 coils per stator side.

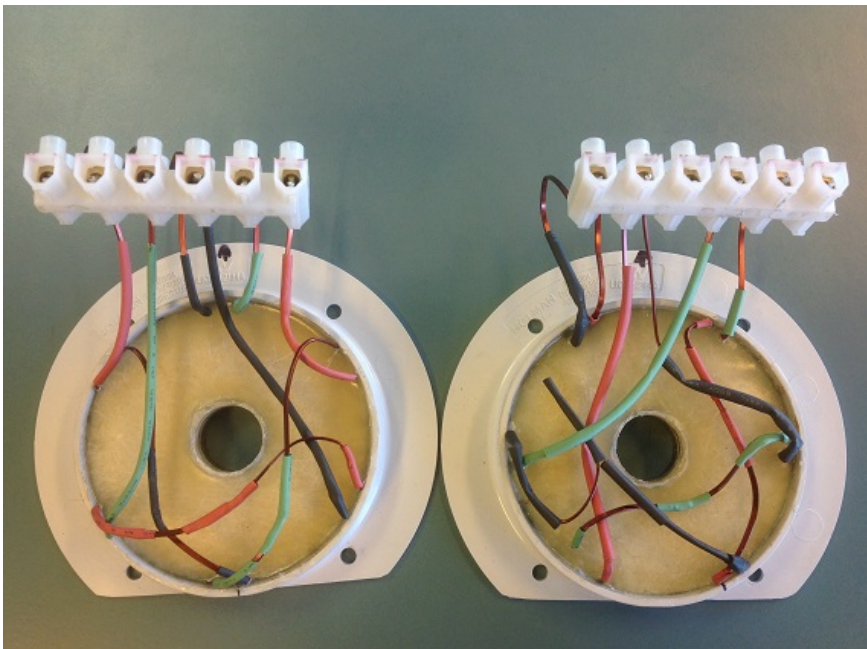


Figure C.23: Two stator sides without magnetic backing. 6 individual coils of each side are joined into 3. Two coils belonging to the same phase are connected in series. The ends of final 3 coils of a stator side are terminated with a 6 way terminal block for easy connection and disconnection.

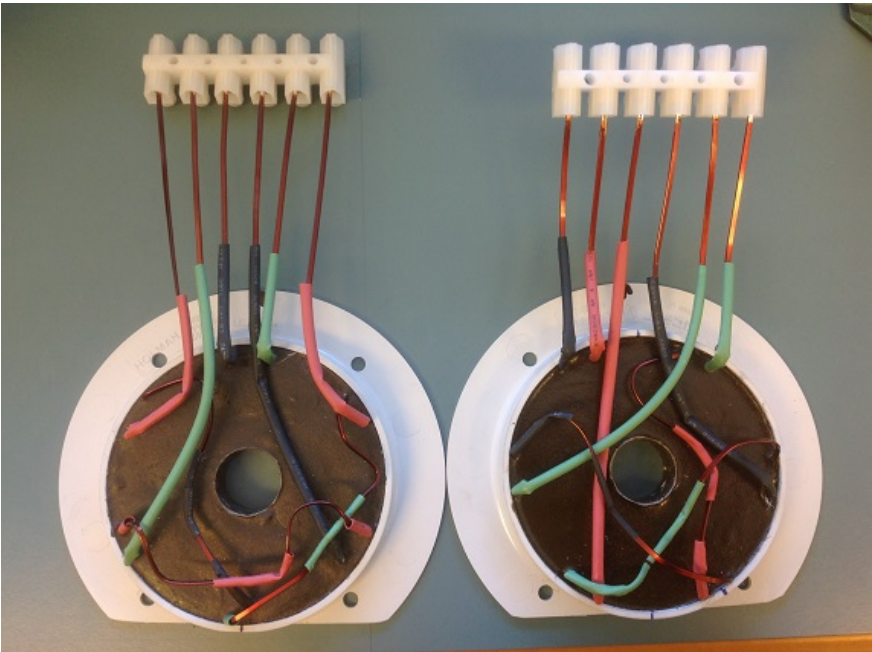


Figure C.24: Two stator sides with magnetic composite backing. The darker color of the iron powder (compared to Figure C.23) is clearly visible.

C.4 Test Equipment

Test equipment used during the research project:

- 1) DSP Gaussmeter (Model 455) by *LakeShore* with *Transverse* HMMT-6J04-VR rectangular probe. (Rotor Magnetic Field distribution).
- 2) USB Digital Microscope (20x-200x) with *MicroCapture* software Version 1.3M. (Ribbon Wire dimension).
- 3) 250kg AST S-Type tension/compression load cell by *PT Ltd* coupled with PT100LC load cell conditioner/transmitter. (AFPM Torque).
- 4) *Fluke 19* multimeter. (Voltage and Current).
- 5) Digital Photo Tachometer *DT – 2234C⁺*. (AFPM RPM)
- 6) Vernier Calipers 0.02mm resolution.
- 7) Tektronix TPS 2014 4 Channel, Digital storage oscilloscope, 100MHz, 1GS/s, with Compact Flash (CF type 1) and an Application Key. (Output Waveforms and Harmonic distortion)
- 8) FLIR C2 Infrared Camera. (Temperature Measurements)
- 9) Analog DC Ammeter - $\pm 30A$. (Load Current)
- 10) 10Ω , 10A Rheostat - Qty 2. (Load Resistance)
- 11) 2Ω , 22.4A Rheostat - Qty 1. (Load Resistance)
- 12) RBA-5kW250VDF-V1 switchable industrial resistor (250V - 1A, 2A, 5A and 10A). (Load Resistance)
- 13) Agilent 4263B LCR Meter. (Inductance and Resistance of stator windings)
- 14) GPC-1850 Dual Tracking Power Supply. (Load Cell 24V power)
- 15) SEMIKRON SKD 51/14 3-phase rectifier.

Appendix D

Program Source Code

D.1 The rotor_and_bushing.m MATLAB program

The program `rotor_and_bushing.m` sets dimensions and plots the *axial* view of the Rotor and the *axial* and *side* views of the Rotor Bushing. The required input values are under the *Set values* and *Relationship Rules* sub headings.

Listing D.1: Rotor and Rotor Bushing Dimensions.

```
% rotor_and_bushing.m
% Plots Rotor and Rotor Bushing dimensions
% Vlad Kaliyev Jan 15.



---


% Rotor Dimensions


---



clc , clear , close all
% Set values
d_mag=22;           % magnet diameter
h_mag=25.4;        % magnet height
D_r=95;            % rotor diameter
D_shaft=20;        % shaft diameter
D_bush=35;         % bushing diameter
h_collar=10;       % collar length
d_collar=D_shaft+5; % collar diameter
h_protrus=1.5;     % magnet protrusion beyond rotor thickness
r_cut=2;           % radius of cut-outs in the bushing

% Relationship Rules
h_bush=h_mag-2*h_protrus; % bushing height=h_magnet-2*h_protrusion
D_out=D_r-8;           % magnet circle outer diameter
D_in=D_out-2*d_mag;    % magnet circle inner diameter

x=0:pi/100:2*pi;
figure
set(gcf, 'Position', [-136 327 1008 653])

% Plot Rotor
R_out=D_r/2;          % Radius
y=R_out*exp(j*x);
plot(real(y), imag(y), 'Linewidth', 1.5) % rotor
hold on, grid on
axis equal

% Plot shaft
R_shaft=D_shaft/2;    % Radius
y=R_shaft*exp(j*x);
plot(real(y), imag(y), 'c', 'Linewidth', 1.5)
```

```

% Plot bushing collar
R_collar=d_collar/2;      % Radius
y=R_collar*exp(j*x);
plot(real(y),imag(y), 'g', 'Linewidth',1.5)

% Plot bushing
R_bush=D_bush/2;          % Radius
y=R_bush*exp(j*x);
plot(real(y),imag(y), 'm', 'Linewidth',1.5)

% Plot magnet circles inner and outer circles
R_out=D_out/2;           % Radius
R_in=D_in/2;
y=R_out*exp(j*x);
plot(real(y),imag(y), 'k—')
y=R_in*exp(j*x);
plot(real(y),imag(y), 'k-.')

% Plot magnet
r_mag=d_mag/2;
y=r_mag*exp(j*x);
x1=real(y)+R_in+r_mag;   % shift magnet 'x' dimension to the first position
y1=imag(y);
x_center=R_in+r_mag;    % circle's centre 'x'
y_center=0;
plot(x1,y1, 'r—', 'Linewidth',1.5) % first magnet position

plot(x_center,y_center, 'r', 'Marker', 'x', 'Markersize',10,...
      'Linewidth',1.5) % centre of magnet

for n=1:7
    theta=n*pi/4;
    A=[cos(theta) -sin(theta); % transform matrix (rotate angle 'theta')
       sin(theta)  cos(theta)];
    new_magnet=A*[x1;y1];      % new circle
    new_center=A*[x_center;y_center];
    plot(new_magnet(1,:),new_magnet(2,:), 'r—', 'Linewidth',1.5)
    plot(new_center(1,1),new_center(2,1), 'r', 'Marker', 'x', 'Markersize',...
          10, 'Linewidth',1.5) % centre of magnet
end

set(gca,...
     'xlim',[-55 55],...
     'xtick',[-50:10:50],...
     'fontsize',12)
xlabel('X_dimension_(\itmm)', 'fontname','courier_new', 'fontsize',12)

set(gca,...
     'ylim',[-55 55],...
     'ytick',[-50:10:50],...
     'fontsize',12)
ylabel('Y_dimension_(\itmm)', 'fontname','courier_new')

```

```

title({'\bf\fontsize{16}\fontname{courier_new}_Rotor_Dimensions'};...
      ['\fontname{courier_new}\fontsize{12}D_{rotor}=', num2str(D_r, '%2.1f'), ...
       'mm_.....d_{magnet}=', num2str(d_mag, '%2.1f'), 'mm'];...
      ['D_{outer}=', num2str(D_out, '%2.1f'), ...
       'mm_.....D_{inner}=', num2str(D_in, '%2.1f'), 'mm'];...
      ['D_{bushing}=', num2str(D_bush, '%2.1f'), ...
       'mm_.....D_{shaft}=', num2str(D_shaft, '%2.1f'), 'mm']});

legend(' \fontname{times_new_roman}\fontsize{12}Rotor ', ...
       ' \fontname{times_new_roman}\fontsize{12}Shaft ', ...
       ' \fontname{times_new_roman}\fontsize{12}Collar ', ...
       ' \fontname{times_new_roman}\fontsize{12}Bushing ', ...
       ' \fontname{times_new_roman}\fontsize{12}Outer ', ...
       ' \fontname{times_new_roman}\fontsize{12}Inner ', ...
       ' \fontname{times_new_roman}\fontsize{12}Magnets ', ...
       'Location ', 'NorthEastOutside')

%
% Bushing Dimensions
%
figure
set(gcf, 'Position', [14 70 736 600])
set(gca, ...
     'xlim', [-20 70], ...
     'xtick', [-10:10:60], ...
     'xticklabel', {-10 0 10 20 0 10 20 30 }, ...
     'fontsize', 12)

hold on, grid on
axis equal

xlabel('X_dimension_(\itmm)', 'fontname', 'courier_new', 'fontsize', 12)
ylabel('Y_dimension_(\itmm)', 'fontname', 'courier_new', 'fontsize', 12)

% Plot shaft
R_shaft=D_shaft/2;           % Radius
y=R_shaft*exp(j*x);
plot(real(y), imag(y), 'c', 'Linewidth', 1.5)

% Plot bushing collar
R_collar=d_collar/2;       % Radius
y=R_collar*exp(j*x);
plot(real(y), imag(y), 'g', 'Linewidth', 1.5)

% Plot bushing
R_bush=D_bush/2;           % Radius
y=R_bush*exp(j*x);
plot(real(y), imag(y), 'm', 'Linewidth', 1.5)

% Plot Cut-outs in bushing
x=pi/2:pi/100:3*pi/2;      % half circle only from 90 to 270
y=r_cut*exp(j*x);
x1=real(y)+R_bush;         % shift the cut-out 'x' dimension to the first position

```

```

y1=imag(y);
plot(x1,y1,'b—', 'Linewidth',1.5) % first cut-out position
for n=1:7
    theta=n*pi/4;
    A=[cos(theta) -sin(theta); % transformation matrix ( angle 'theta' )
        sin(theta)  cos(theta)];
    new_magnet=A*[x1;y1]; % new circle
    new_center=A*[x_center;y_center];
    plot(new_magnet(1,:),new_magnet(2,:), 'b—', 'Linewidth',1.5)
end

% Side view
datum=30;

rectangle('Position',[datum,-R_bush,h_bush,D_bush],...
          'LineWidth',1.5,'LineStyle','-', 'EdgeColor','m')
rectangle('Position',[datum+h_bush,-R_collar,h_collar,d_collar],...
          'LineWidth',1.5,'LineStyle','-', 'EdgeColor','g')
line([datum, datum+h_bush+h_collar],[R_shaft, R_shaft],...
     'Color','c','LineWidth',1.5,'LineStyle','—')
line([datum, datum+h_bush+h_collar],[-R_shaft, -R_shaft],...
     'Color','c','LineWidth',1.5,'LineStyle','—')
line([datum, datum+h_bush],[R_bush-r_cut, R_bush-r_cut],...
     'Color','b','LineWidth',1.5,'LineStyle','—')
line([datum, datum+h_bush],[-R_bush+r_cut, -R_bush+r_cut],...
     'Color','b','LineWidth',1.5,'LineStyle','—')

text(-10,-R_bush*1.4,...
     '\it \Note: (1) \_cut-outs\_must\_be\_symmetrical\_for\_balance')
text(-10,-R_bush*1.6,...
     ['\it \Note: (2) \_h_{bush}<h_{magnet}\_by\_2*h_{protrus}=2*',...
     num2str(h_protrus, '%2.1f')])

title(...
     {'\bf\ fontsize {16}\ fontname{ courier _new}_Rotor_Bushing_Dimensions'};...
     ['\fontname{ courier _new}\ fontsize {12}D_{bushing}=',...
     num2str(D_bush, '%2.1f'),...
     'mm_{h_{bushing}}=', num2str(h_bush, '%2.1f'), 'mm'];...
     ['d_{collar}=', num2str(d_collar, '%2.1f'),...
     'mm_{h_{collar}}=', num2str(h_collar, '%2.1f'), 'mm'];...
     ['r_{cut-out}=', num2str(r_cut, '%2.1f'), 'mm']});

legend( '\fontname{ times _new _roman}\ fontsize {12}Shaft',...
        '\fontname{ times _new _roman}\ fontsize {12}Collar',...
        '\fontname{ times _new _roman}\ fontsize {12}Bushing',...
        '\fontname{ times _new _roman}\ fontsize {12}Cut-out',...
        'Location', 'NorthEastOutside')

```

D.2 The stator_coils.m MATLAB program

The program `stator_coils.m` plots the limits of the stator coils super positioned onto *axial* view of the Rotor. The required input values are under the *Set values* sub heading. The values under *Set values* and *Relationship Rules* sub headings for the *Rotor Dimension* heading of this program listing must be the same as for `rotor_and_bushing.m` MATLAB listing provided in Appendix D.1.

Listing D.2: Stator Side Coils limits.

```
% stator_coils.m
% -- Plots Stator Coils position and physical limits --
% -- The stator coils super positioned onto Rotor Dimensions set in
% (rotor_and_bushing.m)
% Vlad Kaliyev 18 Mar 15.

% -- All angles are in radians for calculations , and degrees for display
%
%-----
% Nomenclature
% P          - total number of poles
% P_pitch    - pole pitch
% N_s        - number of 'slots' (or coil sides) per stator (symbolic slots
% in case of coreless stator)
% N_c        - number of coils per stator per phase
% N_sc       - number of coils per stator side (N_sc=N_ph*N_c == Q_c)
% N_ph       - number of phases
% k_d        - winding distribution factor (per stator side)
% coil_pitch - displacement angle between coils in a stator side
% P_pitch    - pole pitch

% 1.
% There are 4 cycles in 1 mechanical revolution
% 360M=360E*4=1440E - 1440 Electrical degrees in 360 Mechanical
% Or 360E == 90M
%    120E == 30M

% 2.
% Dual stator - stator on both sides of the rotor.
%
%-----
clc , clear , close all

% Set values
P=8;    % number of poles = number of rotor magnets
N_s=6;  % number of slots (==coil sides) per stator
N_c=2;  % number of coils per phase (per stator side)
N_ph=3;
```



```

coil_clearance=0.5; % clearance between coils in the stator

N_sc=N_c*N_ph; % for double-layer non-overlap N_stator_coils=N_slots
P_pitch=2*pi/P; % pole pitch in radians
coil_pitch=2*pi/N_sc; % coil pitch in radians

%-----
% ROTOR DIMENSIONS
%-----
% plot the rotor first (must be the same as in "rotor_and_bushing.m file")
%-----
% Set values
d_mag=22; % magnet diameter
h_mag=25.4; % magnet height
D_r=95; % rotor diameter
D_shaft=20; % shaft diameter
D_bush=35; % bushing diameter
h_collar=10; % collar length
d_collar=D_shaft+5; % collar diameter

% Relationship Rules
D_out=D_r-8; % magnet circle outer diameter
D_in=D_out-2*d_mag; % magnet circle inner diameter
x=0:pi/100:2*pi;

% Plot Rotor
figure
set(gcf, 'Position', [-136 327 1008 653])

R_out=D_r/2; % Radius
y=R_out*exp(j*x);
plot(real(y), imag(y), 'Linewidth', 1.3) % rotor
hold on, grid on
axis equal

% Plot shaft
R_shaft=D_shaft/2; % Radius
y=R_shaft*exp(j*x);
plot(real(y), imag(y), 'c', 'Linewidth', 1.2)

% Plot bushing collar
R_collar=d_collar/2; % Radius
y=R_collar*exp(j*x);
plot(real(y), imag(y), 'g', 'Linewidth', 1.2)

% Plot bushing
R_bush=D_bush/2; % Radius
y=R_bush*exp(j*x);
plot(real(y), imag(y), 'm', 'Linewidth', 1.2)

% Plot magnet circles inner and outer circles
R_out=D_out/2; % Radius

```

```

R_in=D_in/2;
y=R_out*exp(j*x);
plot(real(y),imag(y),'k—')
y=R_in*exp(j*x);
plot(real(y),imag(y),'k-.')

% Plot magnet
r_mag=d_mag/2;
y=r_mag*exp(j*x);
x1=real(y)+R_in+r_mag; % shift the magnet 'x' dimension to the first pos
y1=imag(y);
magnets=[x1;y1]; % save the first magnet coordinates
magnets(:, :, 1)=magnets;
x_center=R_in+r_mag; % circle's center 'x'
y_center=0;
plot(x1,y1,'b—', 'Linewidth',1.2) % first magnet position
plot(x_center,y_center,'b','Marker','x','Markersize',10,...
     'Linewidth',1.2) % centre of magnet
for n=1:7
    theta=n*pi/4;
    A=[cos(theta) -sin(theta); % transformation matrix
       sin(theta)  cos(theta)];
    new_magnet=A*[x1;y1]; % new circle
    magnets(:, :, n+1)=new_magnet; % add the rest of the magnets
    new_center=A*[x_center;y_center];
    plot(new_magnet(1,:),new_magnet(2,:), 'b—', 'Linewidth',1.2)
    plot(new_center(1,1),new_center(2,1), 'b','Marker','x',...
         'Markersize',10, 'Linewidth',1.2) % center of magnet
end

set(gca,...
     'xlim',[-60 60],...
     'xtick',[-50:10:50],...
     'fontsize',12)
xlabel('X_dimension_(\itmm)', 'fontname','courier_new', 'fontsize',12)
set(gca,...
     'ylim',[-60 60],...
     'ytick',[-50:10:50],...
     'fontsize',12)
ylabel('Y_dimension_(\itmm)', 'fontname','courier_new')

%-----
% STATOR windings
%-----
% bushing collar is physical limiting parameter (can not touch windings)
% N_sc=6; % number of stator winding per side

fprintf('Number_of_stator_coils_(per_side)=%1.0f\n',N_sc)
fprintf(...
     'Coils_span_angle_(phase_''a''_and_''c'')_=%3.2f_degrees_\n',...
     coil_pitch*180/pi)
fprintf('Arc_taken_by_the_winding_=Pole_pitch_=%3.2f_degrees_\n',...

```

```

    P_pitch*180/pi)
fprintf('Arc (gap) between poles = %3.2f degrees\n', ...
    (2*pi-P_pitch*6)*180/pi/6)
gap_pole=(2*pi-P_pitch*6)/6*(R_in+r_mag);
fprintf(...
    'Distance (gap) between poles (center of magnets) = %3.2f mm\n', ...
    gap_pole)
Thick_coil=floor(gap_pole-coil_clearance);
fprintf('Max Coil thickness (gap-clearance) = %3.2f mm\n', Thick_coil)

%extension of active conductors BEYOND magnet's diameter (mm)
w=Thick_coil/2;

%-----
% Phase 'a' single loop coil

% arc taken by a winding = pole pitch

theta_a=-P_pitch; % arc taken by the phase 'a' winding (negative sign is
% for drawing purposes only as first side is taken at 90 degrees and second
% side taken at 'P_pitch' (pole pitch) angle in a clockwise direction)

% first side of phase 'a'
x_a1=zeros(1,100); % 'x' of the first side of phase 'a'
y_a1=linspace(R_in-w, R_out+w,100); % 'y' of the first side of phase 'a'
first_side_a=[x_a1;y_a1]; % first side of phase 'a'
line(x_a1,y_a1,...
    'Color','k','LineWidth',2.5,'LineStyle','—')
A=[cos(theta_a) -sin(theta_a); % transformation matrix
    sin(theta_a) cos(theta_a)];
second_side_a=A*[x_a1;y_a1]; % second side of phase 'a' winding

% second side of phase 'a'
line(second_side_a(1,:),second_side_a(2,:),...
    'Color','k','LineWidth',2.5,'LineStyle','—')

% bottom of phase 'a'
x_bot=pi/2+theta_a:pi/100:pi/2;
bottom_a=(R_in-w)*exp(j*x_bot);
plot(real(bottom_a),imag(bottom_a),'Color','k','LineWidth',2.5,...
    'LineStyle','—')

% top of phase 'a'
x_top=x_bot;
top_a=(R_out+w)*exp(j*x_top);
plot(real(top_a),imag(top_a),'Color','k','LineWidth',2.5,'LineStyle','—')

% plot the rest of windings in a stator side-----
for n=1:N_sc-1
    rotate=n*coil_pitch;
    A=[cos(rotate) -sin(rotate); % transformation matrix
        sin(rotate) cos(rotate)];

```

```

new_first=A*first_side_a;
new_second=A*second_side_a;
new_bot=A*[ real(bottom_a);imag(bottom_a)];
new_top=A*[ real(top_a);imag(top_a)];
plot(new_first(1,:),new_first(2,:), 'k—', 'Linewidth',2.5)
plot(new_second(1,:),new_second(2,:), 'k—', 'Linewidth',2.5)
plot(new_bot(1,:),new_bot(2,:), 'k—', 'Linewidth',2.5)
plot(new_top(1,:),new_top(2,:), 'k—', 'Linewidth',2.5)
end

%-----
% Absolute physical limits for a coil
%-----
theta_lim=(2*pi-P_pitch*6)/6 /2; % half of angular gap between coils' sides
% vertical line
x_lim=zeros(1,100); % 'x' of the vertical line
y_lim=linspace(R_collar, R_out+3*w,100); % 'y' of the vertical line
vertical_limit=[x_lim;y_lim]; % vertical line
%line(x_lim,y_lim,...
% 'Color','r','LineWidth',1.2,'LineStyle','-')
A=[cos(theta_lim) -sin(theta_lim); % transformation matrix
   sin(theta_lim) cos(theta_lim)];
first_side_lim=A*[x_lim;y_lim]; % first side
% first side limit
line(first_side_lim(1,:),first_side_lim(2,:),...
      'Color','r','LineWidth',2,'LineStyle','-')
% the rest of sides of limit
for n=1:N_sc-1
    phi=coil_pitch*n;
    A=[cos(phi) -sin(phi); % transformation matrix
       sin(phi) cos(phi)];
    second_side_lim=A*[first_side_lim(1,:);first_side_lim(2,:)];
% second side limit
line(second_side_lim(1,:),second_side_lim(2,:),...
      'Color','r','LineWidth',2,'LineStyle','-')
end

% bushing collar is physical limiting parameter (can not touch windings)
% Plot collar limit
x=pi/6+theta_lim:pi/100:pi/2+theta_lim; % from 30deg to 90+gap/2
R_collar=d_collar/2; % Radius
y=R_collar*exp(1j*x);
plot(real(y),imag(y), 'r', 'Linewidth',2)

%-----

title(...
    {'\bf\fontsize{16}\fontname{courier_new}Stator_Side_Coils'};...
    ['\fontname{courier_new}\fontsize{12}Number_of_coils_(N_{sc})=',...
    num2str(N_sc, '%2.0f'), '-----Number_of_poles_(P)=', num2str(P, '%2.0f')];...
    ['Coil_Span_Angle_(\theta_{c})_=_',...
    num2str(coil_pitch*180/pi, '%2.2f'), '^{\circ}'];

```

```
[ 'Arc_taken_by_middle_of_coil=Pole_{pitch}=\tau_{p}=\ ', ...  
  num2str(P_pitch*180/pi, '%2.2f'), '^circ' ]});  
legend( '\fontname{times_new_roman}\fontsize{12}Rotor ', ...  
        '\fontname{times_new_roman}\fontsize{12}Shaft ', ...  
        '\fontname{times_new_roman}\fontsize{12}Collar ', ...  
        '\fontname{times_new_roman}\fontsize{12}Bushing ', ...  
        '\fontname{times_new_roman}\fontsize{12}Outer ', ...  
        '\fontname{times_new_roman}\fontsize{12}Inner ', ...  
        '\fontname{times_new_roman}\fontsize{12}Magnets ', ...  
        'Location ', 'NorthEastOutside')
```

Appendix E

Project Timeline

ENG4111/4112 Research Project Timeline 2014-2015

